Doctoral Thesis

Collective Scattering System for high-k turbulence measurement in KSTAR

Dong Jae Lee

Department of Physics

Graduate School of UNIST

2021

Collective Scattering System for high-k turbulence measurement in KSTAR

Dong Jae Lee

Department of Physics

Graduate School of UNIST

Collective Scattering System for high-k turbulence measurement in KSTAR

A thesis/dissertation
submitted to the Graduate School of UNIST
in partial fulfillment of
requirements for the degree of
Doctor of Philosophy

Dong Jae Lee

06. 05. 2020 of submission
Approved by

Advisor
Hyeon Keo Park

Collective Scattering System for high-k turbulence measurement in KSTAR

Dong Jae Lee

This certifies that the thesis/dissertation of Dong Jae Lee is approved

06. 05. 2020 of submission

signature

Advisor: Hyeon Keo Park

signature

Yongkyoon In: Thesis Committee Member #1

signature

Eun Mi Choi: Thesis Committee Member #2

signature

Yong Un Nam: Thesis Committee Member #3

signature

Woochang Lee: Thesis Committee Member #4;

Abstract

Anomalous electron heat transport issue has been a long-standing issue and may be attributed by a small-scale turbulence such as electron temperature gradient (ETG) mode which can induce thermal energy losses even for the regime where the ion-gyroscale turbulence is suppressed in fusion grade plasmas. Magnetohydrodynamic (MHD) instabilities and turbulence of ion-gyroscale are relatively well understood while turbulence of the electron-gyroscale is not well known because of difficulty in the measurement of such small-scale turbulence. Hence, understanding and validation of the electron energy transport arisen from electron-gyroscale turbulence are essential for the magnetic confinement fusion research.

To measure such a small-scale turbulence in KSTAR plasma, a collective scattering system (CSS) has been developed. This diagnostic to simultaneously measures electron density fluctuations at four discrete high poloidal wavenumbers (k_θ) utilizing 300 GHz (λ = 1mm) ordinary (O-mode) probe beam. The range of detectable poloidal wavenumbers is from ~14 to ~26 cm^{-1}, which corresponds to $0.085 \lesssim k_\theta \rho_e \lesssim 0.16$ for 1.8 T KSTAR plasmas with electron temperature (T_e) of 2 keV, where ρ_e is the electron gyroradius. The optical system with remote control capability is able to flexibly change the measurement location from the plasma core (r/a ~ 0.2) to outer edge (r/a ~ 1) on a shot-by-shot basis, where a is the minor radius. To extract phase information as well as the scattered beam power, the CSS employs a quadrature detection system consisting of four-channel detector array and electronics. Inphase and quadrature (IQ) signals from the electronics of 4 MHz bandwidth (determined considering the detectable poloidal wavenumbers and the poloidal rotation speed of KSTAR plasmas) are recorded by a digitizer at a nominal sampling rate 10 MS/s for full discharge pulse length. The spatial resolution is ~6-10 cm in the radial direction and ~1-2 cm in the poloidal direction.

Due to installation of second neutral beam injection (NBI) system, the microwave imaging reflectometer (MIR), developed for ion-gyroscale fluctuation measurement, had been moved to a narrow diagnostic port and shared with the CSS. For sharing a single port, a large-aperture strip-grid beam splitter was developed to effectively separate and combine the 300 GHz O-mode beam for the CSS and 78-96 GHz extraordinary (X-mode) beam for the MIR system mi9nimizing unavoidable power loss by the beam splitter.

The CSS was first installed in the middle of 2018 KSTAR campaign, and successfully commissioned in the 2018 and 2019 KSTAR campaigns. Initial measurement results had been obtained from various plasmas such as ohmic plasmas, low-confinement (L-mode) and high-confinement (H-mode) plasmas.

However, it has to be noted that the CSS can measure large-scale MHD activities since it also works as an interferometer. As the 300 GHz probe beam and four scattered beams pass through the plasma entirely or partially, the measured signals are able to contain information of fluctuations from the large-scale MHD activities. Therefore, one has to consider the interferometric contribution to the CSS data to avoid misinterpretation.

This thesis work describes the theory of scattering, design characteristics of the optical systems, configuration of overall systems, their laboratory test result and initial measurement results. Also, it shows that various physical parameters were calculated and considered to develop CSS suitable for KSTAR plasma research. The initial measurement results show that the turbulence decreases after the L-H transition as well known. In order to measure ETG turbulence in KSTAR plasmas, the experiments were performed to increase the electron temperature gradient. As the temperature increased, an increase in broadband turbulence was measured. In addition, turbulence moving in different poloidal directions, which is estimated as ITG and TEM turbulence in the H-mode plasma pedestal region, was simultaneously measured.

In the future, more intensive analyses of CSS data will be carried out for studies of physics associated with small scale turbulence such as characteristics of ETG or trapped electron mode (TEM) in KSTAR H-mode or hybrid mode edge and their contribution to the plasma performance.

Contents

List of Figures

List of Tables

Abbreviations and Acronyms

D	Deuterium
T	Tritium
He	Helium
T	Tesla
MeV	Mega electron volt
GHz	Gigahertz
mW	Millliwatt
MHz	Megahertz
KeV	Kilo electron volt
Sr	Solid angle
μW	Microwatt
μm	Micrometer
dB	Decibel
dBm	Decibel milliwatte
dBc	Decibel relative to the carrier
μs	Microsecond
Hz	Hertz
Gbps	Gigabits per second
MBytes	Megabytes
FWHM	Full width half maximum
cm	centimeter

Chapter 1

Introduction

1.1 Nuclear fusion energy

Have you ever imagined a world without electrical energy? Since the invention of electricity, civilization has developed rapidly and human life has been enriched. However, the resources to produce electrical energy, such as oil, gas, coal and etc., are not limitless. In addition, they caused various problems such as global warming and environmental pollution. The depletion of these resources will become a huge problem for future generations. For this reason, human beings are steadily working on alternative energy research to solve these energy problems. Among them, nuclear fusion energy, the most efficient and infinite energy in the universe, is considered to be one of the next generation energy sources of mankind and active research is under way.

Tokamak is a toroidal plasma confinement device developed to study nuclear fusion energy. So far, studies have shown that using deuterium-tritium (D-T) reaction which produce an alpha particle and neutron with total energy 17.6 MeV is the most reliable method.

$$ {}^{2}_{1}\mathrm{D} + {}^{3}_{1}\mathrm{T} \rightarrow {}^{4}_{2}\mathrm{He}\ (3.5\ \mathrm{MeV}) + {}^{1}_{0}\mathrm{n}\ (14.1\ \mathrm{MeV}) \qquad (1.1) $$

For the self-sustaining D-T chain reaction in the tokamak, the following relation called Lawson criterion must be satisfied, $nT\tau_E > 3 \times 10^{21}\ \mathrm{m}^{-3}$ keV s where n and T are plasma density and temperature respectively. τ_E is energy confinement time which is defined as $\tau_E = W / (P - dW / dt)$ where W is stored energy of the plasma and P is the total heating power. However, there were reports that there is an upper limit to electron density in toroidal confinement devices. [1, 2] Above all, as the plasma density and temperature increase, it causes a large pressure gradient, resulting in various instabilities and bad plasma confinement. Therefore, it is very important to be able to control MHD instabilities and micro-instabilities at a plasma pressure that can be reached as high

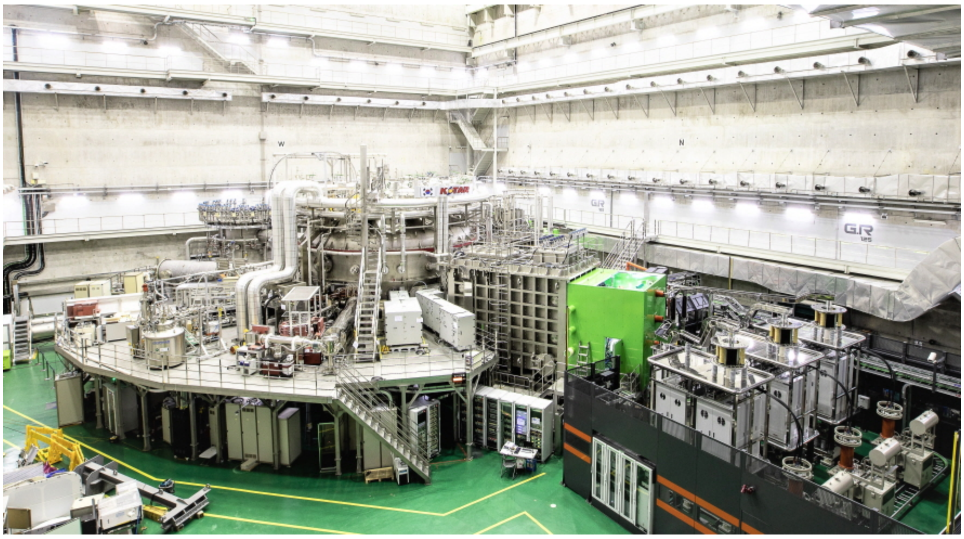

Fig. 1.1 The KSTAR main device with heating and diagnostic systems.

as possible at given magnetic field.

Korea superconducting tokamak advanced research (KSTAR) which is a tokamak developed to study nuclear fusion energy in Korea is one of the first research tokamaks in the world to feature fully superconducting magnets with 16 toroidal field (TF) coils and 7 pairs of poloidal field (PF) coils [3]. A picture of KSTAR and designed plasma parameter is shown in figure **1.1** and table **1.1**. The first plasma of KSTAR was obtained in 2008 and plasma experiments has performed more than 24,000 discharges so far. The KSTAR is actively conducting research with scientists of various nationalities and showing a lot of results, attracting attention from all over the world. Recently, NBI-2 was newly introduced, and it is preparing for an employment of new heating devices such as ECH and plans to replace the inner wall of the Tokamak from carbon to tungsten are in progress. The main goal of KSTAR is to carry out the plasma experiments to control various instabilities, including understanding the physical mechanism, and to perform the experiments to be conducted in ITER in advance. International Thermonuclear Experimental Reactor (ITER) is an experimental device to prove whether the nuclear fusion demonstration reactor is actually possible. ITER is currently being built next to the Cadarache facility in Saint-Paul-les-Durance, in Provence, southern France. Korea, United States, European Union, China, Japan, Russia and India are participating in the ITER project. The construction of ITER is expected to be completed in 2024, D-D and D-T reaction experiment will be started from 2025 and 2035, respectively. The main goal of ITER is to achieve fusion power gain $Q \geq 10$ through D-T reaction with 50 MW external heating for 300 – 500 s which mean fusion power generation is over 500 MW (Q = fusion power / external heating power) [4].

Parameters	KSTAR	ITER
Major radius, R	1.8 m	6.2 m
Minor radius, a	0.5 m	2.0 m
Elongation, κ	2.0	1.7
Triangularity, δ	0.8	0.33
Plasma shape	DN, SN	SN
Auxiliary heating / CD	~ 28 MW	73 (110) MW
Plasma current, I_p	2.0 MA	15 (17) MA
Toroidal field, $B_T(0)$	3.5 T	5.3 T
Pulse length	300 s	400 s
β_n	5.0	1.8 (2.5)

Table 1.1 Compared parameters between KSTAR and ITER.

1.2 Motivation

The most known theory of transport in magnetically confined plasma is the neoclassical transport theory. However, particle and heat transport of tokamak plasmas often exceeds neoclassical expectations by an order of magnitude or more. This experimentally observed strong transport is called anomalous transport. It is known that anomalous transport is caused by several micro-instabilities. The most prominent candidates are ion temperature gradient (ITG) instabilities, trapped electron modes (TEM) and electron temperature gradient (ETG) instabilities. The scales of micro-turbulences and their impact on the transport are schematically shown in figure 1.2. Among them, anomalous electron heat transport issue has been a long-standing issue and may be attributed by a small-scale turbulence such as ETG mode which can induce thermal energy loss even for the regime where the ion-gyroscale turbulence such as ITG and TEM is suppressed in fusion grade plasmas [5]. Magnetohydrodynamic (MHD) instabilities and turbulence of ion-gyroscale are relatively well understood but turbulence of the electron-gyroscale (ETG) is not well known since the spatial scale

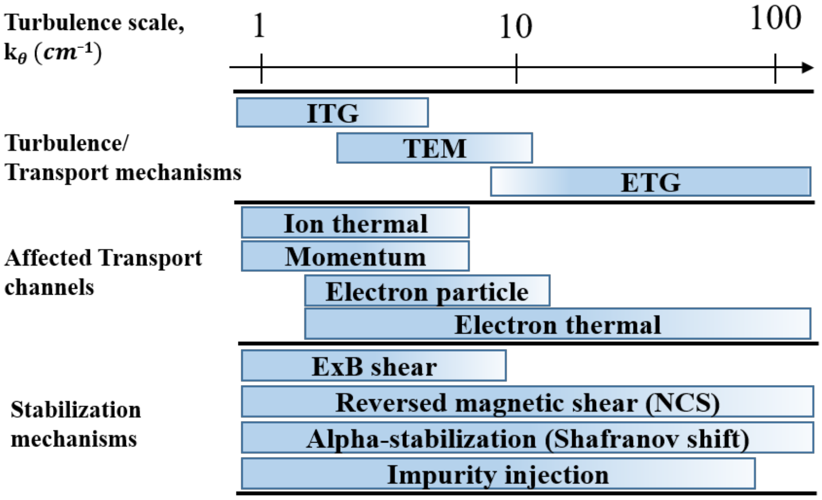

Fig. 1.2 A summary of the scales of three major micro-turbulences with their impact on the transport and typical suppression mechanism.

of ETG mode is very small compared to ITG or MHD instabilities. Therefore, understanding of the electron energy transport arisen from electron-gyroscale turbulence is essential for the magnetic confinement fusion research.

ETG mode instabilities which cause the electron heat transport are characterized by $k_\theta \rho_i \gg 1$ or $k_\theta \rho_e \sim 1$, where ρ_i and is the ion gyroradius. It has been observed that electron heat transport increases dramatically when the electron temperature gradient exceeds a critical electron temperature gradient. Nonlinear gyrokinetic simulations predicted that a significant electron heat transport is observed when ETG is destabilized [5]. Only recently it has reported direct evidence of a small scale turbulence driven by ETG mode through comparison of observed turbulence in National Spherical Torus Experiment (NSTX) and the numerical results from a linear gyrokinetic stability code [7, 8]. As mentioned above, ETG mode instabilities have been observed in several Tokamaks, but the physical mechanism of ETG mode has not been fully clarified. Thus, it is very important to understand exactly how small-scale turbulence plays a role and interacts in the Tokamak plasma. In this process, new physical phenomena can be discovered or clues to problems that have not been solved.

To measure such a small-scale turbulence even in KSTAR plasma, a collective scattering system (CSS) with 300 GHz (1 mm wavelength) has been developed and it is able to simultaneously measure electron density fluctuations at four discrete poloidal wavenumbers in KSTAR [6]. The range of detectable poloidal wavenumbers (k_θ) is from ~14 to ~26 cm^{-1}, which corresponds to the normalized poloidal wavenumbers $0.085 \lesssim k_\theta \rho_e \lesssim 0.16$ for 1.8 T KSTAR plasmas with $T_e \sim 2$

keV, where ρ_e is the electron gyroradius and T_e is the electron temperature. The detectable wavenumbers cover the scales of TEM and ETG mode. The CSS was first installed in middle of 2018, and it successfully commissioned in the 2018 and whole 2019 KSTAR campaigns.

1.3 Thesis organization

This thesis is focused on the development of the collective scattering system and preliminary studies of initial measurements in KSTAR plasmas. Specifically, the thesis is organized as follows. In chapter 2, the theory and basic principle of Thomson scattering are reviewed. In chapter 3, various calculations performed prior to the design of the CSS are presented. These calculations were used to determine the probe beam characteristics of suitable for measuring high-k turbulence in KSTAR plasmas. In addition, ray tracing calculation were performed to check how much the probe beam and scattered beam are refracted in the KSTAR plasma. The chapter 4 covers detail of the collective scattering system design and laboratory test results of the optics and key components of the diagnostic. In chapter 5, I discuss the correlation between electron temperature gradient and small-scale turbulence using the initial data measured by CSS. Also, I interpret interesting observations that turbulences with different wavenumbers move in different poloidal directions in the H-mode pedestal region. In addition, I briefly cover the changes in high-k turbulence through the CSS spectrogram in L-mode, H-mode and observation of Alfven eigenmodes. Finally, the summary, conclusion and future work are briefly presented in chapter 6.

Chapter 2

Theory of Thomson Scattering

2.1 Principle of scattering measurement

First of all, most of the equations in this chapter can be found in references [9, 10, 11]. When electromagnetic waves are incident on the plasma, charged particles move by the interactions with the incident wave and then new electromagnetic waves are generated. In the collision process between photons and electrons, if the photon energy is high enough, then an inelastic collision can occur. This is because the orbits of the colliding electrons change, and the photons lose energy. This kind of scattering is called Compton scattering. On the other hand, if the energy of the photon is low so that the photon has little effect on the electrons, then the energy of the photon is almost maintained. This scattering is called Thomson scattering. In this thesis, we only discuss Thomson scattering.

In the case of Thompson scattering, if the wavelengths of the incident electromagnetic waves are very shorter than the Debye length, the phases of the scattered electromagnetic waves are different from each other (see Fig. 2.1 (b)). It means that the intensity of scattered wave is determined in proportion to the number of particle's causing the scattering. This is called incoherent scattering, and is the principle of the Thomson scattering diagnostics that provides electron temperature and density profiles in fusion plasmas. On the other hand, if the wavelength of the incident wave is much larger than Debye length, the phases of scattered wave are almost the same. It means that when we calculate the intensity of scattered wave, we have to consider the interference effect in scattering volume. This scattering is called coherent scattering or collective scattering, and KSTAR collective scattering system uses this principle to measure small-scale turbulence. We now consider that the scattering process is interaction between the electromagnetic wave and plasma density fluctuation wave. As mentioned above, during the Thomson scattering process, total energy and momentum have to be conserved as

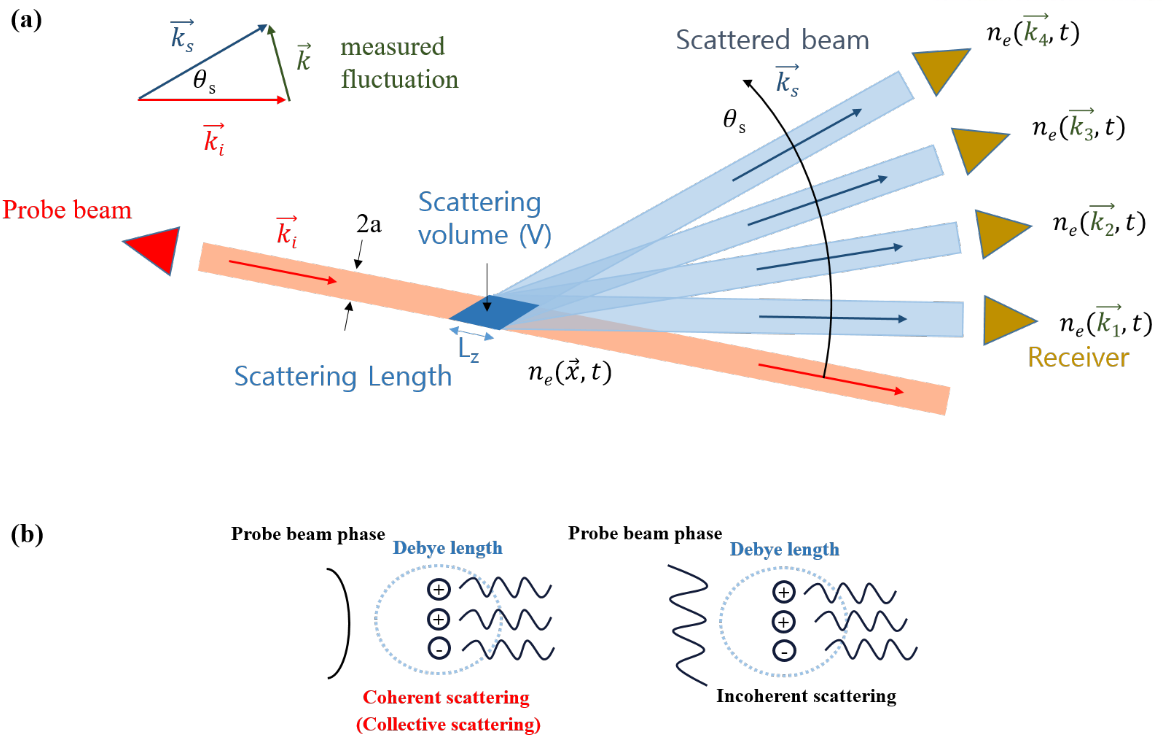

Fig. 2.1 (a) Simple scattering geometry and (b) comparison of the two types of scattering processes.

$$\omega_s = \omega_i + \omega \tag{2.1}$$

$$\vec{k}_s = \vec{k}_i + \vec{k} \tag{2.2}$$

$$\vec{k}_s = \frac{\omega_s}{c} \hat{s}, \tag{2.3}$$

where i and s is incident and scattered wave, respectively and c is the speed of light. We assume that the frequency of a plasma density fluctuation is significantly smaller than the incident wave ($\omega_i \gg \omega \rightarrow k_i \approx k_s$). From the wavenumber matching condition (Eq. (2.2)), we have the following Bragg relationship.

$$k = 2k_i \sin\left(\frac{\theta_s}{2}\right), \tag{2.4}$$

where θ_s is the scattering angle (see Fig. 2.1 (a)). It means that if we measure the scattered wave at a certain angle, the information of the electron density fluctuation can be obtained by Eq. (2.4). The Scattering length (L) shown in Fig 2.1 can be represented as follows.

$$L = \frac{2a}{\sin\theta_s} \tag{2.5}$$

Eq. (2.5) requires careful calculation because the value is incorrect when the scattering angle is sufficiently small. It means that the scattering length (L_z) can be much larger than region of the fluctuations along the probe beam direction.

The mathematical expression for the field profile of a Gaussian beam can be written as

$$E(\vec{r}) \;=\; E_0 e^{-\frac{r_\perp^2}{a^2}}, \tag{2.6}$$

where a is the beam radius at which the field amplitudes fall to 1/e of their axial values. The Fourier transform of the Gaussian beam is

$$\begin{aligned} E(\vec{k}) \;&=\; \int_{\mathrm{V}} d^3r\; E_0 e^{-\frac{r_\perp^2}{a^2}} e^{-i\vec{k}\cdot\vec{r}} \\ &=\; E_0 \int_{-\infty}^{+\infty} dx \int_{-\infty}^{+\infty} dy \int_{-\frac{L_z}{2}}^{+\frac{L_z}{2}} dz\; e^{-\frac{x^2+y^2}{a^2}} e^{-i(k_x x + k_y y + k_z z)} \end{aligned} \tag{2.7}$$

The integral values of each component are (see Appendix A)

$$(x) \;=\; \int_{-\infty}^{+\infty} dx\; e^{-\frac{x^2}{a^2} - ik_x x} \;=\; a\sqrt{\pi} e^{-\frac{a^2}{4}{k_x}^2} \tag{2.8}$$

$$(y) \;=\; \int_{-\infty}^{+\infty} dy\; e^{-\frac{y^2}{a^2} - ik_y y} \;=\; a\sqrt{\pi} e^{-\frac{a^2}{4}{k_y}^2} \tag{2.9}$$

$$(z) \;=\; \int_{-\frac{L_z}{2}}^{+\frac{L_z}{2}} dz\; e^{-ik_z z} \;=\; L_z\; \mathrm{sinc}\left(\frac{k_z L_z}{2}\right) \tag{2.10}$$

Substituting above results into Eq. 2.6, the Fourier transform of the Gaussian beam becomes

$$\begin{aligned} E(\vec{k}) \;&=\; E_0 \pi a^2 L_z e^{-\frac{a^2}{4}({k_x}^2 + {k_y}^2)} \mathrm{sinc}\left(\frac{k_z L_z}{2}\right) \\ &=\; E_0 \mathrm{V} e^{-\frac{a^2}{4}{k_\perp}^2} \mathrm{sinc}\left(\frac{k_z L_z}{2}\right) \\ &=\; E_0 \mathrm{V} e^{-\frac{{k_\perp}^2}{(2/a)^2}} \mathrm{sinc}\left(\frac{k_z}{2/L_z}\right) \end{aligned} \tag{2.11}$$

where $\mathrm{sinc}\left(\frac{k_z}{2/L_z}\right)$ is Sinc function ($\mathrm{sinc}(x) = \frac{\mathrm{sinc}(x)}{x}$) and $\mathrm{V} = \pi a^2 L_z$ is the scattering volume. From Eq. (2.11), we can deduce the k-space resolution.

$$\Delta k_\perp = \frac{2}{a} \qquad (e^{-1} \text{ width}) \tag{2.12}$$

$$\Delta k_z = \frac{2\pi}{L_z} \qquad \text{(0 level width)} \tag{2.13}$$

From the above equation, we can calculate k-space resolution if we know the information of the probe beam and the scattering angle to be measured at the scattering position. Differentiation of Eq. (2.4) gives.

$$k \;=\; k_i \cos\left(\frac{\theta_s}{2}\right)\Delta\theta_s \tag{2.14}$$

Assuming is small enough, we can express it as

$$\Delta k \;=\; k_i \Delta\theta_s \tag{2.15}$$

$$\Delta k_\perp = \frac{2\pi}{\lambda_i}\Delta\theta_s \tag{2.16}$$

In Eq. (2.15), most of the fluctuation components of plasma are $k_\perp$ ($\Delta K \approx \Delta k_\perp$). Substituting Eq. (2.14) into Eq. (2.16), we find that

$$\Delta\theta_s = \frac{\lambda_i}{\pi a} \tag{2.17}$$

Eq. (2.17) means that the scattering has an angular extent related to the probe beam size.

2.2 Scattering radiation

2.2.1 Scattering radiation by a single charge

In order to obtain the electric field due to charged particle accelerating in the field of an external electromagnetic wave, it is necessary to first understand the concept of retarded time (see Fig. 2.2). The radiation $\vec{E}(\vec{r},t)$ of accelerating charged particle is emitted by the motion of a charged particle at an earlier time(retarded time) t' :

$$t' = t - \frac{R}{c} \tag{2.18}$$

where c is speed of light and R is observing position on accelerating charged particle at time t'. Using the above concept, the electric and magnetic fields by accelerating charged particle can be obtained by Lienard-Wiechert formula.

$$V(\vec{r},t) = \frac{1}{4\pi\epsilon_0}\frac{qc}{Rc - \vec{R}\cdot\vec{v}}\,, \qquad \vec{A}(\vec{r},t) = \frac{\vec{v}}{c^2}V(\vec{r},t) \tag{2.19}$$

$$\vec{E} = -\nabla V - \frac{\partial\vec{A}}{\partial t}\,, \qquad \vec{B} = \nabla \times \vec{A}\,, \tag{2.20}$$

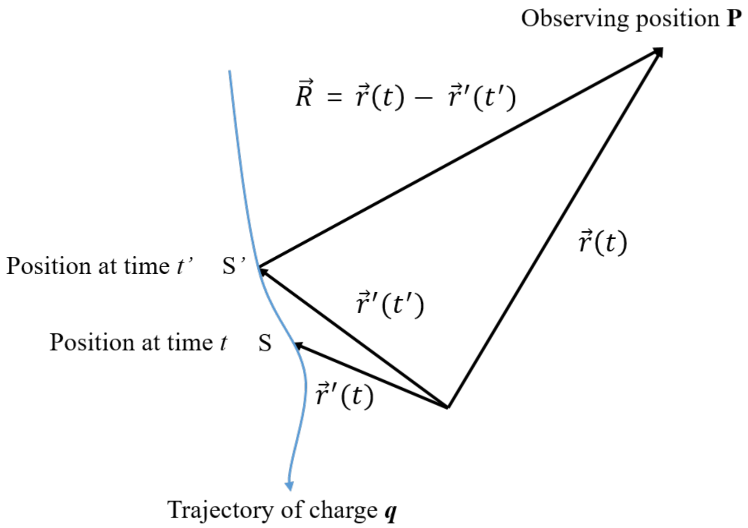

Fig. 2.2 Concept of retarded time and radiation from accelerating charged particle.

where $\vec{v}$ is speed of charged particle at time t'. Since the calculation of Eq. (2.20) is very complex, we first calculate from ∇V.

$$\nabla V = \frac{qc}{4\pi\epsilon_0}\frac{-1}{\left(Rc - \vec{R}\cdot\vec{v}\right)^2}\nabla\left(Rc - \vec{R}\cdot\vec{v}\right) \tag{2.21}$$

By Eq. (2.18), $\nabla(Rc)$ term becomes

$$c\nabla R = -c^2\nabla t' \tag{2.22}$$

$\nabla\left(\vec{R}\cdot\vec{v}\right)$ term also becomes (see Appendix B):

$$\nabla\left(\vec{R}\cdot\vec{v}\right) = \left(\vec{R}\cdot\nabla\right)\vec{v} + (\vec{v}\cdot\nabla)\vec{R} + \vec{R}\times(\nabla\times\vec{v}) + \vec{v}\times\left(\nabla\times\vec{R}\right) \tag{2.23 (a)}$$

$$= \dot{\vec{v}}\left(\vec{R}\cdot\nabla t'\right) + \vec{v} - \vec{v}(\vec{v}\cdot\nabla t') - \vec{R}\times\left(\dot{\vec{v}}\times\nabla t'\right) + \vec{v}\times(\vec{v}\times\nabla t')$$

$$= \vec{v} + \left(\vec{R}\cdot\dot{\vec{v}} - v^2\right)\nabla t' \tag{2.23 (b)}$$

Substituting Eq. (2.22) and (2.23) into Eq. (2.21),

$$\nabla V = \frac{qc}{4\pi\epsilon_0}\frac{-1}{\left(Rc - \vec{R}\cdot\vec{v}\right)^2}\left[\vec{v} + (c^2 + v^2 + \vec{R}\cdot\dot{\vec{v}})\nabla t'\right] \tag{2.24}$$

To finish calculating the Eq. (2.24), we need to calculate the $\nabla t'$. Using Eq. (2.22) (see Appendix B),

$$-c\nabla t' = \nabla R = \nabla\sqrt{\vec{R}\cdot\vec{R}} = \frac{1}{2\sqrt{\vec{R}\cdot\vec{R}}}\nabla(\vec{R}\cdot\vec{R})$$

$$= \frac{1}{R}\left[\left(\vec{R}\cdot\nabla\right)\vec{R} + \vec{R}\times\left(\nabla\times\vec{R}\right)\right] \tag{2.25}$$

In a similar way to Eq. (B.3.2), (B.7):

$$\left(\vec{R}\cdot\nabla\right)\vec{R} = \vec{R} = \vec{v}\left(\vec{R}\cdot\nabla t'\right), \qquad \nabla\times\vec{R} = (\vec{v}\times\nabla t') \tag{2.26}$$

Therefore, we can get the $\nabla t'$.

$$-c\nabla t' = \frac{1}{R}\left[\vec{R} - \vec{v}\left(\vec{R}\cdot\nabla t'\right) + \vec{R}\times(\vec{v}\times\nabla t')\right] = \frac{1}{R}\left[\vec{R} - \left(\vec{R}\cdot\vec{v}\right)\nabla t'\right] \tag{2.27}$$

$$\nabla t' = \frac{-\vec{R}}{Rc - \vec{R}\cdot\vec{v}} \tag{2.28}$$

Substituting Eq. (2.28) into Eq. (2.24),

$$\nabla V = \frac{1}{4\pi\epsilon_0}\frac{qc}{\left(Rc - \vec{R}\cdot\vec{v}\right)^3}\left[\left(Rc - \vec{R}\cdot\vec{v}\right)\vec{v} - \left(c^2 - v^2 + \vec{R}\cdot\dot{\vec{v}}\right)\vec{R}\right] \tag{2.29}$$

Using Eq. (2.19) and Appendix B, $\frac{\partial\vec{A}}{\partial t}$ can be also obtained.

$$\frac{\partial\vec{A}}{\partial t} = \frac{1}{4\pi\epsilon_0}\frac{qc}{\left(Rc - \vec{R}\cdot\vec{v}\right)^3}\left[\left(Rc - \vec{R}\cdot\vec{v}\right)\left(-\vec{v} + \frac{R\cdot\dot{\vec{v}}}{c}\right) + \frac{R}{c}\left(c^2 - v^2 + \vec{R}\cdot\dot{\vec{v}}\right)\vec{v}\right] \tag{2.30}$$

Substituting Eq. (2.29) and (2.30) into Eq. (2.20), finally we can get the electric field due to accelerating charged particle.

$$\vec{E}(\vec{r},t) = -\nabla V - \frac{\partial\vec{A}}{\partial t}$$

$$= \frac{q}{4\pi\epsilon_0}\frac{R}{\left(Rc - \vec{R}\cdot\vec{v}\right)^3}\left[\left(c^2 - v^2\right)\left(c\hat{R} - \vec{v}\right) + \vec{R}\times\left(\left(c\hat{R} - \vec{v}\right)\times\dot{\vec{v}}\right)\right]$$

$$= \frac{1}{4\pi\epsilon_0}\frac{q}{R^2}\left[\frac{(\hat{R} - \vec{\beta})(1 - \beta^2)}{\left(1 - \hat{R}\cdot\vec{\beta}\right)^3}\right] + \frac{1}{4\pi\epsilon_0}\frac{q}{cR}\left[\frac{\hat{R}\times\{(\hat{R} - \vec{\beta})\times\dot{\vec{\beta}}\}}{\left(1 - \hat{R}\cdot\vec{\beta}\right)^3}\right], \tag{2.31}$$

where $\vec{\beta} = \frac{\vec{v}}{c}$. In Eq. (2.31), the first term of the electric field decreases in inverse proportion to the square of the distance to the charged particle. If the particle's velocity and acceleration are zero, this term remains. This is a well-known generalized Coulomb electric field. The second term decreases in inverse proportion to the distance to the charged particle. Therefore, in the long distance (far field), this term become the main electric field and is related to electromagnetic radiation by an accelerating charged particle. Considering a nonrelativistic assumption ($\beta \ll 1$) which is valid for the scattering experiment, the scattered electric field from the charged particle is

$$\vec{E_s}(\vec{r},t) = \frac{1}{4\pi\epsilon_0}\frac{q}{cR}\left[\hat{R}\times\{(\hat{R}-\vec{\beta})\times\dot{\vec{\beta}}\}\right] \tag{2.32}$$

$$\dot{\vec{\beta}} = \frac{\dot{\vec{v}}}{c} = \frac{q\vec{E_\iota}\left(\vec{r'},t'\right)}{mc} \tag{2.33}$$

The movement of ions is relatively slow compared to electrons, so the intensity of radiation by ion is negligible (i.e., q = e). And assuming the far field approximation ($\vec{R} = \vec{r} - \vec{r'} \approx \vec{r}$), the scattered electric field can be written

$$\vec{E_s}(\vec{r},t) = \frac{r_e}{r}\left[\hat{r}\times\{\hat{r}\times\vec{E_\iota}\left(\vec{r'},t'\right)\}\right], \tag{2.34}$$

where $r_e = \frac{e^2}{4\pi\epsilon_0 m_e c^2} \approx 2.82 \times 10^{-15}$ m is the classical radius of electron. Millimeter-wave probe beams used in Tokamak plasma usually use Gaussian beams as follows:

$$\vec{E_\iota}\left(\vec{r'},t'\right) = \vec{E_0}e^{-\frac{{r'_\perp}^2}{w^2(z')}}\ e^{i(k_i z'-\omega_i t')}, \tag{2.35}$$

where $w(z')$ is the beam radius which is the waist size (a) in the entire scattering volume. Inserting above equation into Eq. (2.34), the scattered electric field becomes

$$\vec{E_s}(\vec{r},t) = \frac{E_0 r_e}{r}\left[\hat{r}\times(\hat{r}\times\hat{E_\iota})\right]e^{-\frac{{r'_\perp}^2}{a^2}}\ e^{i(k_i z'-\omega_i t')} \tag{2.36}$$

In this thesis, the electric field $\vec{E_\iota}\left(\vec{r'},t'\right)$ of the probe beam is perpendicular to propagating direction of scattered beam, then $\hat{r}\times\left(\hat{r}\times\hat{E_\iota}\right) = 1$.

$$\vec{E_s}(\vec{r},t) = \frac{E_0 r_e}{r}e^{-\frac{{r'_\perp}^2}{a^2}}\ e^{i(k_i z'-\omega_i t')} \tag{2.37}$$

2.2.2 Scattering radiation by a density fluctuation

The total scattered radiation by the electron density fluctuation ($\tilde{n}_e(\vec{r'},t')$) observed at a time t in the scattering volume (V) is given by

$$\vec{E_s}(\vec{r},t) = \frac{E_0 r_e}{r}\int_V d^3r'\,\tilde{n}_e\left(\vec{r'},t'\right)e^{-\frac{{r'_\perp}^2}{a^2}}\ e^{i\left(k_i z'-\omega_i t'\right)} \tag{2.38}$$

The Fourier transform of electron density fluctuation ($\tilde{n}_e(\overrightarrow{r'},t')$) is expressed in the following form

$$\tilde{n}_e(\overrightarrow{r'},t') = \int_{-\infty}^{+\infty} \frac{d\omega}{2\pi} \int_{-\infty}^{+\infty} \frac{d^3k}{(2\pi)^3} \tilde{n}_e(\vec{k},\omega)\ e^{i(\vec{k}\cdot\overrightarrow{r'}-\omega t')} \tag{2.39}$$

Substituting Eq. (2.39) into Eq. (2.38) gives

$$\overrightarrow{E_s}(\vec{r},t) = \frac{E_0 r_e}{r} \int_V d^3r' \int_{-\infty}^{+\infty} \frac{d\omega}{2\pi} \int_{-\infty}^{+\infty} \frac{d^3k}{(2\pi)^3} \tilde{n}_e(\vec{k},\omega) e^{-\frac{{r'_\perp}^2}{a^2}}\ e^{i(\vec{k}\cdot\overrightarrow{r'}+k_i z'-(\omega_i+\omega)t')} \tag{2.40}$$

Assuming the far field from above, Eq. (2.18) becomes

$$t' = t - \frac{\left|\vec{r}(t) - \overrightarrow{r'}(t')\right|}{c} = t - \frac{\sqrt{r^2 + {r'}^2 - 2\vec{r}\cdot\overrightarrow{r'}}}{c}$$

$$= t - \frac{r}{c}\sqrt{1 + \frac{{r'}^2}{r^2} - 2\frac{\hat{r}\cdot\overrightarrow{r'}}{r}}\ \approx t - \frac{r}{c} + \frac{\hat{r}\cdot\overrightarrow{r'}}{c} \tag{2.41}$$

Using Eq. (2.1), (2.41) and the scattered wavenumber vector ($\overrightarrow{k_s} \approx \frac{\omega_s}{c}\hat{r}$), rearrange the exponential term of Eq. (2.40), then we can get following equation as

$$\overrightarrow{E_s}(\vec{r},t) = \frac{E_0 r_e}{r} \int_V d^3r' \int_{-\infty}^{+\infty} \frac{d\omega}{2\pi} \int_{-\infty}^{+\infty} \frac{d^3k}{(2\pi)^3} \tilde{n}_e(\vec{k},\omega) e^{-\frac{{r'_\perp}^2}{a^2}+i(\vec{k}-\vec{k}_m)\cdot\overrightarrow{r'}+i(\vec{k}_s\cdot\vec{r}-\omega_s t)} \tag{2.42}$$

where we defined $\vec{k}_m = \vec{k}_s - \vec{k}_i$. And the volume integral of Eq. (2.42) becomes (see Appendix A)

$$\int_V d^3r'\, e^{-\frac{{r'_\perp}^2}{a^2}+i(\vec{k}-\vec{k}_m)\cdot\overrightarrow{r'}} = \mathrm{V}e^{-\frac{(\vec{k}-\vec{k}_m)_\perp^2}{(2/a)^2}} \operatorname{sinc}\left[\frac{(\vec{k}-\vec{k}_m)_z}{2/L_z}\right] \tag{2.43}$$

Substituting Eq. (2.43) into Eq. (2.42),

$$\overrightarrow{E_s}(\vec{r},t) = \frac{E_0 r_e \mathrm{V}}{r} \int_{-\infty}^{+\infty} \frac{d\omega}{2\pi} \int_{-\infty}^{+\infty} \frac{d^3k}{(2\pi)^3} \tilde{n}_e(\vec{k},\omega) f(\vec{k},\vec{k}_m) e^{i(\vec{k}_s\cdot\vec{r}-\omega_s t)} \tag{2.44}$$

Where $f(\vec{k},\vec{k}_m)$ is defined as

$$f(\vec{k},\vec{k}_m) = e^{-\frac{(\vec{k}-\vec{k}_m)_\perp^2}{(2/a)^2}} \operatorname{sinc}\left[\frac{(\vec{k}-\vec{k}_m)_z}{2/L_z}\right] \tag{2.45}$$

If $\vec{k} = \vec{k}_m,\ f(\vec{k},\vec{k}_m) = 1$

Considering electron density fluctuation ($\tilde{n}_e(\overrightarrow{r'},t')$) which has a constant wave vector ($\vec{k}_\omega$) and a single frequency (ω_ω),

$$\tilde{n}_e\left(\vec{r'}, t'\right) = \frac{\tilde{n}_e}{2} e^{i\left(\vec{k}_\omega \cdot \vec{r'} - \omega_\omega t'\right)}, \tag{2.46}$$

where $\tilde{n}_e$ is the peak amplitude at the center of scattering volume. The Fourier transformed electron density fluctuation is

$$\tilde{n}_e\left(\vec{k}, \omega\right) = \frac{\tilde{n}_e}{2} (2\pi)^4 \delta(\omega - \omega_\omega) \delta\left(\vec{k} - \vec{k}_\omega\right) \tag{2.47}$$

Substituting Eq. (2.47) into Eq. (2.44), and then perform the integrals

$$\overrightarrow{E_s}(\vec{r}, t) = \frac{E_0 r_e \tilde{n}_e \mathrm{V}}{2r} f\left(\vec{k}_\omega, \vec{k}_m\right) e^{i\left(\vec{k}_s \cdot \vec{r} - \omega_s t'\right)} \tag{2.48}$$

2.2.2 Scattering radiation power

The scattered average power per unit area is defined as

$$I = \frac{P}{A} = \langle |\vec{S}| \rangle_{time} = \frac{1}{2} c \epsilon_0 \, \langle |\vec{E}|^2 \rangle_{time} \tag{2.49}$$

where $\vec{S}$ is Poynting vector and < > is an time average over a $time$. The scattered power per unit solid angle is

$$\frac{dP_s(\vec{r})}{d\Omega} = \frac{1}{2} c \epsilon_0 r^2 \, \langle |\vec{E}_s(\vec{r}, t)|^2 \rangle_{time} \tag{2.50}$$

Assuming r >> a, the beam radius of the scattered beam which is Gaussian beam at a distance r can be derived as

$$w_s{}^2(\vec{r}) = a^2 \left[1 + \left(\frac{\lambda_s r}{\pi a^2}\right)^2\right] \approx \left(\frac{\lambda_s r}{\pi a}\right)^2 \tag{2.51}$$

Using $\lambda_s \approx \lambda_i$, the solid angle at a position $(\vec{r})$ becomes

$$d\Omega = \frac{\pi w_s{}^2(\vec{r})}{r^2} = \frac{\lambda_i{}^2}{\pi a^2} = \frac{\lambda_i{}^2 L_z}{\mathrm{V}} \tag{2.52}$$

Inserting Eq. (2.52) into Eq. (2.50), the total scattered power is

$$P_s(\vec{r}) = \frac{c \epsilon_0 r^2 \lambda_i{}^2 L_z}{2\mathrm{V}} \langle |\vec{E}_s(\vec{r}, t)|^2 \rangle_{time} \tag{2.53}$$

< **Coherent density fluctuation case** >

Substituting Eq. (2.48) into Eq. (2.53), the total power of scattering radiation is

$$P_s(\vec{r}) = \frac{1}{4} P_0 \tilde{n}_e{}^2 r_e{}^2 L_z{}^2 \lambda_i{}^2 f^2(\vec{k}_\omega, \vec{k}_m), \tag{2.54}$$

where P_0 is power of probe beam [mW] and $\frac{P_0}{\mathrm{A}} = \frac{1}{2} c\epsilon_0 E_o{}^2$. For example, using actual parameter from the KSTAR collective scattering system, $P_0 = 50$ mW and λ_i = 0.1 cm, then the power of scattering radiation is

$$P_s[\mathrm{mW}] = 1 \times 10^{-26} \times \tilde{n}_e{}^2[\mathrm{cm}] L_z{}^2[\mathrm{cm}] \tag{2.55}$$

< **Incoherent density fluctuation case** >

The incoherent density fluctuation case is out of our interest, so the detailed process is omitted. For details, please refer to the following reference [9,10,11]. The total power of scattering radiation by incoherent density fluctuation can be obtain by

$$P_s(\vec{r}) = P_0 r_e{}^2 L_z{}^2 \lambda_i{}^2 f^2(\vec{k}_\omega, \vec{k}_m) \int_{-\infty}^{+\infty} \frac{d\omega}{2\pi} \frac{1}{T} \left|\tilde{n}_e(\vec{k}_\omega, \omega)\right|^2 \tag{2.56}$$

Chapter 3

Preparation for design of diagnostics

3.1 Probe beam frequency and polarization

In order to measure high-k turbulence using the coherent scattering principle in the Tokamak plasma, it is necessary to determine characteristics of the probe beam such as the frequency and polarization. The wavenumber of measured electron density fluctuation is determined by the wavenumber of the probe beam and scattering angle represented by Eq. (2.14). As the frequency of the probe beam increases, the wavenumber of the turbulence measured in the plasma increases. However, when it is higher than a certain level, the wavelength of the probe beam becomes smaller than the Debye length of the plasma (~10^{-5}), and the coherent scattering does not occur. Therefore, it is necessary to select the proper frequency and polarization of the probe beam considering various factors according to the characteristics of the turbulence to be measured. Since microwave imaging reflectometry (MIR) system [12, 13] and beam emission spectroscopy (BES) [14] had been already installed for ion-scale turbulence ($k < 5\ \mathrm{cm}^{-1}$) in KSTAR, it was decided that the collective scattering system measures smaller scale turbulence ($k > 10\ \mathrm{cm}^{-1}$). Considering the space of the available diagnostic port in KSTAR and the realistic design of the optical system, the maximum scattering angle is ~ 20 degrees. When using a probe beam of about 300 GHz at this angle, it is possible to measure the wavenumber of turbulence over 20 cm^{-1}.

3.1.1 ECR frequency and absorption coefficient.

In the conceptual design of the CSS, the probe beam is transmitted through the plasma and reflected from the inner wall of KSTAR, and then makes a focus on the outboard region. However, there is an electron cyclotron resonant (ECR) layer for a given frequency in the plasma that can absorb some power of the electromagnetic wave. Absorption coefficient (relative absorption ratio) is dependent on the harmonic number and polarization

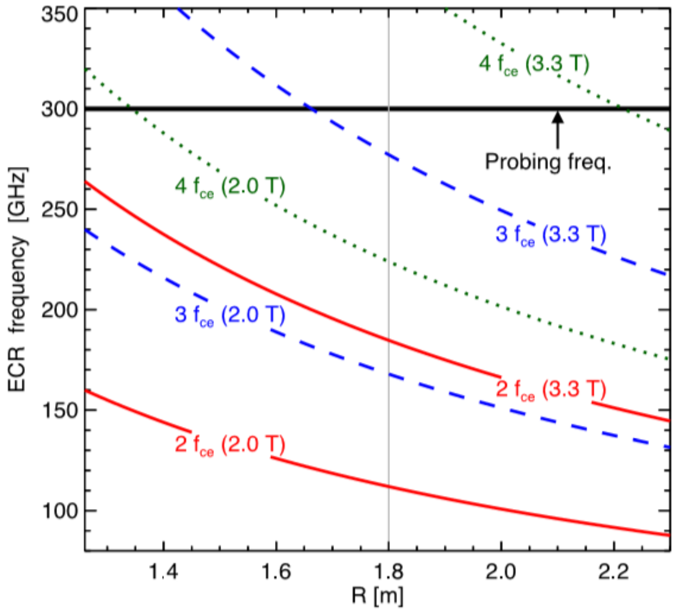

Fig. 3.1 The electron cyclotron resonance (ECR) frequencies of the second, third, and fourth harmonics for KSTAR plasmas at nominal operation fields from 2.0 T to 3.3 T. [5]

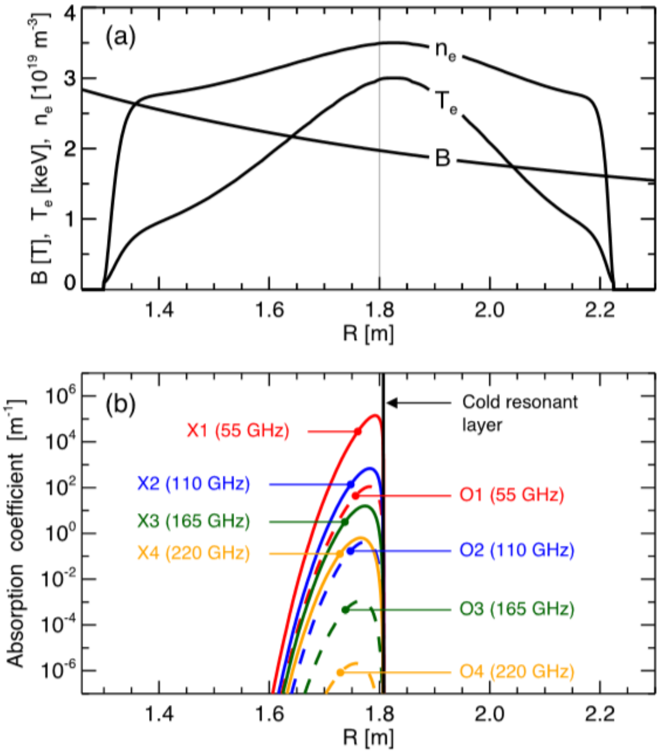

Fig. 3.2 (a) Profiles of an H-mode plasma ($B_{t0} = 2.0\ \mathrm{T}, T_{e0} = 3.0\ \mathrm{KeV}, \mathrm{and}\ n_{e0} = 3.5 \times 10^{19}\ \mathrm{m}^{-3}$) and (b) absorption coefficients of several lower ECE harmonics where O1 and X1 is fundamental ordinary mode, fundamental extraordinary mode respectively, O2 is 2nd harmonic ordinary mode, and so on. [5]

of the ECR layer. Typically, the absorption coefficient is higher at lower harmonic number and X-mode polarization. So it is necessary to choose an appropriate frequency and polarization for the probe beam to minimize the absorption at the resonant layer within the plasma. Figure 3.1 shows the ECR frequencies of the second, third and fourth harmonics for KSTAR plasmas at two magnetic fields 2.0 T and 3.3 T, which are nominal lower and upper limit of the magnetic field. To avoid the second harmonic layer (from 87 to 265 GHz), which is widely used for ECR heating due to its strong absorption, the probe beam frequency has to be higher than 265 GHz and thus 300 GHz was chosen. As can be seen from Fig. 3.2, the absorption coefficient of ordinary mode (O-mode) is lower by two orders of magnitude than that of extraordinary (X-mode), so it is an appropriate choice to use the O-mode probe beam.

3.1.2 ECE emissivity and system noise

The 300 GHz probe beam passes the fourth and fifth ECR layers for 2 T plasmas and this implies that 300 GHz electron cyclotron emission (ECE) from the layers are emitted. If the ECE power is large enough to be compared with scattered radiation power, it acts as noise and then we cannot properly obtain information of small scale electron density fluctuations. Figure 3.3 shows the calculation results of the 300 GHz O-mode fourth and fifth harmonic emissivity. The total integral of the O5-mode emissivity is 4.7×10^{-9} μWm^{-2}Sr^{-1}MHz^{-1}. When the bandwidth of the detection system and solid angle are considered, the detected ECE power is much reduced. An expected scattered radiation power using Eq. (2.55) is $P_s = 4.0$ μW (assuming $P_i = 20$ mW, $\lambda_i = 1$ mm, $L_z = 10$ cm and $\delta n_e = 1 \times 10^{17}$ m^{-3}). Note that the actual output power of the probe beam source is 45 mW and various losses such as absorption of the vacuum window were considered. In conclusion, the O5-mode emissivity is negligible since the ECE power is significantly smaller (by nine orders of magnitude) than the expected scattered power.

The system noise power is defined by

$$P_n = k_B T_n B_n \tag{3.1}$$

where $k_B = 1.38 \times 10^{-23}$ J/K is the Boltzmann constant, T_n and B_n are the noise temperature and bandwidth of the detection system respectively. The bandwidth of detection system is 20 MHz, and assuming the noise temperature of 5000 K, the system noise power is 1.38×10^{-6} μW. The minimum detectable electron density fluctuation ($\frac{\delta n_e}{n_e} \approx 8 \times 10^{-6}$) is sufficiently small.

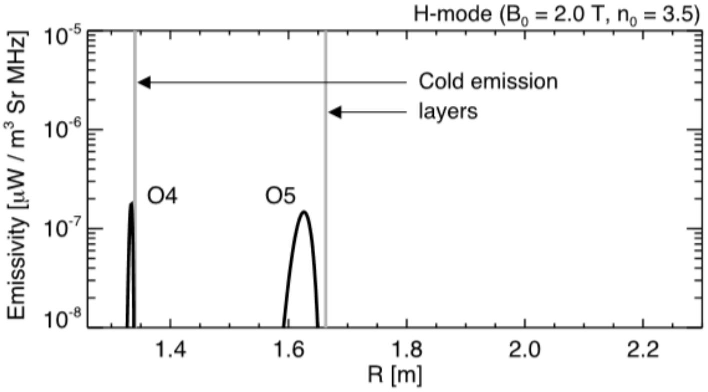

Fig. 3.3 Emissivity of 300 GHz O-mode fourth and fifth harmonic electron cyclotron emission for 2 T plasma.

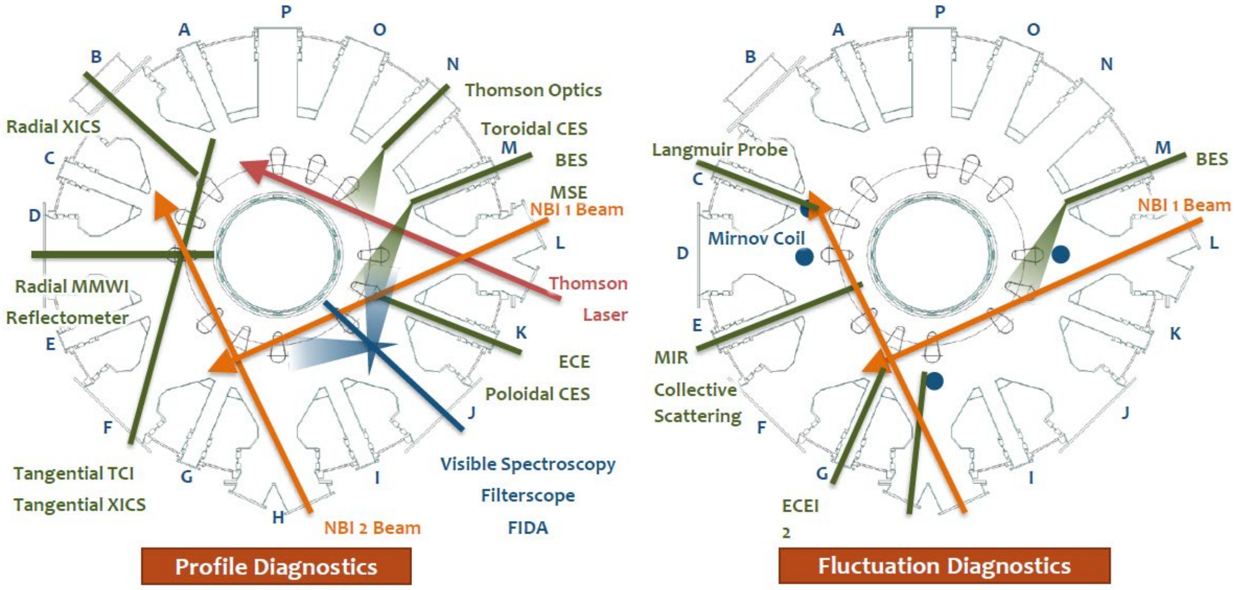

Fig. 3.4 Top view diagram of KSTAR diagnostics in 2019. The CSS is installed on the E-port together with the MIR system.

3.2 The CSS and MIR diagnostics.

The KSTAR is equipped with various diagnostics and heating devices for various research purposes as shown in Fig 3.4. During the development of the CSS, the microwave imaging reflectometry (MIR) system was planned to move from the G-port to the E-port and share the port with the CSS due to the introduction of new neutral beam injection (NBI-2) system [15]. Prior to the 2019 KSTAR campaign, the MIR system had shared the G-port with the electron cyclotron emission imaging (ECEI) system [16, 17]. A glass beam splitter made of 1.1 mm thick Borofloat 33 was used to split and combine the optical paths of the two diagnostics. Also a glass beam splitter of the same glass was used to combine and split the optical path of the probing optics and the receiving optics of the MIR system. In the frequency range 78-100 GHz and X-mode polarization used by both the MIR system and ECEI system, the glass beam splitter has roughly 50:50 transmittance (power transmission ratio) and reflectance (power reflection ratio), respectively. In fact, the 50:50 transmittance and reflectance imply that each beam loses its power when it passes the beam splitter. However, since the CSS and MIR system use entirely different frequency ranges and polarizations using the glass beam splitter is not efficient. Moreover, as shown in Fig 3.5, it has a very low reflectance of less than 20 % and a high absorptance (power loss at the glass) of over 30% for 300 GHz O-mode beam. The dashed curves are the calculated results using the loss tangent (4.6) and dielectric constant (3.7 x 10^{-3}) reported at 1 MHz, but they are significantly different from the measured results. The solid cures are the calculated results using different loss tangent (4.35) and dielectric constant (2.7 x 10^{-3}), which were chosen for matching with the measured results.

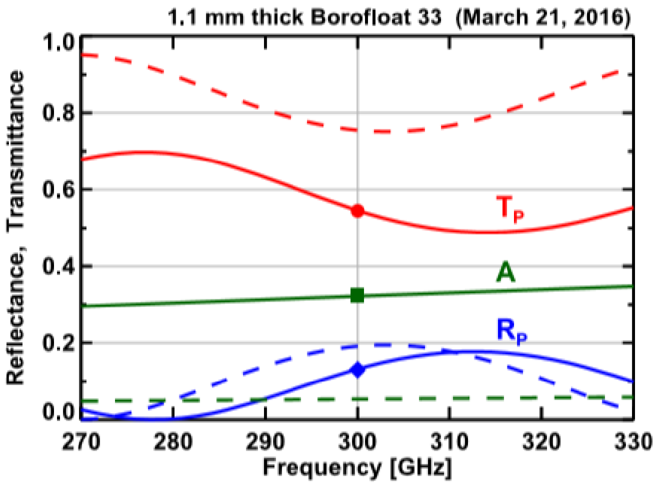

Fig 3.5 Reflectance, transmittance, and absorptance of the glass beam splitter of the P-polarization beam (O-mode): measured at 300 GHz (symbols) and calculated in 270-330 GHz (curve). The solid curve and the dashed curves were obtained with the dielectric constant 4.35 and 4.6, loss tangent 2.7 $\times 10^{-2}$ and 3.7 $\times 10^{-3}$, respectively [18].

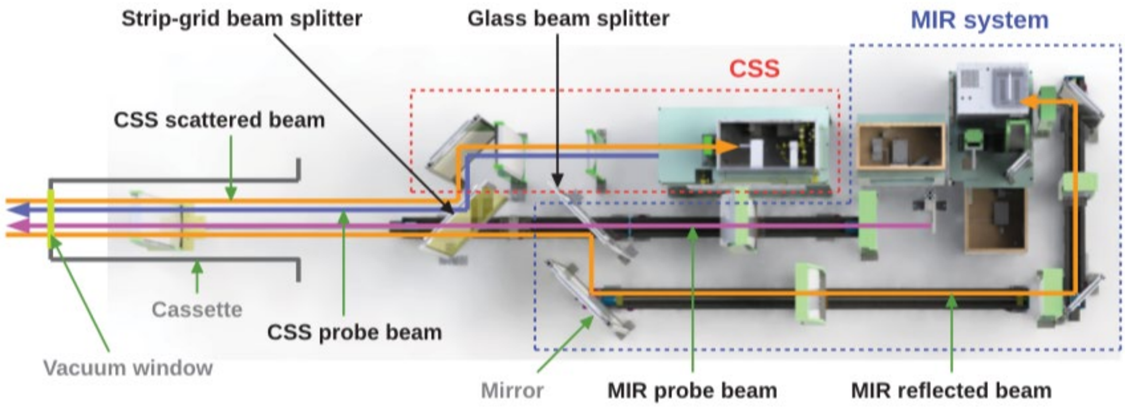

Fig. 3.6 a 3D design of MIR system and CSS in KSTAR E-port (top view) [18].

3.2.1 Strip-grid beamsplitter

As mentioned above, since the frequencies range and polarizations of two diagnostics are different, it is necessary to employ a new type of beam splitter to effectively separate and combine the two optical systems. Consider the case of an incident beam passing through the wire-grids with uniform spacing (g) as shown in Fig 3.7. With $g \ll \frac{\lambda}{2}$ and $2a < g$, for an electric field of incident beam polarized perpendicular to the wire direction, the impedance of the grid is much higher than that of free space, so the grid has almost no effect and is mostly transmitted. This impedance is a characteristic of a medium and indicates the degree to which it interferes with the flow (Imagine a circuit connected in parallel, one with resistance and the other with no resistance). However, for an electric field of incident beam polarized parallel to the wire direction, the impedance of the grid is much lower than the characteristic impedance of the transmission line representing free space, so the transmittance and reflectance of a specific frequency can be controlled by the grid width ($2a$) and grid spacing (g). In the long-wavelength limit ($g \ll \lambda$), the impedance of the wire-grid with a $2a$ is given as [19]

$$\frac{Z_g}{Z_{fs}} = j\left(\frac{g}{\lambda}\right)\ln\left(\frac{g}{2\pi a}\right), \tag{3.2}$$

and the impedance of the strip-grid with a width $2a$ is given

$$\frac{Z_g}{Z_{fs}} = j\left(\frac{g}{\lambda}\right)\ln\csc\left(\frac{\pi a}{g}\right), \tag{3.3}$$

where Z_{fs} is the characteristic transmission line impedance, Z_g is the total grid impedance, g is grid spacing, and λ is the wavelength of the incident beam. The Eq. (3.2) and (3.3) are purely imaginary impedance

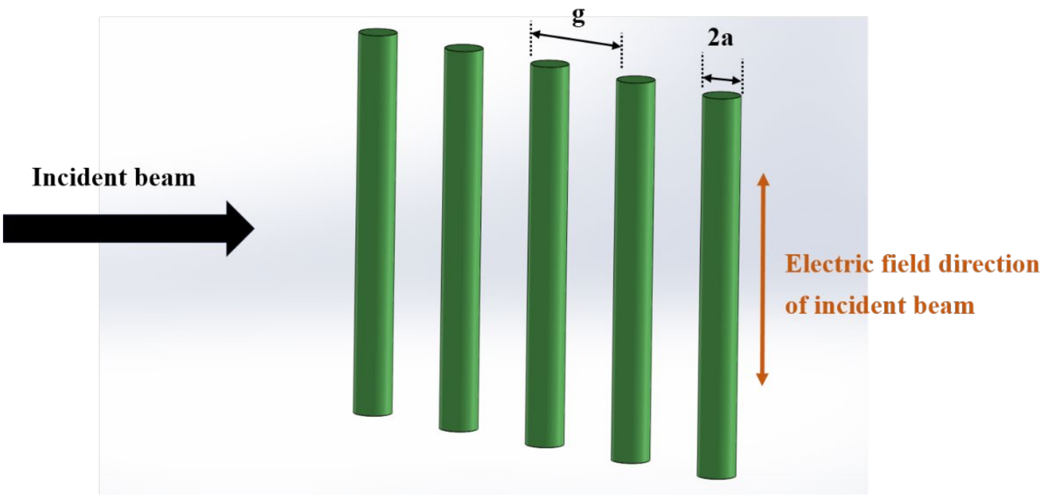

Fig 3.7 Schematic drawing of one dimensional wire-grids and incident beam with the electric field direction parallel to the wire-grids, where g is the grid spacing and $2a$ is grid diameter.

increasing in proportion to the frequency and valid only in the limit λ considerably greater than the grid dimension. The electric field reflection and the transmission coefficient are

$$r_{\parallel} = \frac{\mathrm{E_{ref}}}{\mathrm{E_{inc}}} = \frac{\frac{-Z_{fs}{}^{2}}{Z_s}}{2Z_{fs} + \frac{Z_{fs}{}^{2}}{Z_s}} = \frac{-1}{1 + \frac{2Z_s}{Z_{fs}}} \tag{3.4}$$

$$t_{\parallel} = \frac{\mathrm{E_{tra}}}{\mathrm{E_{inc}}} = \frac{1}{1 + \frac{Z_{fs}}{2Z_s}} \tag{3.5}$$

where $\mathrm{E_{inc}}$ is the electric field of the incident beam, $\mathrm{E_{ref}}$ and $\mathrm{E_{tra}}$ are the electric field of the reflected and transmitted beams, respectively. The fractional power of reflection and transmission are the squared magnitude of the expressions given in Eq. (3.4) and (3.5). The reflectance and transmittance as a function of $\frac{g}{\lambda}$ with $2a$ = 0.15 mm and g = 0.3 mm are shown in Fig 3.8. The expected reflectance is 96 % for the 300 GHz O-mode incident beam. Since reflectance increases in inverse proportion to g, it is better to reduce g as much as possible. Of course, if g decreases, a should be reduced appropriately to fit it. However, due to technical difficulty and cost, a strip-grid with g = 0.3 mm was fabricated using an etching technique on a dielectric substrate sheet which is RO4003C with 0.84 mm thickness. The thickness of the copper strips on the RO4003C substrate is 17 μm. Figure 3.9 shows the laboratory test results of the strip-grid beamsplitter for the 300 GHz O-mode beam together with the schematic test setups. The total beam power was calculated by integrating the beam intensity on the 2D plane by measuring the 2D profile at a fixed distance z = 500 mm for the three cases.

The reflectance is ~ 98.3 % and the transmittance is 2.5 %. There is ~2% difference between the measured value and the calculated value. This might be caused by the power variation of the source beam and the manufacturing tolerance of the strip-grid beam splitter.

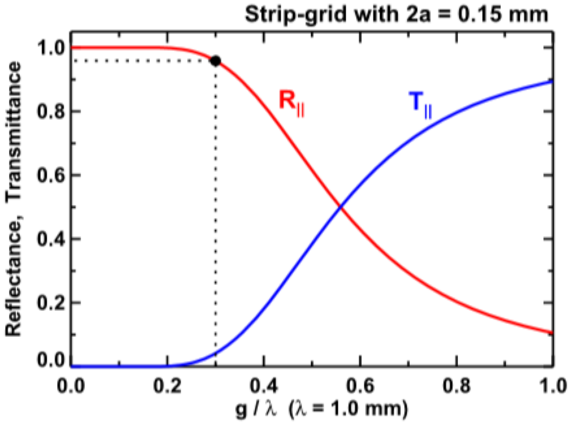

Fig. 3.8 The reflectance and transmittance of strip-grid beam splitter calculated theoretically as a function of $\frac{g}{\lambda}$ with the strip width 2a = 0.15 mm for the 300 GHz incident beam with the electric field parallel to the direction of the strips. [18]

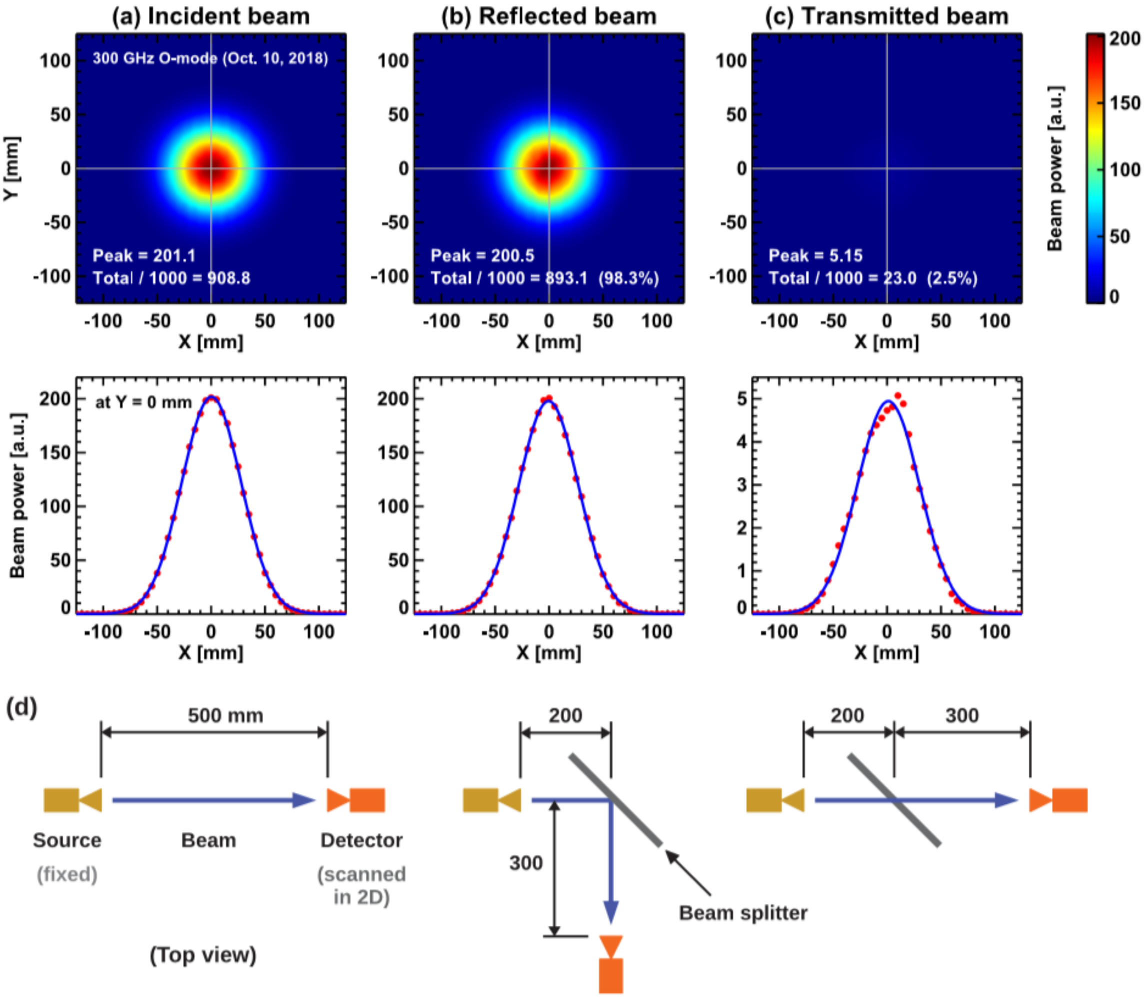

Fig. 3.9 The measured 2D and 1D (horizontal at Y = 0) intensity profiles for 300 GHz O-mode beams: (a) the incident beam without the strip-grid beam splitter, (b) the reflected beam from strip-grid beam splitter, and (c) the transmitted beam through the strip-grid beam splitter. [18]

3.2.1 Transmittance of the dielectric substrate

With $g \ll \frac{\lambda}{2}$, if the grid beam splitter is manufactured using only a wire-grid or strip-grid without a dielectric substrate, almost all X-mode beams in which the electric field direction is perpendicular to the wire direction are transmitted. However, since it is difficult to manufacture in this way, a dielectric substrate is used. In addition, since the beam splitter is positioned at a 45 degrees angle in the horizontal direction with respect to the beam propagation direction, the reflectance and transmittance vary depending on the frequency. The reflectance of incident beam penetrating dielectric material is given as [20]

$$\mathrm{R} = \frac{{r_{12}}^2 + {r_{23}}^2 + 2r_{12}r_{23}\cos(2k_0 N_r t\cos\theta_2)}{1 + {r_{12}}^2{r_{23}}^2 + 2r_{12}r_{23}\cos(2k_0 N_r t\cos\theta_2)}, \tag{3.6}$$

where k_0 is the wavenumber of the incident beam, N_r is the real part of complex refractive index $(N_r - jN_i)$ of the dielectric material which is related to the dielectric constant (ϵ_r) as $N_r = \sqrt{\epsilon_r}$, and t is the thickness of dielectric material. r_{12} is the reflection coefficient of the beam field at surface 1 given as

$$r_{12} = -\frac{\sin(\theta_1 - \theta_2)}{\sin(\theta_1 + \theta_2)} \quad (\mathrm{S-polarization}),$$

$$r_{12} = -\frac{\tan(\theta_1 - \theta_2)}{\tan(\theta_1 + \theta_2)} \quad (\mathrm{P-polarization}) \tag{3.7}$$

. r_{23} is the reflection coefficient of the beam field at surface 2 given as

$$r_{23} = -\frac{\sin(\theta_2 - \theta_3)}{\sin(\theta_2 + \theta_3)} \quad (\mathrm{S-polarization}),$$

$$r_{23} = -\frac{\tan(\theta_2 - \theta_3)}{\tan(\theta_2 + \theta_3)} \quad (\mathrm{P-polarization}) \tag{3.8}$$

where θ_1 is the incident angle to the surface 1 of the dielectric material, θ_2 is the refracted angle from the surface 1, and θ_3 is the refracted angle from the surface 2 shown in Fig 3.10. The two orthogonal linear polarization states S-polarization and P-polarization are important parts for reflection and transmission. For the S-polarized beam, the electric field is perpendicular to the plane of incidence, while that of the P-polarized beam is parallel to this plane. The dielectric loss of the beam power in dielectric material as absorptance is given by

$$\mathrm{A} = 1 - e^{-\delta k_0 N_r t} \tag{3.9}$$

where $\delta \approx \tan\delta = \frac{\epsilon_i}{\epsilon_r}$ is the loss tangent which is the ratio of the imaginary to real dielectric constant, and ϵ_i is imaginary value of the complex dielectric constant. Then, the transmittance is as follows.

$$\mathrm{T} = 1 - \mathrm{R} - \mathrm{A} \tag{3.10}$$

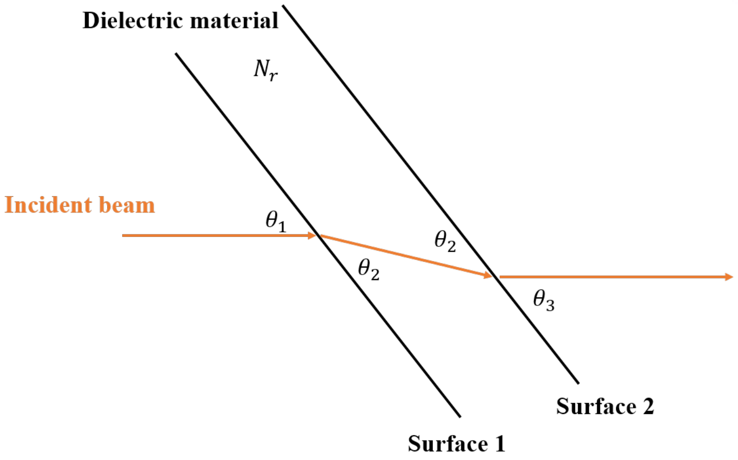

Fig. 3.10 Schematic drawing of the passage of an incident beam through dielectric material.

The known dielectric constant and loss tangent of RO4003C are 3.38 $\pm$ 0.05 and 2.7 $\times 10^{-3}$ at 10 GHz, respectively. Since no measured results have been reported yet, the transmittance were calculated using these values in the frequency range from 75 to 110 GHz for the thickness from 0.2 to 0.8 mm as shown in Fig 3.11. Note that the MIR system employs the heterodyne detection system which down-converts the measured reflected beam to the four IF frequencies, and these IF frequencies are transmitted to the electronics through 20 m long broad-band cable. Here, since the broad-band cable loss is higher at higher frequency, the thickness of the dielectric material sheet is determined so that the transmittance increases as the frequency increases. Fig. 3.12 shows calculated and measured transmittance, reflectance, and absorptance as a function of frequency from 75 to 110 GHz for the strip-grid beam splitter which has 0.84 mm thickness of the dielectric material sheet RO4003C. As shown in Fig 3.12, the transmittance of grid-strip beam splitter is 65% - 92 % for the X-mode probe beams in 78-96 GHz being used for the MIR system and the calculated value and the measured value agree well. In conclusion, the grid-strip beam splitter makes it possible to effectively separate and combine the optical systems of the CSS and MIR system. The power of a measured signal of a detection system using one glass beam splitter and one strip-grid beam splitter was increased by approximately 44 – 238 % compared to the previous optical system using two glass beam splitter. Because the transmittance and reflectance of glass beam splitter is ~ 50 % for that of MIR system.

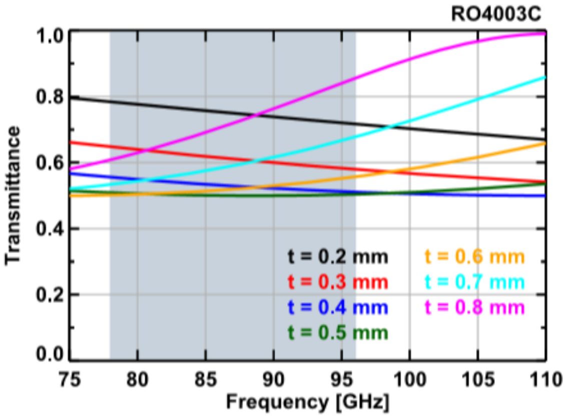

Fig. 3.11 The calculated transmittance as function of frequency for the thickness of the dielectric material from 0.2 to 0.8 mm (assuming S-polarized incident beam and 45 degrees of the incident angle). The shaded region represents the frequency range from 78 – 96 GHz used for the MIR probe beam. [18]

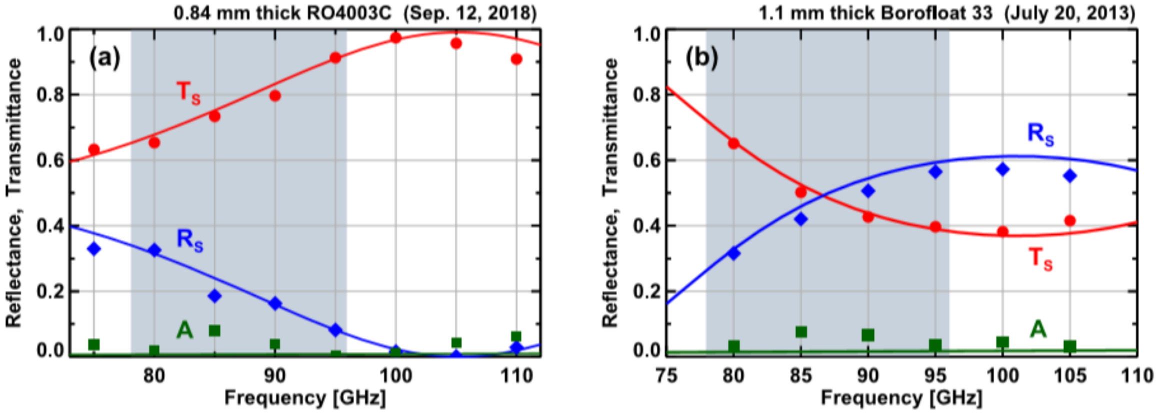

Fig. 3.12 (a) The calculated (curve) and measured (symbols) transmittance, reflectance, and absorptance as a function of frequency from 75 to 110 GHz of the strip-grid beam splitter for X-mode beam. (b) The calculated (curve) and measured (symbols) transmittance, reflectance, and absorptance as a function of frequency from 75 to 110 GHz of a glass beam splitter made of Boroflot33 for X-mode beam. [18]

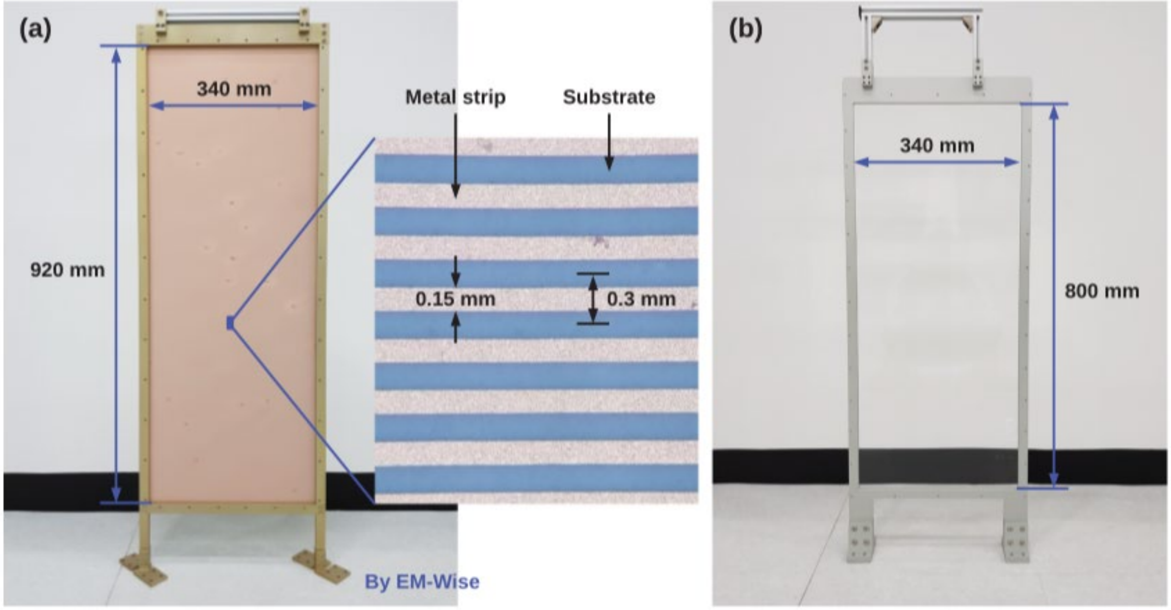

Fig. 3.13 (a) The fabricated strip-grid beam splitter with strip-grid spacing of 0.3 mm and strip width of 0.15 mm on the 0.84 mm thick RO4003C. (b) A glass beam splitter with 1.1 mm thick Borofloat 33. [18]

3.3 The refractive index of lenses and the waist of the 300 GHz probe beam

In order to design the CSS optics using a 300 GHz probe beam, more exact information such as the refractive index of the lenses, the waist radius and waist position of the probe beam source is required. To obtain the waist radius and position of the probe beam source, the 2D beam intensity profiles along the beam propagation were measured as shown in Fig. 3.14. The Z=0 mm position corresponds to the axial distance 400 mm from the probe beam source. The 1/e^2 beam radii in the vertical and horizontal direction were obtained as a function of z using the measured beam intensity profile. The 300 GHz source generates a Gaussian beam and the Gaussian beam radius is given by

$$w(z) = w_0\sqrt{1+\left(\frac{z}{z_R}\right)^2} \tag{3.11}$$

$$z_R = \frac{\pi {w_0}^2 n}{\lambda}, \tag{3.12}$$

where w_0 is the waist radius, z_R is Rayleigh range, and n is the refractive index of the medium in which the beam propagates. The waist radius and waist position (z_0) of the 300 GHz source beams were obtained by fitting Eq. (3.11) to the measured beam radii. The w_{0y} and w_{0x} are 2.90 mm and 2.86 mm, respectively, the $z_{0x,0y}$ is ~ 395 mm which means the beam waist is positioned at a position 5 mm in front of the source antenna.

The refractive index of the lenses used for optics were obtained by using the measured beam radii after a lens. Like the optics of the MIR system, the lenses of the CSS optics were made of High-density Polyethylene (HDPE). Figure 3.15 shows the compared beam radii after a lens between the measurements and calculations in both vertical and horizontal direction. The refractive index of the HDPE lens at 300 GHz can be obtained as ~1.53. Note that in the determination of the refractive index, comparisons in both directions were considered.

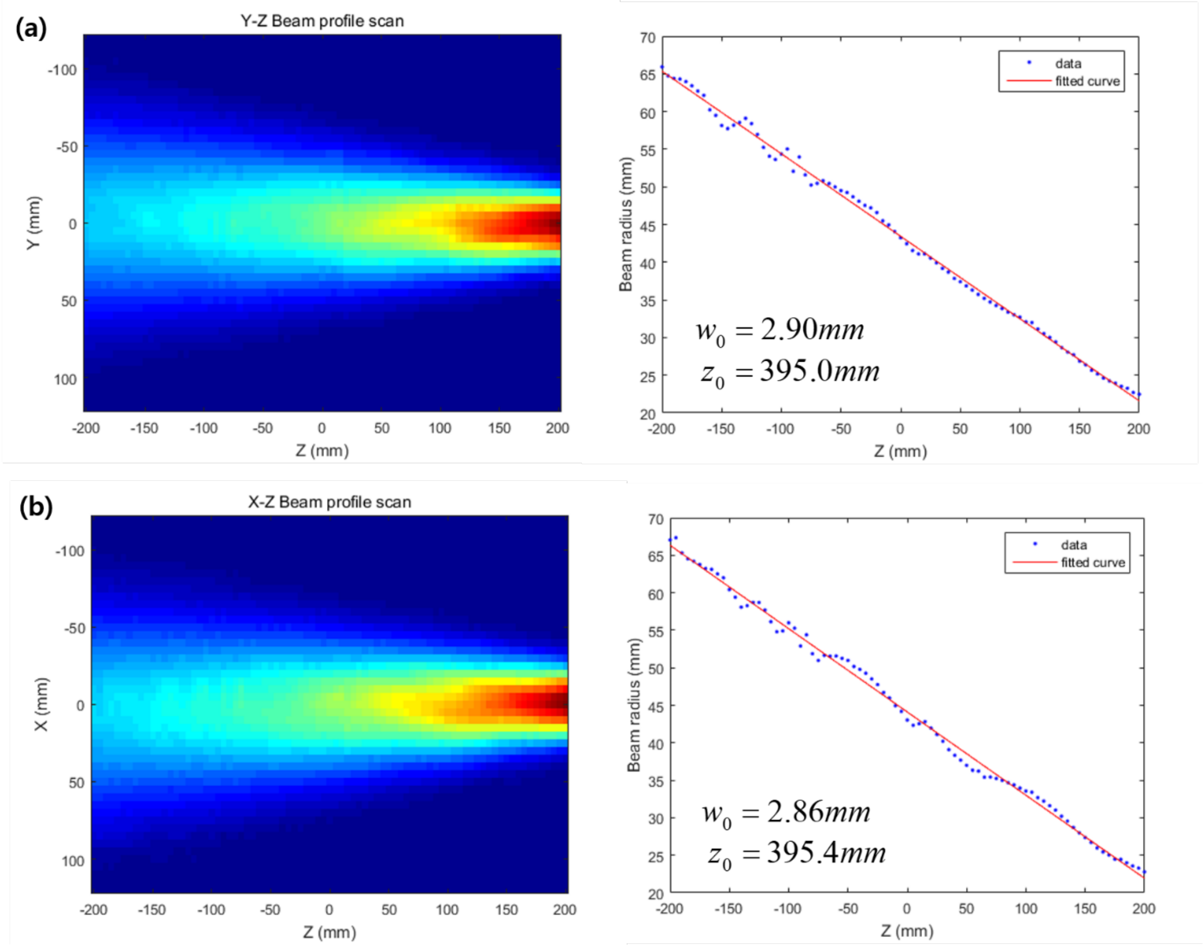

Fig. 3.14 The measured 2D intensity profile of the 300 GHz probe beam source (a) in the Y-Z plane (vertical and axial direction) and (b) in the X-Z plane (horizontal and axial direction). The Z=0 mm position corresponds to the axial distance 400 mm from the source. Note that the beam source is placed on the right.

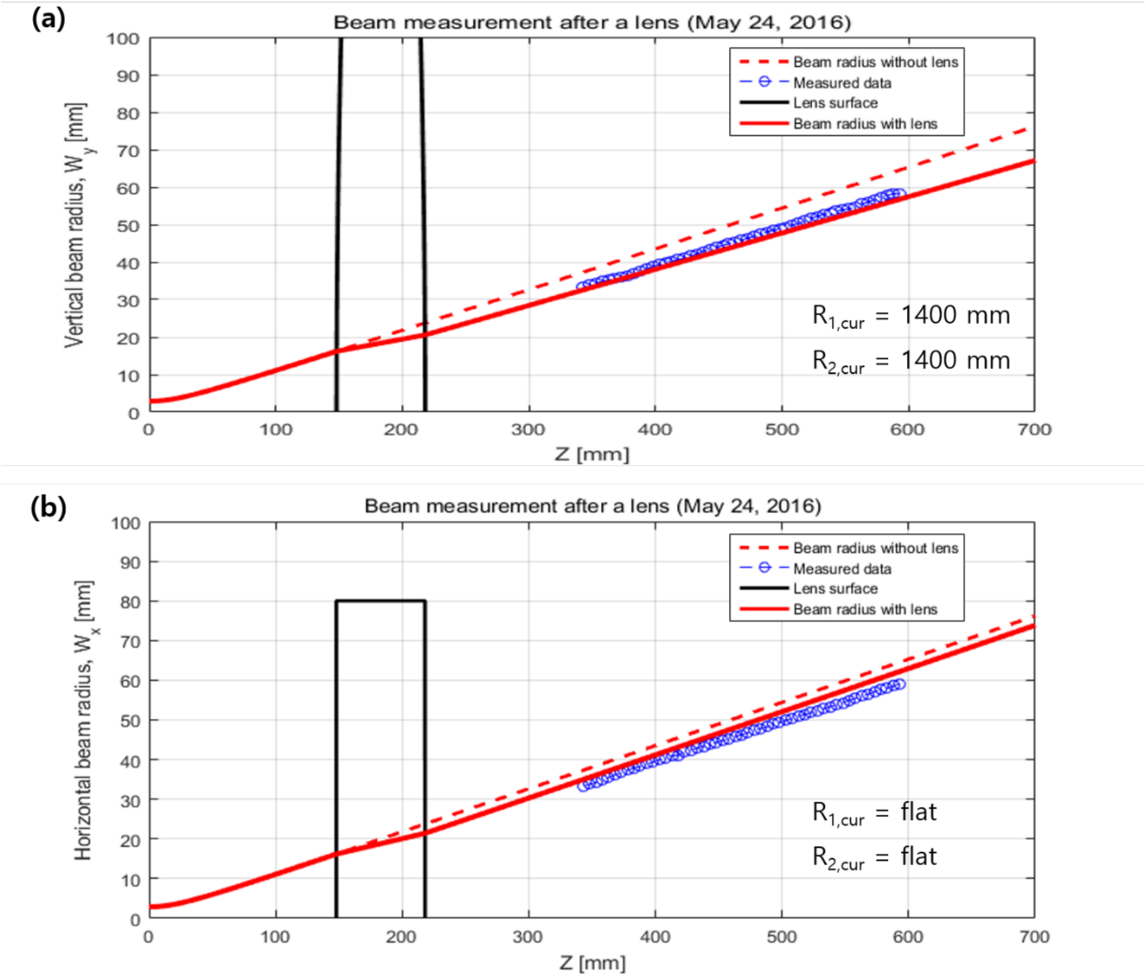

Fig. 3.15 (a) The vertical beam radius (dashed) without lens, and the calculated (solid) and measured (symbol) vertical beam radii after a lens, (b) The horizontal beam radius (dashed) without lens, and the calculated (solid) and measured (symbol) horizontal beam radii after the lens. The lens is made of High-density Polyethylene (HDPE).

3.4 Ray tracing for 300 GHz in KSTAR plasma

No matter how precisely the optical system is designed, it can be difficult to determine the exact scattering angle and scattering volume location if the probe and scattered beams are significantly refracted in the plasma. Hence, it is necessary to calculate how much the probe beam is refracted in the KSTAR plasma, and then the measurement data needs to be corrected through ray tracing calculation. The ray tracing calculation were performed using measured KSTAR plasma parameters and EFIT calculation results. Figure 3.16 shows the probe and scattered beam path through the CSS optics. The red line represents the beam path of the probing optics, and the four blue line represents

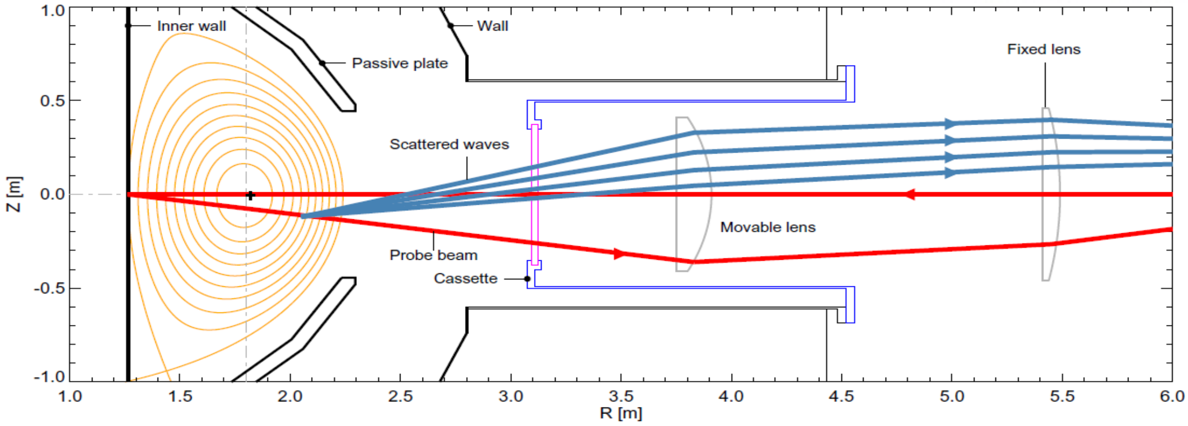

Fig. 3.16 Schematic of the optics of the KSTAR collective scattering system. The Red line is probe beam path, the blue line is four channels scattered beam path.

the paths of the scattered beams at four angles. The Fig 3.17 shows that the 80 GHz O-mode beam is significantly refracted in 1.9 T L-mode plasma. The blue dotted line and solid line are the probing beam path through the vacuum and the plasma, respe-ctively. The red dotted line and solid line are the paths of a scattered beam through the vacuum and the plasma, respectively. Figure 3.18 shows a calculation result of the 300 GHz O-mode beam in 1.8 T H-mode plasma. The difference in the scattering position between the vacuum and plasma cases is approximately 1 mm, and there is almost no difference in scattering angle (< 0.1°). Figure 3.19 shows the calculation result of the 300 GHz H-mode beam in 1.8 T L-mode plasma. The difference in scattering position is about 5 mm, and the difference in scattering angle is about 0.1°. The H-mode plasma has a higher density gradient in the pesestal region than the L-mode plasma, so refraction can be expected, However, the refraction effect can be neligible for the 300 GHz O-mode beam in KSTAR plasmas.

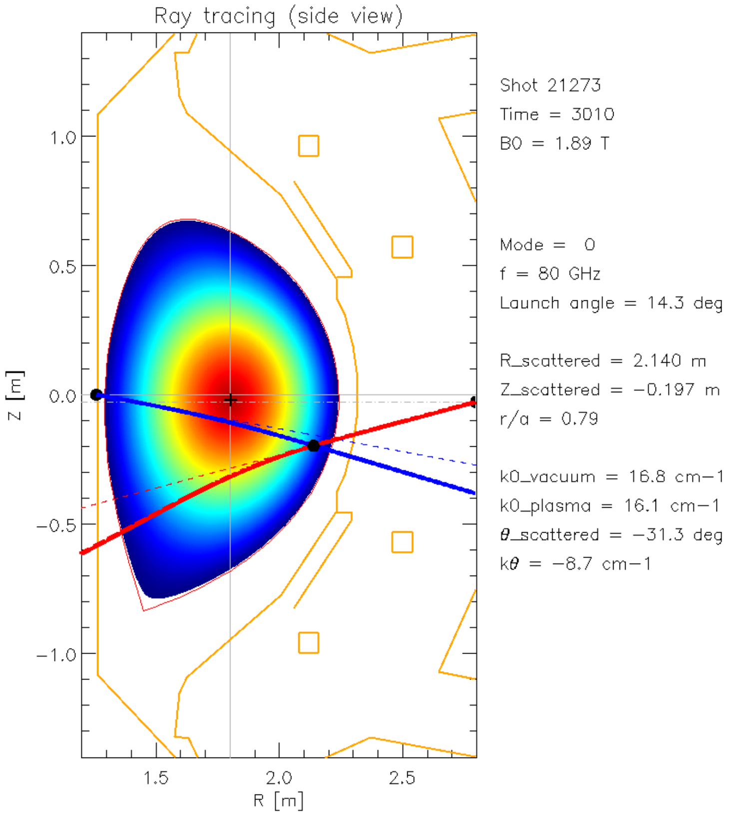

Fig. 3.17 The result of a ray tracing calcuation for 80 GHz O-mode beam in 1.9 T L-mode plasma. The blue dotted line and solid line are the probing beam paths through the vacuum and the plasma, respectively. The red dotted line and solid line are the paths of a scattered beam through the vacuum and the plasma, respectively.

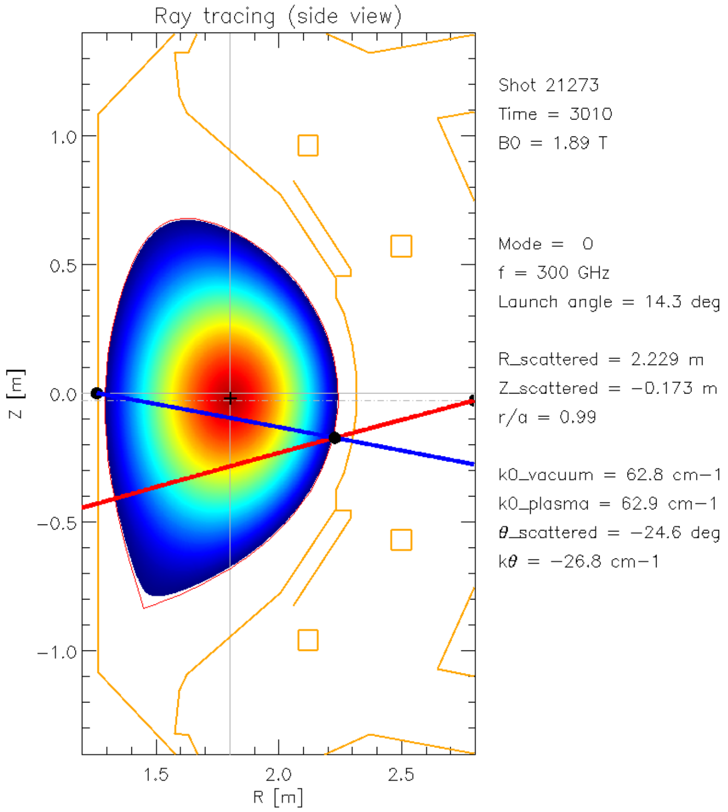

Fig. 3.18 The result of ray tracing calcuation for 300 GHz O-mode beam in 1.9 T L-mode plasma.

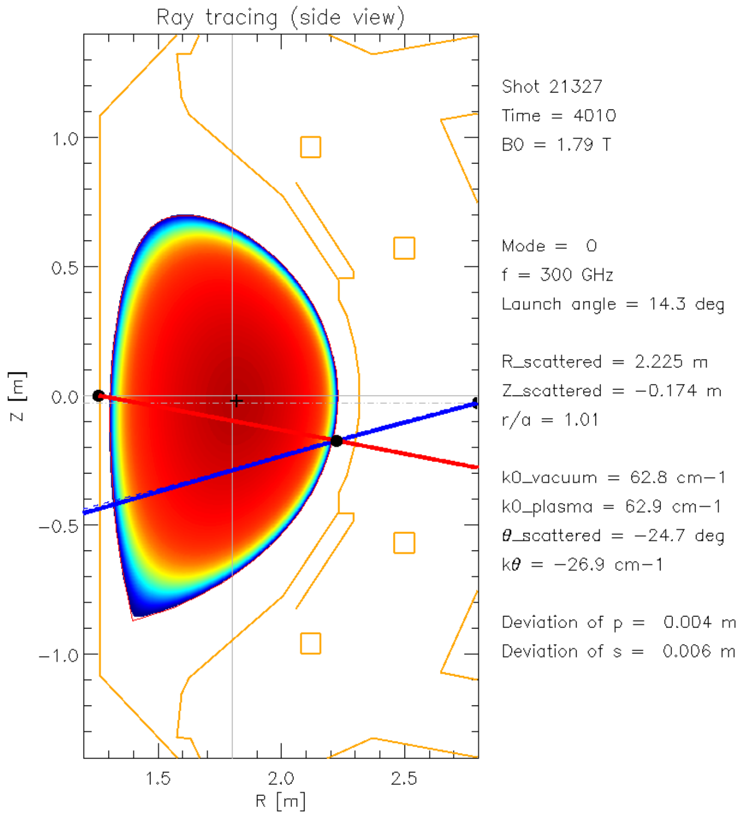

Fig. 3.19 The result of ray tracing calcuation for 300 GHz O-mode beam in 1.8 T H-mode plasma.

Chapter 4

KSTAR collective scattering system

4.1 Overview of the collective scattering system

The KSTAR has various density fluctuation diagnostics for turbulence study as shown in Table 4.1. However, there is no diagnostics capable of measuring turbulence scale of more than 10 cm^{-1}. As previously mentioned, the high-k turbulence above 10 cm^{-1} is known to be associated with anomalous transport induced by ETG mode. In KSTAR, only indirect evidence of existence was reported as a result of simulation regarding ETG mode. Thus, the four channels CSS based on 300 GHz microwave source had been developed and installed in KSTAR to measure the electron gyro-scale fluctuation as shown in Fig 4.1. Since the CSS can be operated simultaneously with the MIR system located in the same port, the two diagnostics can measure evolutions of various turbulences such as ITG mode, TEM, and ETG.

Briefly, the CSS measures scattering signals by injected 300 GHz probe beam at a specific location using the principle described in Chapter 2.1. The scattering caused by small scale density fluctuation can occur anywhere in the path of the probing beam. However, it was designed to measure the scattered beam generated only in a specific area through the optical system. In Fig 4.1, the red line is the probe beam path and yellow line is a scattered beam path. The 300 GHz probe beam is injected into the plasma through the probing optics and reflected from the tilted inner wall. The vertically aligned four detector allow simultaneous measurements of electron density fluctuations with four discrete poloidal wavenumbers in the range from ~14 cm^{-1} to 26 cm^{-1}. The remotely movable optical system can flexibly change the measurement location from the plasma core to outer edge on a shot-by-shot basis, and the fast data acquisition system with the sampling rate of up to 20 MS/s (nominal sampling rate is 10 MS/s) providing the time resolution down to 0.05 μs. The spatial resolution is ~6-10 cm in the radial direction and ~1-2 cm in poloidal direction. The wavenumber resolution is $\Delta k_{\perp}$ ~0.7 cm^{-1} which is based on the probe beam radius of ~ 3 cm near the measurement location. The detectable modes are TEM and ETG mode. The overall system configuration which consists of five parts such as the millimeter wave source, optics, detection system, electronics, and digitizer is shown in Fig. 4.2, and is covered in detail in the following sections.

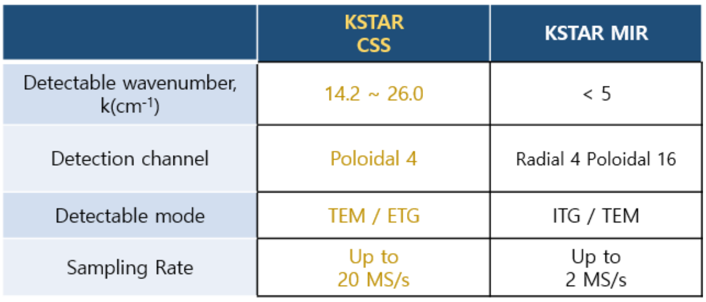

	KSTAR CSS	KSTAR MIR
Detectable wavenumber, k(cm^{-1})	14.2 ~ 26.0	< 5
Detection channel	Poloidal 4	Radial 4 Poloidal 16
Detectable mode	TEM / ETG	ITG / TEM
Sampling Rate	Up to 20 MS/s	Up to 2 MS/s

Table. 4.1 The specification of the KSTAR fluctuation diagnostics.

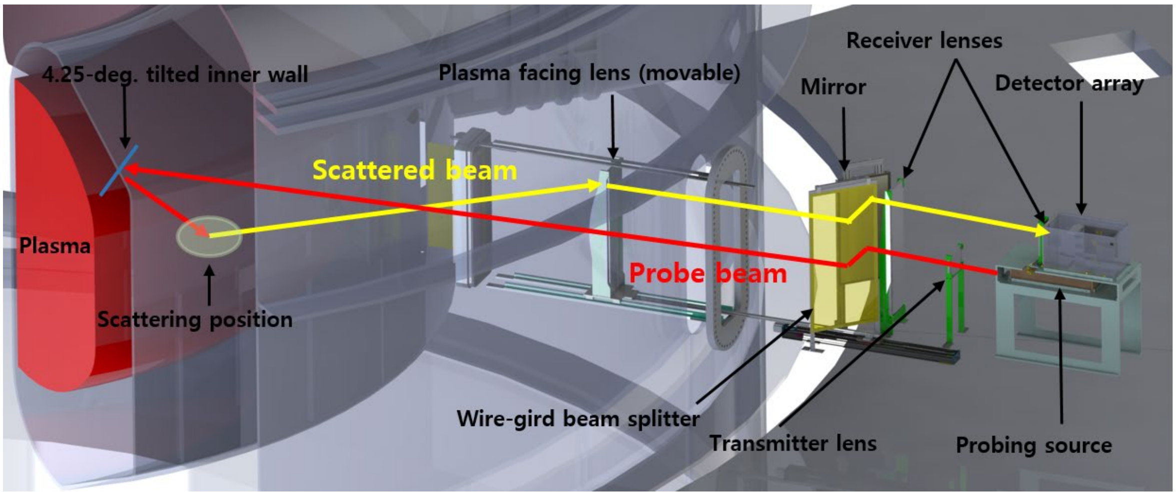

Fig. 4.1 A 3D drawing of the KSTAR collective scattering system.

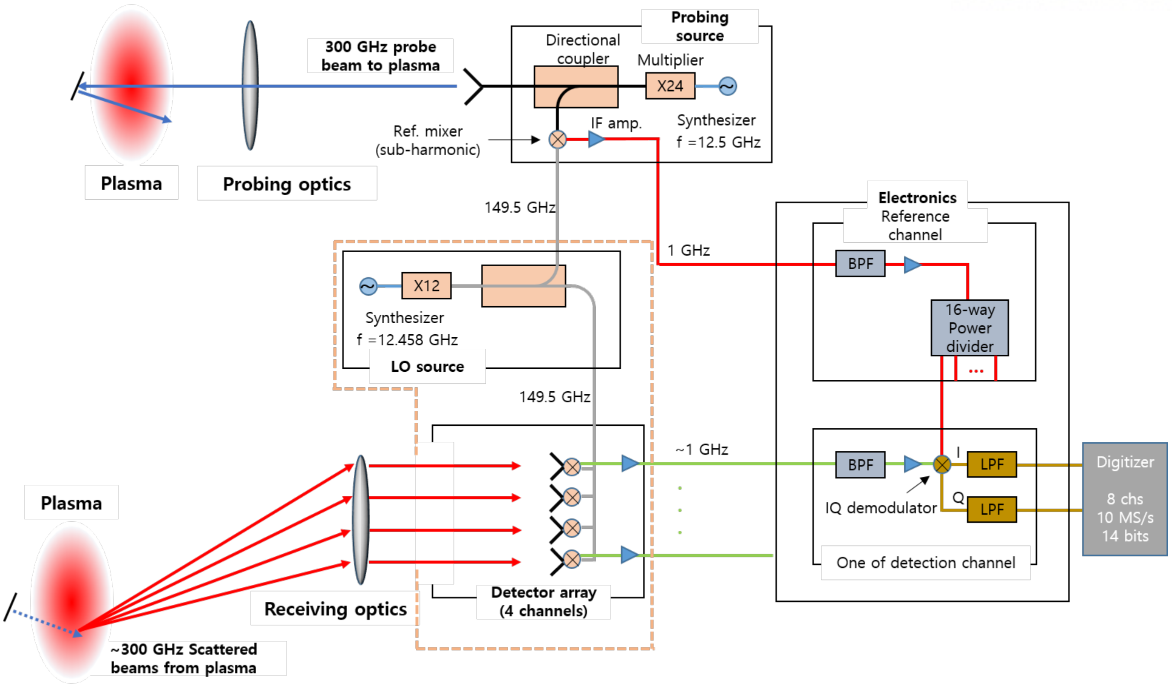

Fig. 4.2 Schematic of the CSS consisting of five part such as millimeter wave source, optics, detection system, electronics, and digitizer.

4.2 The optical system

The CSS optical system was designed with CODE-V which is a commercial optics design software. The source beam waist radius and position, and the refractive index of HDPE at 300 GHz obtained in Chapter 3 were used for the design.

4.2.1 Probing optics

The probing optics consists of three lenses (source lens, second lens, and ‘plasma’ facing lens) and are designed to create a waist of ~3 cm at the measurement location by moving the facing lens. The curvature information of the lenses, and the positions of the strip-grid beam splitter and mirror are shown in detail in Fig 4.3. The facing lens can be moved up to 670 mm and the measurement position can be changed from the plasma core to the outer edge (r/a ~ 0-0.9). Figure 4.4 shows the results of laboratory tests of the probing optics with the fabricated lenses at a measurement position of r/a ~ 0. Figure 4.4 (a) is a 2D beam profile measured by moving a detector in 2D plane (vertical and axial direction). Figure 4.4 (b) shows the comparison of the vertical beam radius between measurement and calculation with CODE-V. Figures 3.4 (c) and (d) show the measured and calculated 2D (vertical and horizontal) beam profiles, respectively. The measured results show good agreement with the results calculated in CODE-V.

4.2.1 Receiving optics

The receiving optics consists of four lenses (facing lens, second lens, compensate lens, and mini lens). Among them, the second lens and facing lens are shared with the probing optics. The measurement position is changed by moving only one lens, the facing lens as shown in Fig 4.5. In addition, it is important to properly design the curvature and position of the facing lens because the Facing lens also shares with the optics of the MIR system. Because the antenna of the detectors is the same with that of the probe beam source, the receiving optics was designed with the waist of ~2.3 mm. Compensate lens is a lens with four different curvatures vertically that allow the scattered beams to enter the detector antennas in the direction perpendicular to the entrance surface. The scattering angles are 12.8, 16.5, 18.3, and 23.9 degrees for a measurement position at r/a ~ 0.5 and they correspond to the wavenumbers of ~14, ~18, ~20, and 26 cm^{-1}. Figure 4.6 shows the results of laboratory tests on CH.4 with the largest scattering angle at a measurement position (r/a ~ 0). Figure 4.6 (a) shows the measurement of the 2D beam profile in the Y-Z (vertical and axial) direction. Figure 4.6 (b) shows the comparison of the beam center position between measurement and calculation. The slopes of the graph are associated with the scattering angles and agree well with each other. Figures 4.6 (c) and (d) show the measured and calculated 2D beam profile in Y-X (vertical and horizontal) direction. The beam shape is similar, but the vertical size of measured beam is slightly longer than that of the calculated beam, which is probably due to diffraction effect, is largest in the CH.4 in which the beam passes through the upper edge of the lens.

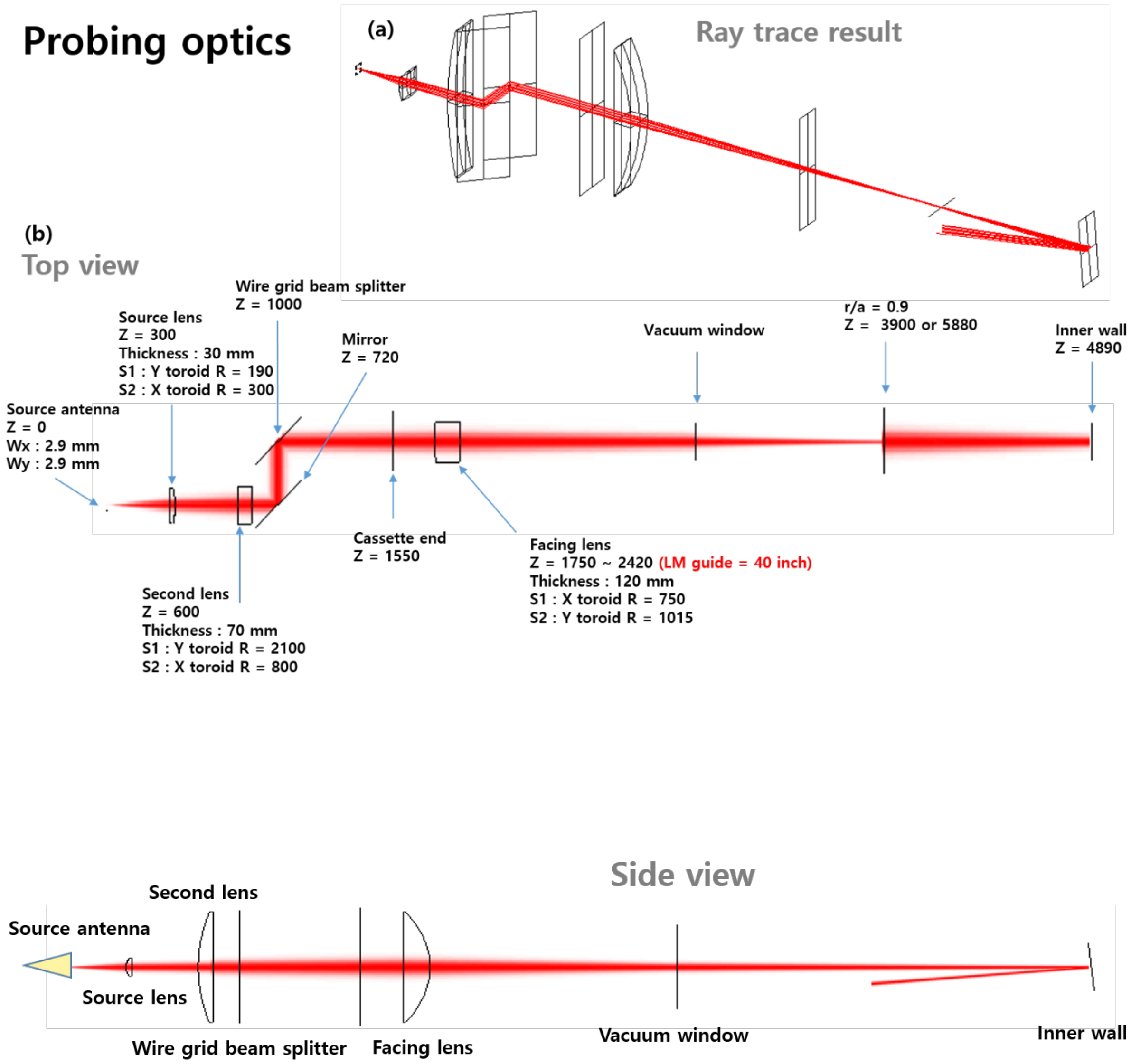

Fig. 4.3 (a) Ray tracing calculation result of the probing optics, (b) Gaussian beam calculation result of the probing optics (top view), with information of three lenses and other optics components, (c) Gaussian beam calculation result of the probing optics (side view).

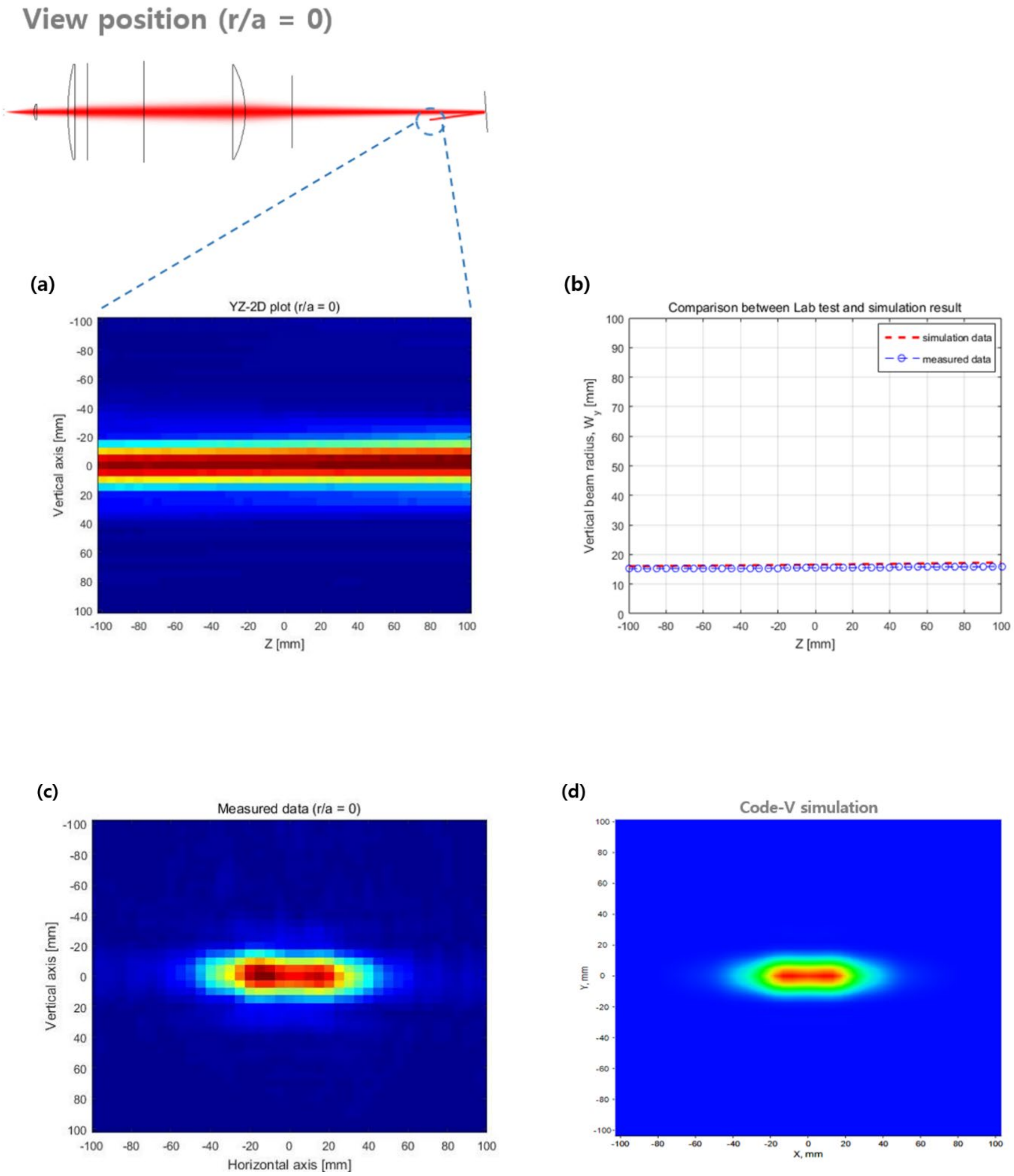

Fig. 4.4 (a) Measured 2D beam profile in the vertical and axial direction, and (b) compared beam radius between measurement (symbol line) and calculation (dotted line). (c) Measured 2D beam profile vertical and horizontal direction, (d) calculated 2D beam profile in the same plane.

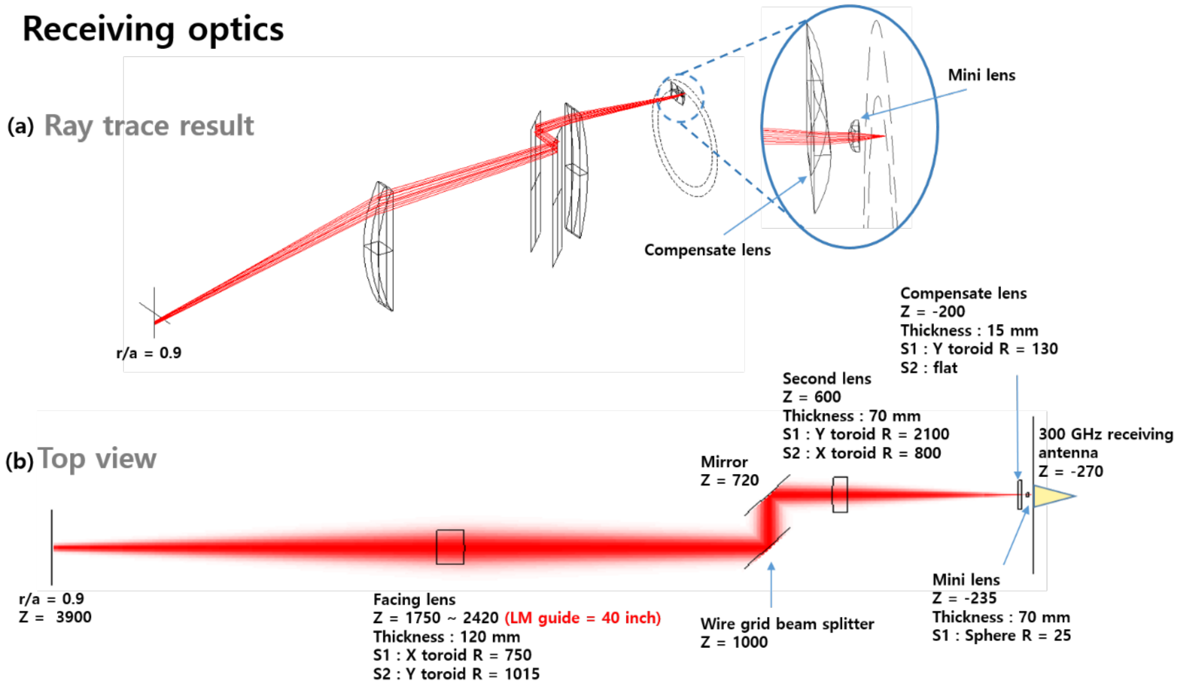

Fig. 4.5 (a) Ray tracing result of the receiving optics, (b) Gaussian beam calculation of the receiving optics (top view), with information of the lenses and other optics components.

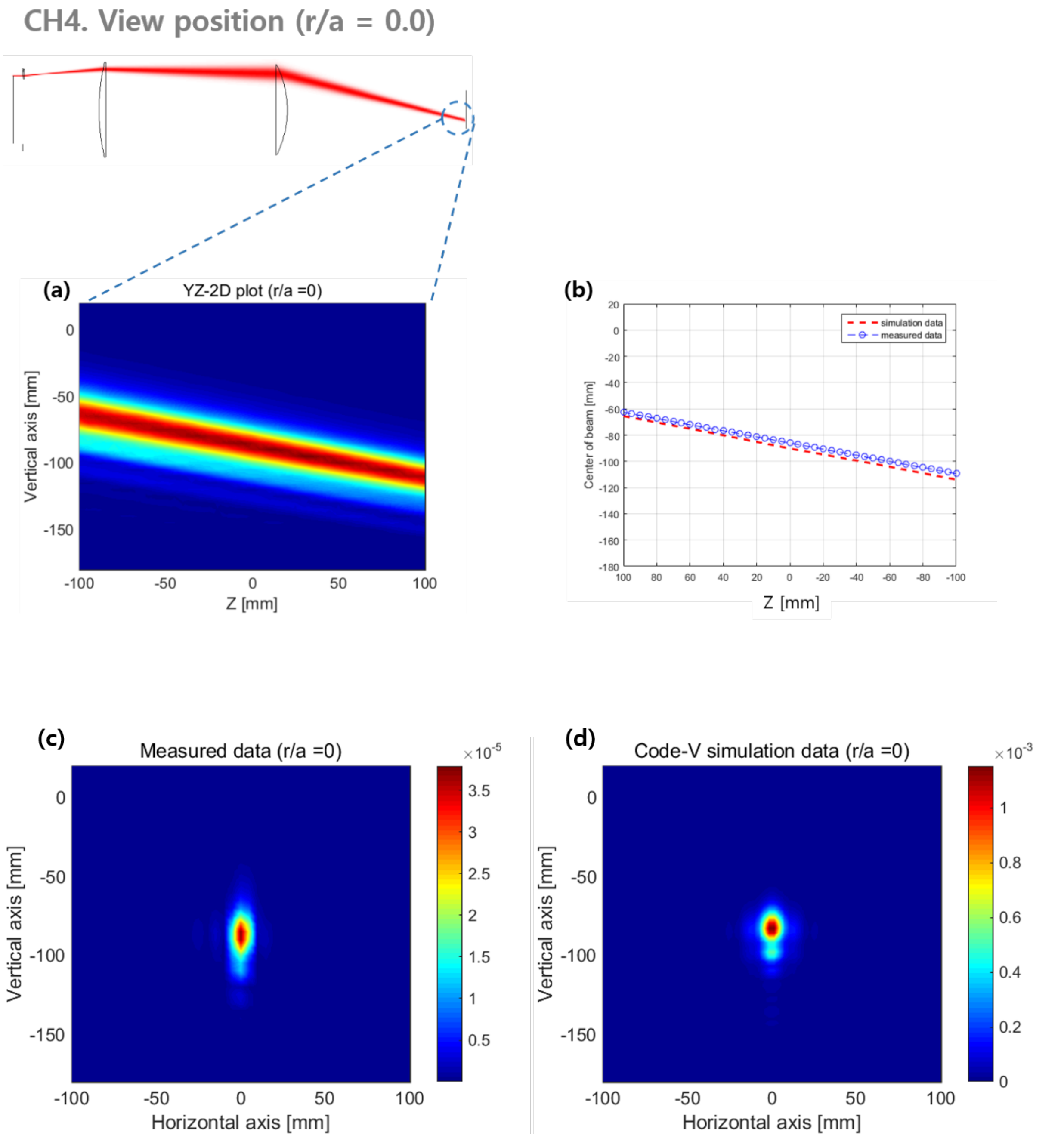

Fig. 4.6 (a) Measured 2D beam profile in the vertical and axial direction, and (b) compared beam radius between measurement (symbol line) and calculation (dotted line) of center of beam. (c) Measured 2D beam profile in the vertical and horizontal direction, and (d) calculated 2D beam profile in the same plane.

4.3 Millimeter wave source

4.3.1 300 GHz beam source

The probing source (made by Virginia Diodes, Inc.) provides ~ 40 mW (~16 dBm) output power at 300 GHz. It is composed of a 12.5 GHz source and x24 multiplier chain, which consists of a tripler and three doublers. The specifications of the multiplier chain is shown in Table. 4.2 and the output power is shown in Fig. 4.7. The output power of the 300 GHz source is transmitted to the antenna with ~23 mW (~13.5 dBm) power through a 20 dB-directional coupler (with insertion loss of ~ 2.5 dB) as shown in Table 4.3 and to the Ref. mixer with <0.3 mW (<-6 dBm) power. Figure 4.8 shows the configuration of the assembled probing source.

Description		Specification	Connector
RF Output	Frequency Range	295 – 305 GHz	WR-3.4
	Output power	~40 mW	
RF Input	Frequency Range	12.3 – 12.7 GHz	SMA(f)
	Power (Typical / Damage)	7 to 13 dBm / 16 dBm	
	Multiplication Factor	24	

Table. 4.2 Specifications of the x24 multiplier chain for the 300 GHz probing source.

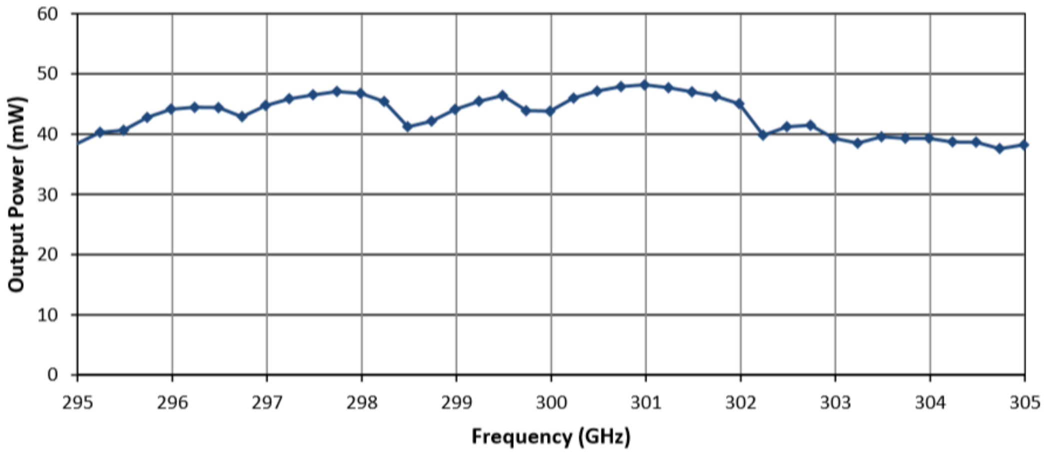

Fig. 4.7 The output power of the x24 multiplier chain for the input power of ~ 10 dBm.

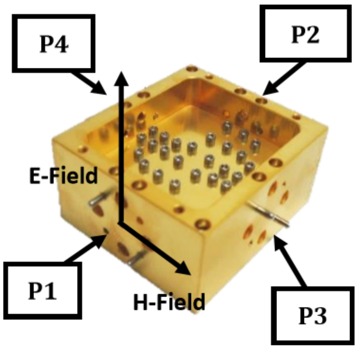

Parameter	Specifications
Incident Port [P1]	220-330GHz [WR3.4 UG-387/UM]
Through Port [P2]	
Coupled Port [P3]	
Isolated Port [P4]	
Directivity	~20dB
Insertion Loss (P1/P2)	~2.5dB
Coupling Factor	~20dB (P1/P3), 10dB (P2/P4)
Divisional Ratio	~17.5dB (P2/P3), 7.5dB (P1/P4)

Table. 4.3 Specifications of the 20 dB directional couplers.

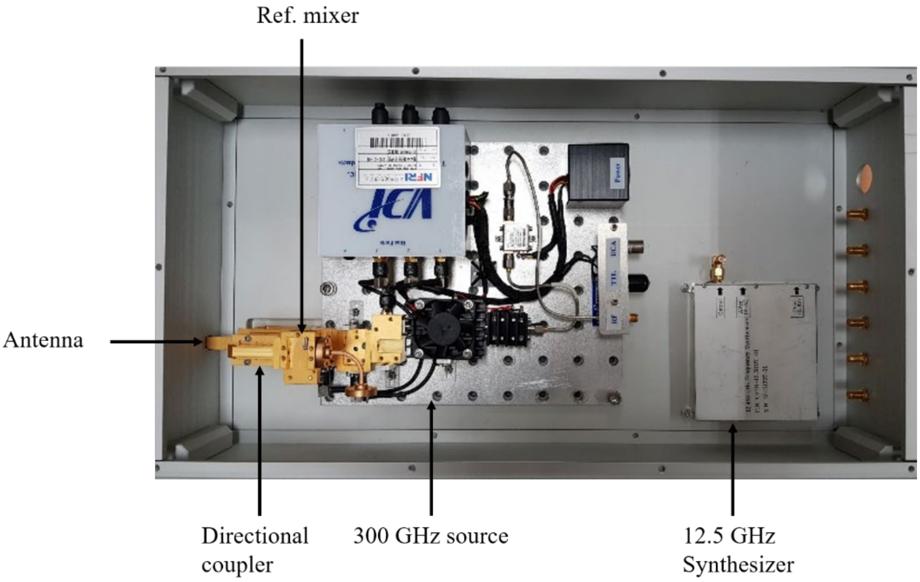

Fig. 4.8 Configuration of the 300 GHz probing source.

4.3.2 149.5 GHz local oscillator (LO) source

The Reference mixer and the detector of the detection system use the sub-harmonic mixer, and the intermediate frequency (IF) is 1 GHz, and thus the frequency of the LO source is 149.5 GHz. The LO source is composed of a 15 dB-directional coupler x12 multiplier chain with a tripler and two doublers, and 12.458 GHz input source. The specifications of the x12 multiplier chain are shown in Table. 4.4 and Fig 4.10. The 150 mW output power coming out of the main port is distributed to 4 detectors by three hybrid couplers, and the 5 mW output power coming out of the coupling port is transmitted to the Ref. mixer located in the probing source box by waveguides.

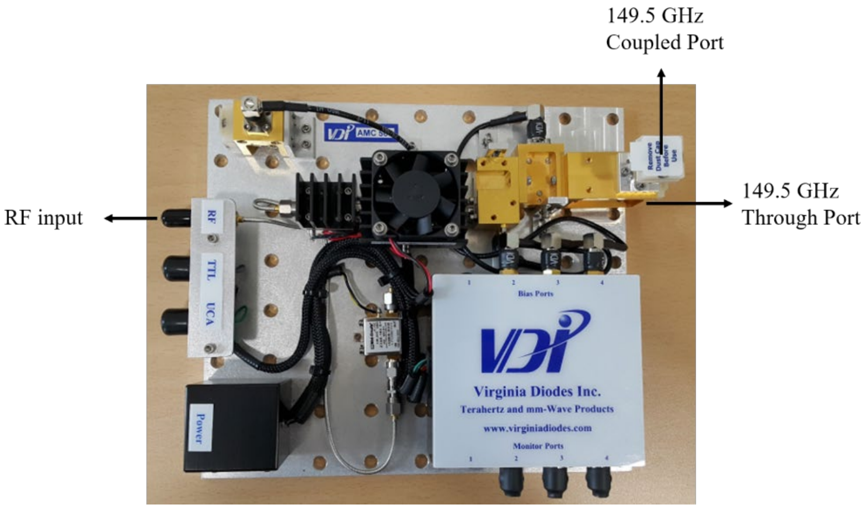

Fig. 4.9 The x12 multiplier chain for the local oscillator (LO) source.

Description		Specification	Connector
RF Output - Through Port	Frequency Range	147.5 – 152.5 GHz	WR-6.5
	Output power	150 mW	
RF Output - Coupled Port	Frequency Range	147.5 – 152.5 GHz	WR-6.5
	Output power	5 mW	
RF Input	Frequency Range	12.3 – 12.7 GHz	SMA(f)
	Power (Typical / Damage)	7 to 13 dBm / 16 dBm	
	Multiplication Factor	12	

Table. 4.4 Specifications the x12 multiplier chain for the 149.5 GHz LO source.

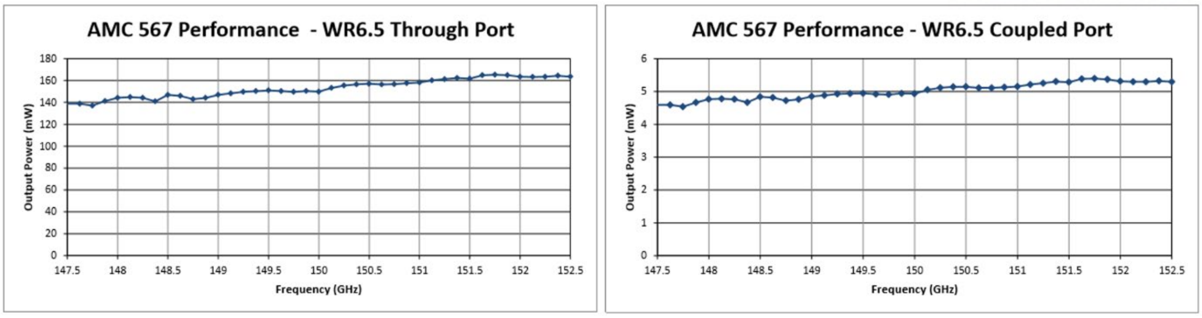

Fig. 4.10 Output powers of the main port (left) and the coupling port (right) of the x12 multiplier chain for the input power of ~ 10 dBm.

4.3.3 Synthesizer

The synthesizer, which is mainly used for plasma diagnostics, uses the phase locked loop (PLL) method which is a feedback control system. It compares the phases of two input signals and produces an error signal that is proportional to the difference between their phases. The error signal is low pass filtered and used to drive a voltage-controlled oscillator (VCO) which creates an output frequency. The output frequency is fed through a frequency divider back to the input of the system, producing a negative feedback loop. If the output frequency drifts the phase error signal will increase, driving the frequency in the opposite direction so as to reduce the error. Thus the output is locked to the frequency at the other input. This other input is called the reference (10 MHz) and is usually derived a crystal oscillator, which is very stable in frequency.

The CSS synthesizers used for the RF input of LO and probing source were developed by EM-Wise. The 12.5 GHz and 12.4583 GHz synthesizers have a fixed output frequency and were designed to meet the RF input power requirements of <+6 dBm. The phase noise and harmonic characteristics are shown in Fig 4.11 and Table 4.5.

Parameter	Specification		Parameter		Specification
Output frequency	12.5 / 12.4583 GHz		Phase Noise	@ 1 kHz	-74 / -65 dBc/Hz
Output power	>+6 dBm			@ 10 kHz	-82 / -73 dBc/Hz
Harmonic (2f)	< -48 dBc			@ 100 kHz	-111 / -111 dBc/Hz
Locking Time	180 μs			@ 1 MHz	-133 / -134 dBc/Hz

Table. 4.5 Specification of the 12.5 GHz and 12.458 GHz synthesizer.

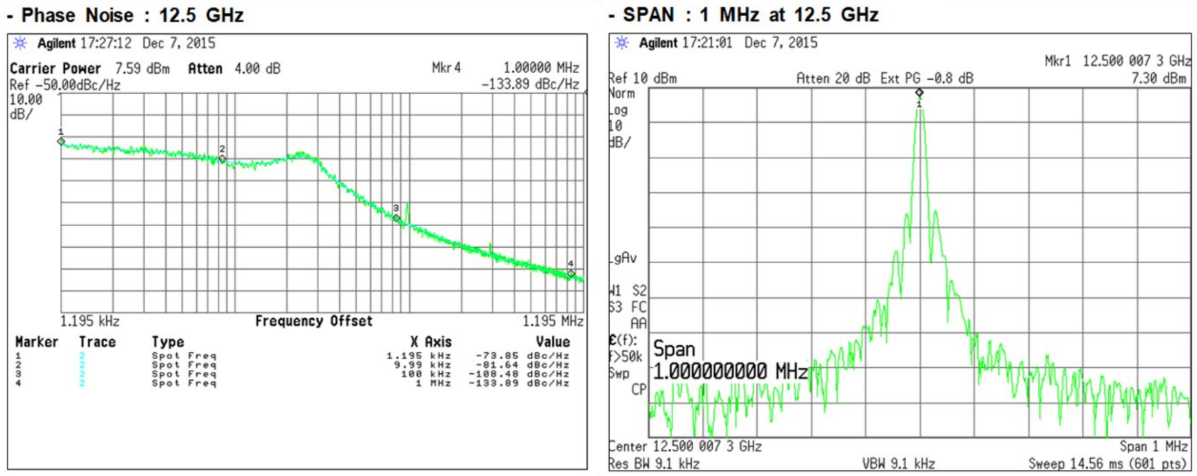

- Phase Noise : 12.5 GHz

- SPAN : 1 MHz at 12.5 GHz

Marker	Trace	Type	X Axis	Value
1	2	Spot Freq	1.195 kHz	-73.85 dBc/Hz
2	2	Spot Freq	9.99 kHz	-81.64 dBc/Hz
3	2	Spot Freq	100 kHz	-108.48 dBc/Hz
4	2	Spot Freq	1 MHz	-133.89 dBc/Hz

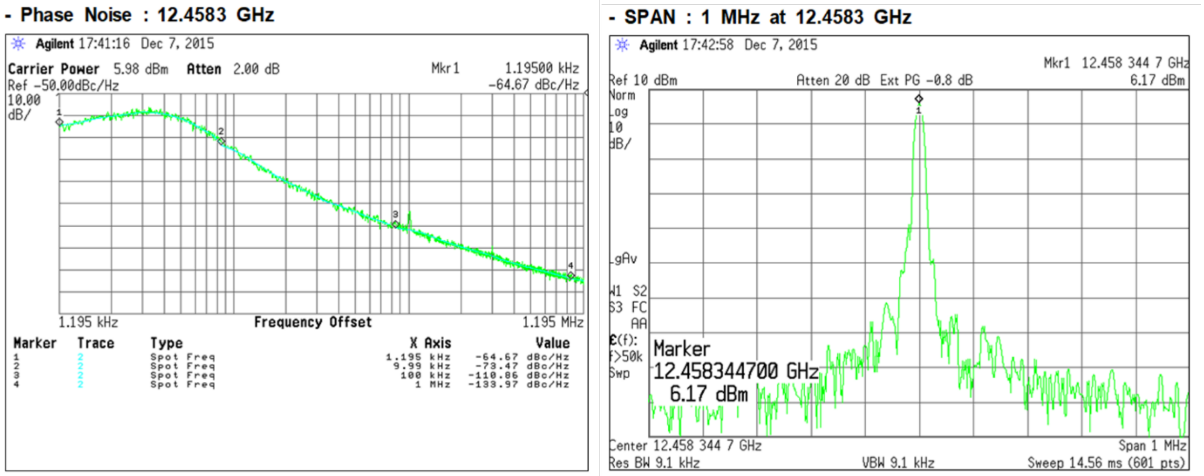

- Phase Noise : 12.4583 GHz

- SPAN : 1 MHz at 12.4583 GHz

Marker	Trace	Type	X Axis	Value
1	2	Spot Freq	1.195 kHz	-64.67 dBc/Hz
2	2	Spot Freq	9.99 kHz	-73.47 dBc/Hz
3	2	Spot Freq	100 kHz	-110.86 dBc/Hz
4	2	Spot Freq	1 MHz	-133.97 dBc/Hz

Fig. 4.11 Phase noise and output power of the 12.5 GHz and 12.4583 GHz synthesizer.

4.4 Heterodyne detection system

Most RF or micro-wave diagnostics use heterodyne detection system. The heterodyne detection system is a system that down or up converts a measured signal to another frequency signal. In the most common application, two signals at frequencies f_1 (measured signal) and f_2 (LO signal) are mixed, creating two new signals; one at the sum of the two frequencies f_1+f_2 and the other at the difference between the two frequencies f_1-f_2. The new signal frequencies are called heterodynes. Typically, only one of the two heterodynes is used and the other signal one is filtered out. Although the carrier frequency (f_1) changes, the information to be transmitted is not changed. Plasma diagnostics mainly use the down conversion method. This is because the frequency ranges of measured signals is from several tens of GHz to several hundreds of GHz. Such higher frequency signals can be easily exposed to various noise and losses while being transmitted to the signal processing unit. Moreover, it is easier to process signals at lower frequency than higher frequency.

In the CSS, a four channel heterodyne detection system detects scattered beams with vertically aligned sub-harmonic mixers with low noise temperature and low conversion loss. The LO signal (~150 mW) is transmitted by three hybrid couplers and waveguide, divided into four signals, and then each signal with <6 mW power is transmitted to the sub-harmonic mixer. The scattered beams (~ 300 GHz) are combined with the LO signal (149.5 GHz) in the sub-harmonic mixer and down converted into ~1 GHz IF signals. Each IF signal is amplified by 32 dB by amplifier (Ciao-wireless, CA12-3001) with low noise figure of ~ 0.8 dB and transmitted to the signal processing electronics through 20 m low-loss broad-band cable. The configuration of the heterodyne detection system is shown in Fig 4.12. The detailed specifications of the sub-harmonic mixer are shown in Table 4.6.

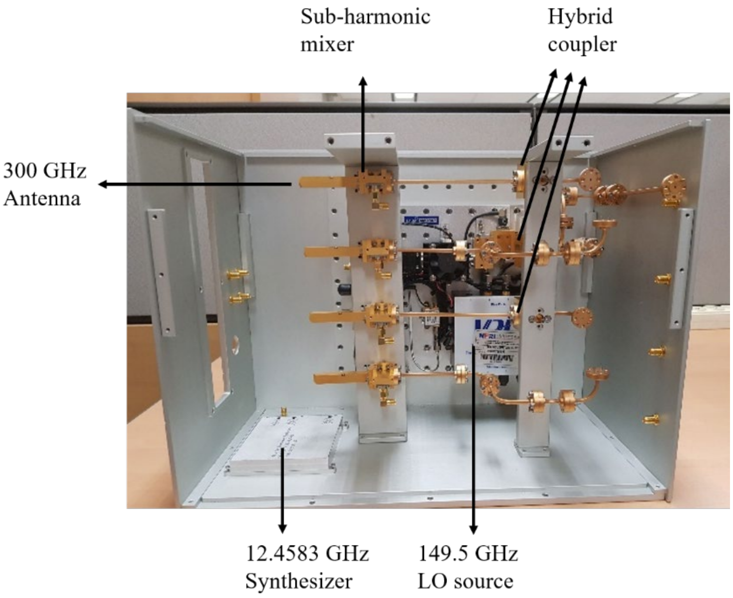

Fig. 4.12 A four channels heterodyne detection system.

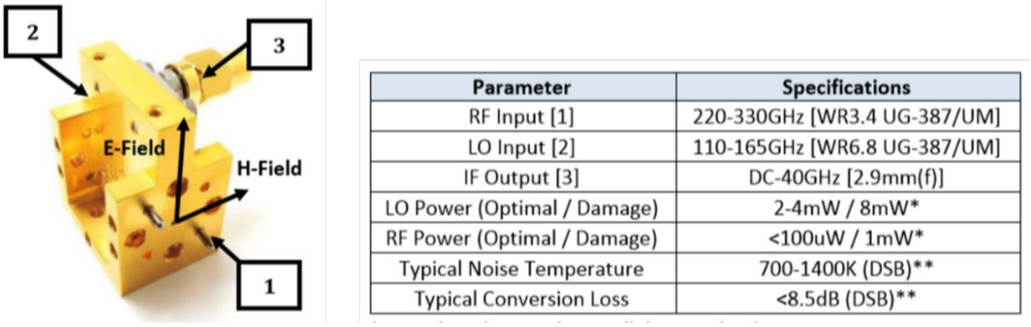

Parameter	Specifications
RF Input [1]	220-330GHz [WR3.4 UG-387/UM]
LO Input [2]	110-165GHz [WR6.8 UG-387/UM]
IF Output [3]	DC-40GHz [2.9mm(f)]
LO Power (Optimal / Damage)	2-4mW / 8mW*
RF Power (Optimal / Damage)	<100uW / 1mW*
Typical Noise Temperature	700-1400K (DSB)**
Typical Conversion Loss	<8.5dB (DSB)**

Table 4.6 Specifications of the sub-harmonic mixer used for the detection system.

4.5 Electronics

To obtain the phase information from the scattered beam, the electronics, which has Inphase and quadrature (I/Q) demodulator, is employed. The I/Q demodulator separates the measured IF signal based on the Ref. IF signal into I and Q signal. By convention, the I signal is a cosine waveform, and the Q signal is a sine waveform. The relationship between I/Q signal and phase is given by the following equation.

$$\text{Phase [radian]} = \arctan\left(\frac{Q}{I}\right) \tag{4.1}$$

The Ref. IF signal and the IF signal from scattered beam are separated into inphase and quadrature signals in the I/Q demodulator, and the propagation direction of the measured fluctuations can be determined by analyzing the I/Q signals. For the CSS electronics, the old 16-channel electronics of the MIR system is used after extending the video bandwidth from 1 MHz to 4 MHz. Figure 4.13 shows a picture of the electronics and measured IF and video bandwidths.

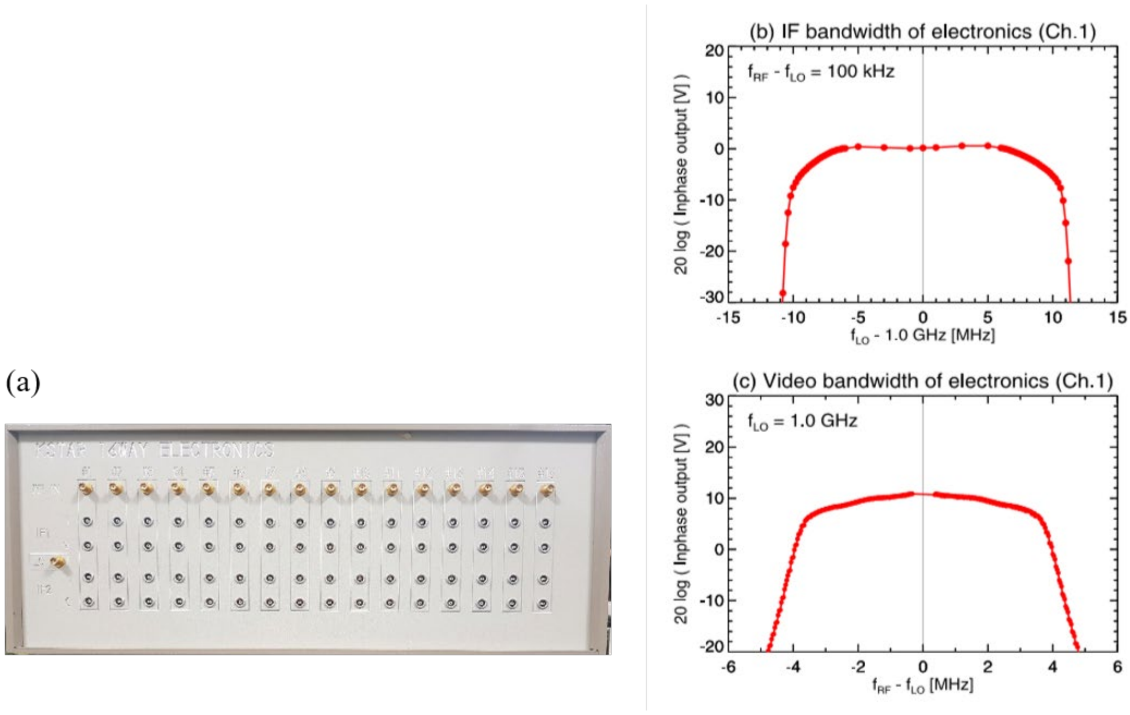

Fig. 4.13 (a) A 16-channel CSS electronics. (b) Measured IF bandwidth (~20 MHz) and (c) video bandwidth (f_{cut} ~ 4 MHz) of the electronics. [5]

4.6 Digitizer

The digitizer converts measured analog signals into digital signals. High-speed digitizers can capture fast events and high-frequency fluctuations. This is crucial when capturing rare events, explosive events, and high-frequency turbulence. Scattered signals are sampled at the sampling rate up to 20 MS/s (nominal 10 MS/s) by a digitizer (D-tAcq ACQ2106) with a host bus adapter (D-tAcq AFHBA404) and buffer server, which enable to record the signals for full pulse lengths of discharges without limitation of a fixed on board memory of the digitizer. The digitizer has 8 input channels, and the input voltage range is ± 2.5 V with 14 bit resolution. Typical data size is about several Gigabytes for 8 channel signals from ~10 s discharge.

Fig. 4.14 An 8-channel CSS digitizer with nominal sampling rate of ~10 MS/s.

Chapter 5

Small-scale turbulence study

5.1 Small-scale turbulence in KSTAR plasmas

The CSS was first installed in the late 2018 KSTAR campaign, and formal operation began in the 2019 KSTAR campaign. We have obtained CSS data from various plasma discharges, and will present CSS spectrograms for several plasmas such as H-mode and L-mode plasma. As shown in Fig 5.1, shot 21357 is a typical H-mode plasma made at the magnetic field B_t = 1.8 T and plasma current I_p = 700 kA, and the plasma was heated by 1.9 MW and 0.4 MW neutral beam injection (NBI) and 0.6 MW electron cyclotron resonant heating (ECH) at 105 GHz. The measurement position of CSS is R~210 cm (r/a~0.6). The CSS spectrogram after the L-H transition at 2 seconds shows a high-k turbulence reduction, which is similar to the experimental results from other Tokamak plasmas. Here, the negative (positive) frequency corresponds to fluctuations propagating in ion (electron) diamagnetic direction. What is noticed here is that the sawtooth activity occurs in the plasma core (seen from the core electron temperature) by the 105 GHz ECH and the turbulence spectrum gets slightly broader, which can be explained by increased plasma rotation speed after the L-H transition. Shot 21327 is also an H-mode discharge which was made at B_t = 1.8 T and I_p = 700 kA, and heated by 1.6 MW NBI and 1.4 MW ECH. The measurement position of CSS is R~225 cm in the pedestal area. A much greater reduction in high-k turbulence than in the H-mode core region is observed in shown Fig 5.2. Furthermore, after the RMP was applied in 5 seconds, and weak quasi-coherent turbulence around 300 kHz disappeared. Compared to the previous shot (21357) in which there was no response to the RMP, the RMP effect looks to be limited in the edge region.

The shot 21273 is an L-mode plasma which was made at the magnetic field B_t = 1.9 T and plasma current I_p = 550 kA, and heated by 1.0 MW NBI, and the CSS measurement position is

R~205 cm. After the plasma current ramp-up is finished, the CSS spectrogram is broadened to ~1.5 MHz in the negative frequency and the broad fluctuation is reduced as the sawtooth instability occurs in the core region. Also, Top RMP was applied at 3.5 s, but there was no response, and when applying Mid RMP at 4 s, fluctuation of the positive on the CSS spectrogram almost disappeared. This result may imply that the RMP field from the middle-row coils more effectively penetrates into the plasma than that from the top- or bottom-row coils.

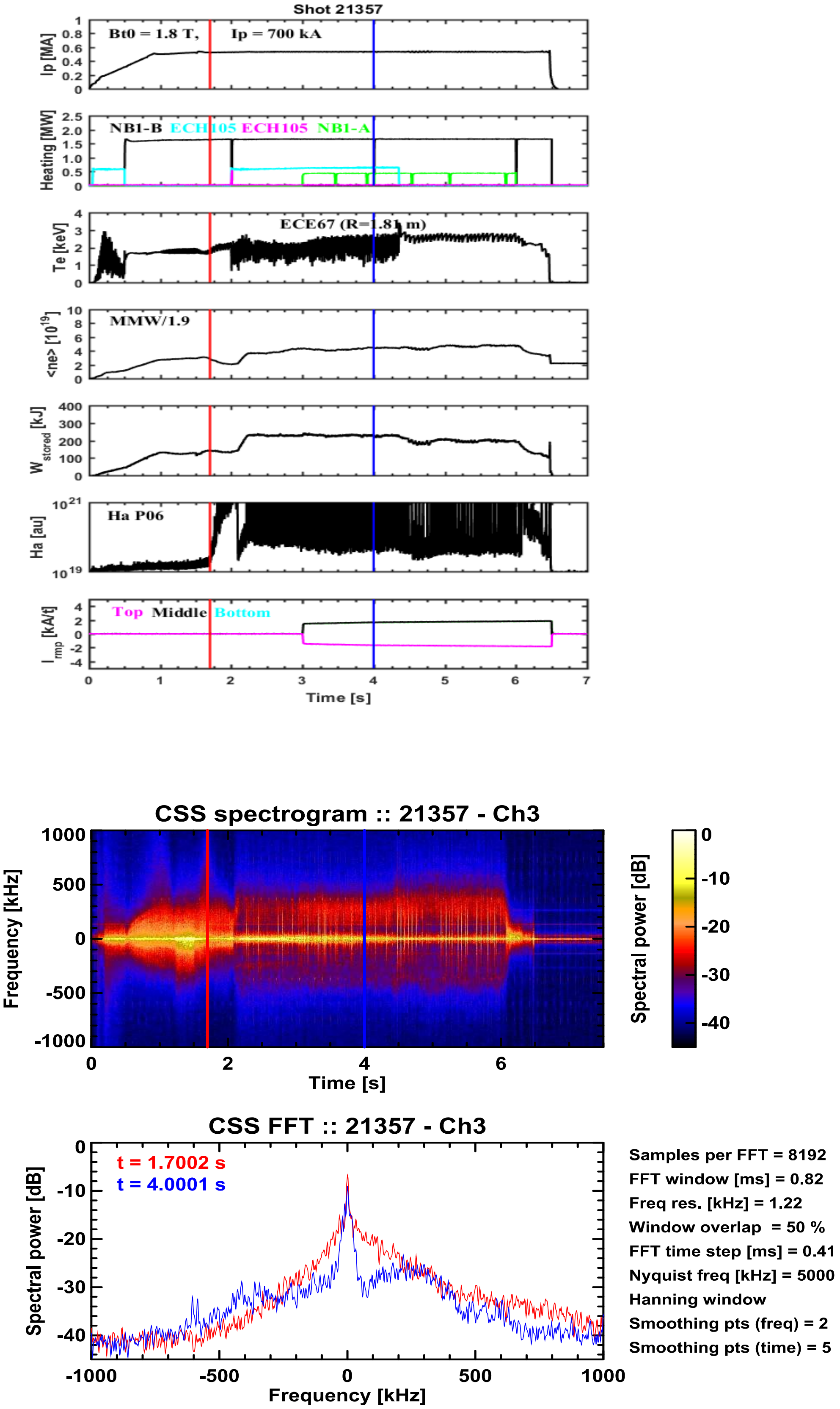

Fig. 5.1 Plasma parameter and CSS spectrogram on CH.3 of Shot 22357 in H-mode plasma core.

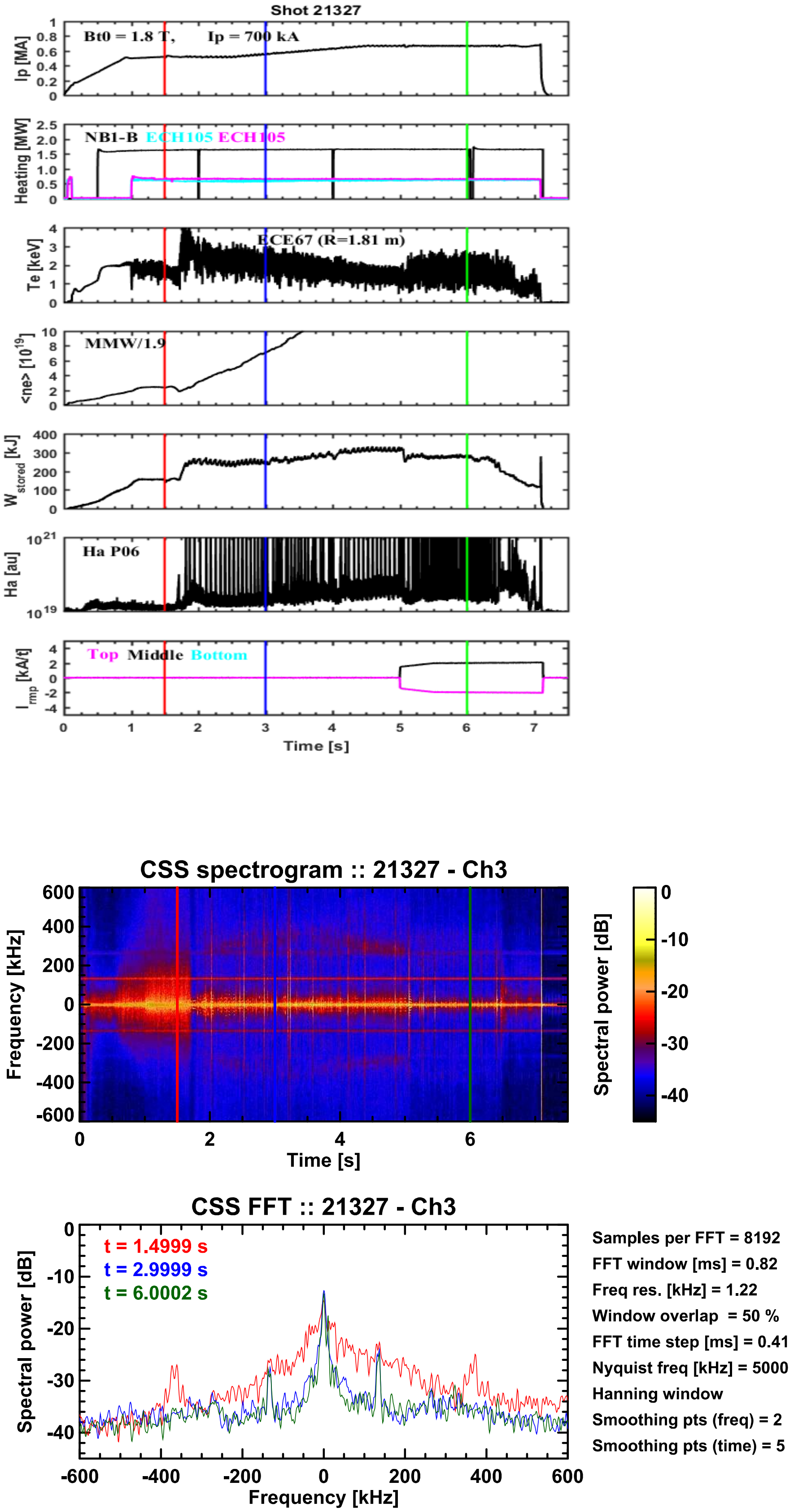

Fig. 5.2 Plasma parameter and CSS spectrogram on CH.3 of Shot 21327 in H-mode plasma edge.

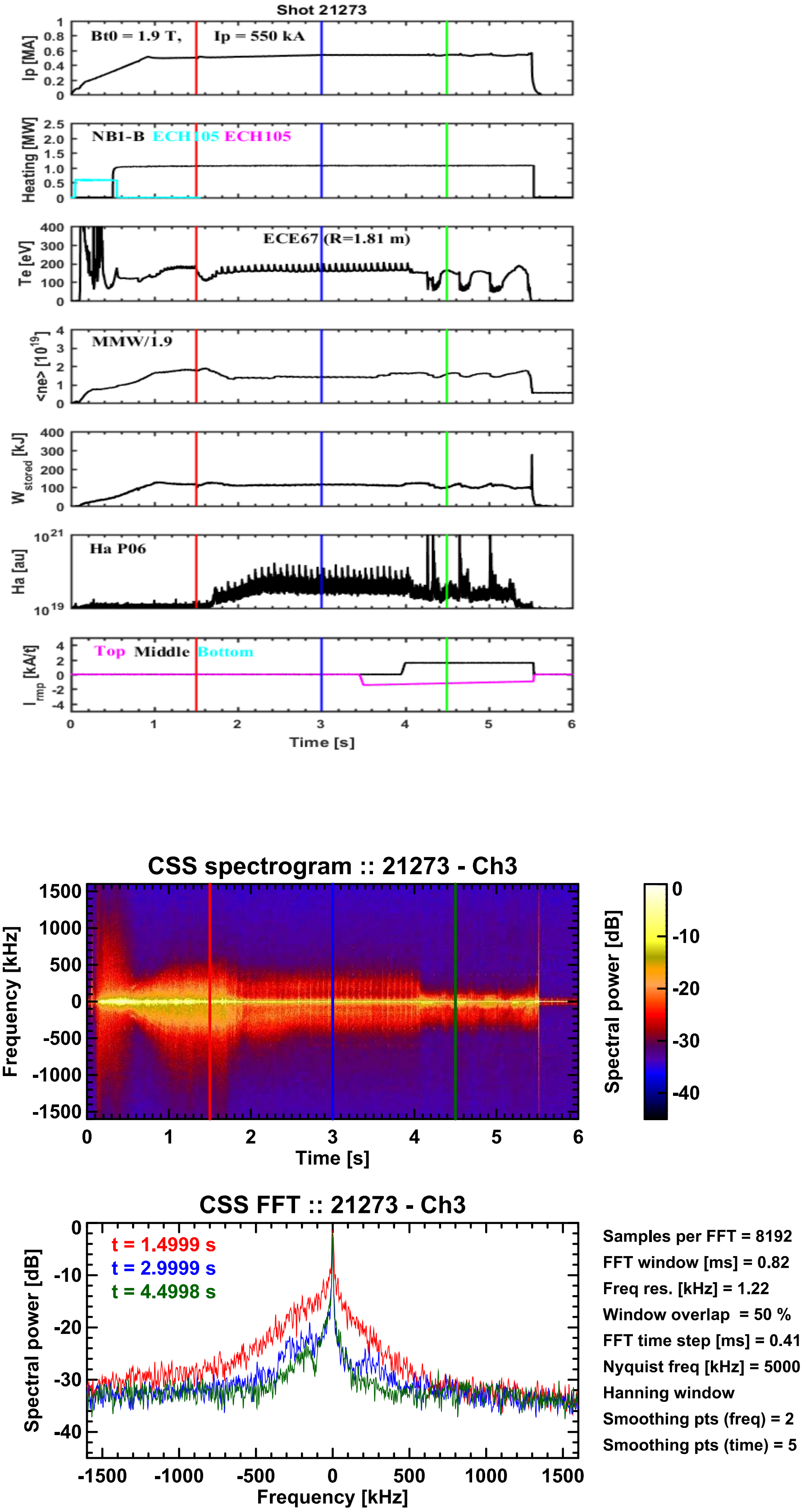

Fig. 5.3 Plasma parameter and CSS spectrogram on CH.3 of Shot 21273 in L-mode plasma.

5.2 Small-scale turbulence driven by electron temperature gradient

As mentioned in section 1.2.1, the small-scale turbulence driven by the ETG mode increases as the electron temperature gradient increases. In the previous section, we showed turbulence changes in L-mode and H-mode plasmas. In order to clearly verify whether the CSS actually measured high-k turbulence, we have compared the changes of the CSS spectrogram by increasing the electron temperature gradient near the plasma core using two ECH sources. For shot 22695 which was made at the magnetic field B_t = 1.9 T and plasma current I_p = 400 kA, the ECH2 (3-6 s, 0.8 MW, 105 GHz) and ECH3 (4-7 s, 0.7 MW, 105 GHz) were injected near the plasma core, and the CSS measurement position was ~195 cm (r/a ~0.3). The CSS spectrogram and basic plasma parameters are shown in Fig. 5.4. Although the CSS spectrogram of all channels generally showed similar results for the shot. The change in CH.2 spectrogram which is related to k_θ ~18 cm^{-1} was most clearly seen. Due to $k_\theta\rho_e$ =~0.12 and $k_\theta\rho_i$ =~2.7 in this shot, it is presumed to be an increase in the turbulence amplitude caused by the ETG mode. This is because typical ITG mode and TEM are characterized by $k_\theta\rho_i < 1$. Although there is no change in the toroidal plasma velocity in core region, the measured fluctuation becomes stronger in the electron diamagnetic direction as sotronger ECH is injected as shown in Fig 5.5. Fig. 5.5 also shows radial profiles of the electron temperature profile, ion temperature, and electron density. Looking at the ion temperature profile and electron density profile, there is no significant change compared to the electron temperature profile. Also, by calculating the normalized scale length of T_e at radius of measurement (R/L_{T_e}=R/$(d\ln T_e/dr)^{-1}$) and comparing the total spectral power of the CSS spectrogram, it seems that there is a correlation between the two parameters.

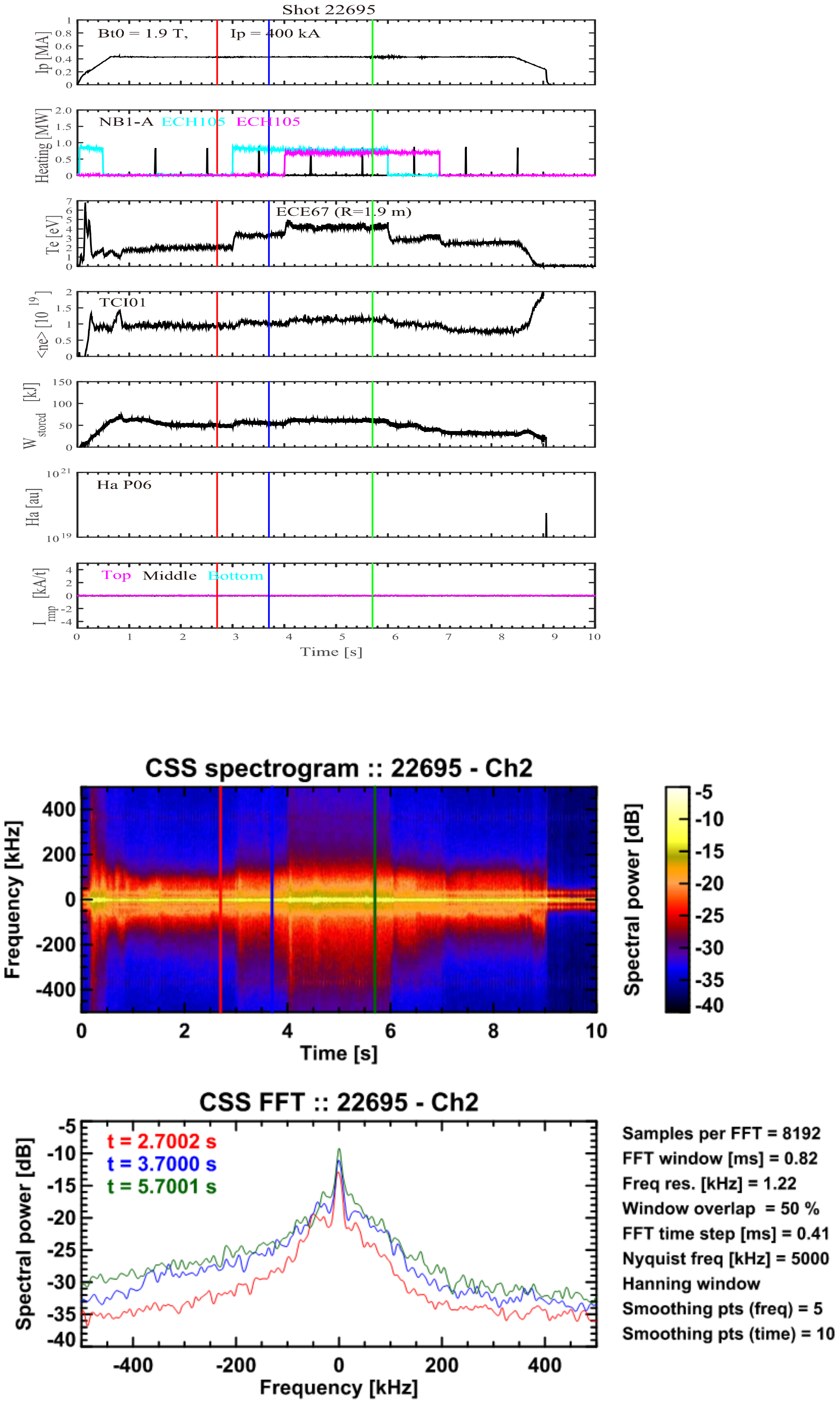

Fig. 5.4 Plasma parameters and CSS spectrogram (from CH.2) for Shot 22695 measured from the plasma core.

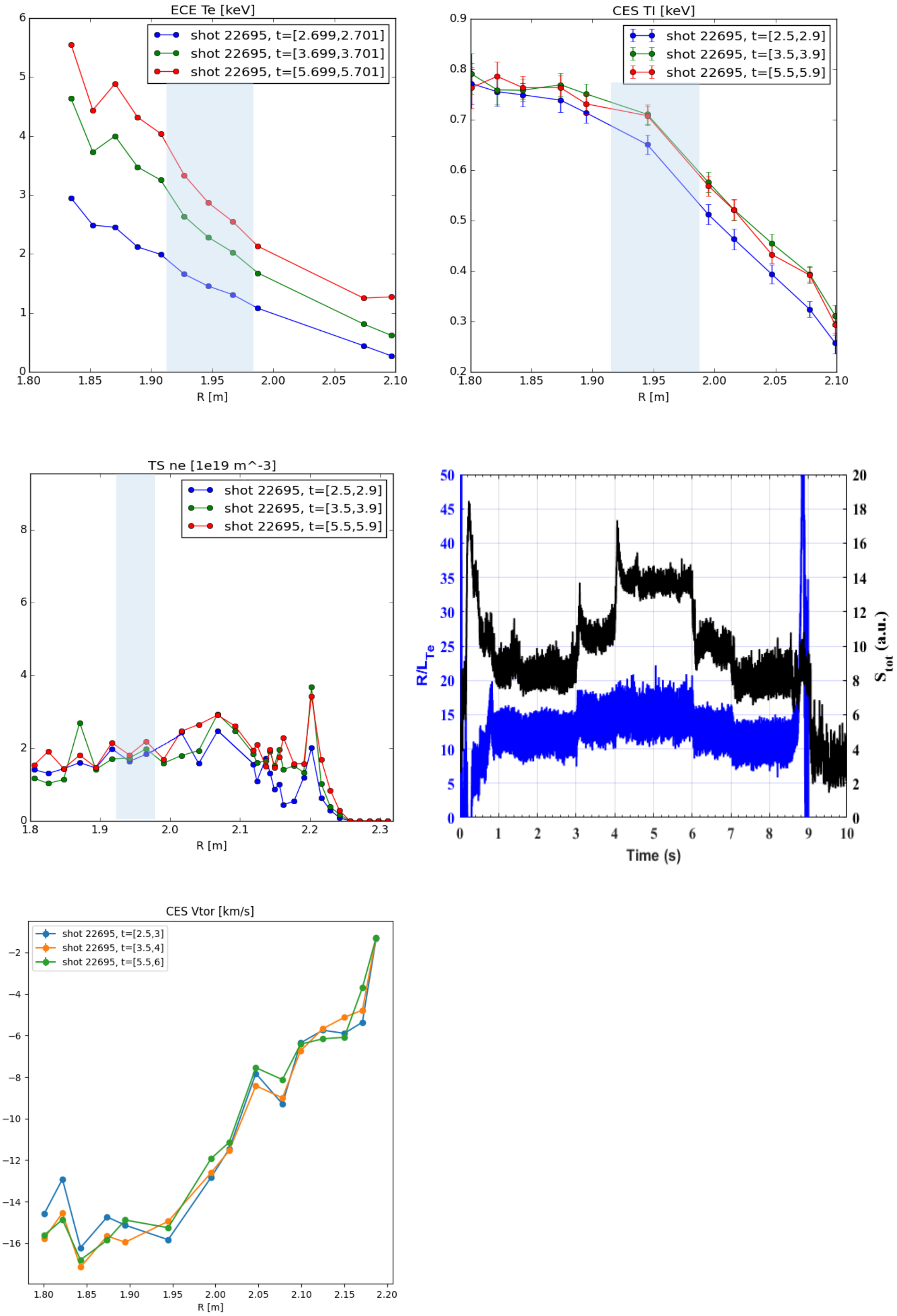

Fig 5.5 Radial profiles of electron temperature profile (ECE), ion temperature (CES), electron density (TS), and toroidal rotation velocity (CES) for shot 22695. Comparison of R/L_{T_e} and total spectral power of CSS spectrogram.

5.3 Simultaneous measurement of ITG and TEM in the H-mode plasma pedestal region

The ITG mode and TEM, known as two major micro-instabilities, can induce anomalous heat transport in the Tokamak plasmas. These modes are usually unstable in the long wavelengths limit such that $k_\theta \rho_i < 1$, where k_θ is the poloidal wave number and ρ_i is the ion Larmor radius ($\rho_i = \frac{(m_i T_i)^{\frac{1}{2}}}{eB}$ where T_i is the ion temperature and m_i is the ion mass). An important characteristic of these modes is the existence of an instability threshold. ITG mode is a drift wave rotating in the ion diamagnetic direction (the ion diamagnetic velocity is $V_{pi}^* = B \times \frac{\nabla p_i}{n_i e_i B^2}$, where n_i is the ion density, p_i is the ion pressure) and related to the normalized ion temperature gradient $\frac{\mathrm{R}}{L_{T_i}}$ where $L_{T_e} = \left(\frac{d\ln T_e}{dr}\right)^{-1}$. [21] JET experiments showed that the ion heat transports increase rapidly when $\frac{\mathrm{R}}{L_{T_i}}$ exceeds the critical ion temperature gradient. [22] The critical ion temperature gradient in the toroidal confinement plasma is given by

$$\frac{R}{L_{T_i}}\bigg|_{crit} = \left(1 + \frac{T_i}{T_e} Z_{\mathrm{eff}}\right)\left(1.33 + 1.91\frac{s}{q}\right) \tag{5.1}$$

where Z_{eff} is the ionic effective charge, q and s are the safety factor, and the magnetic shear respectively. Unlike ITG mode, TEM instabilities usually rotate in the electron diamagnetic direction and are mostly driven through a resonant interaction of the modes with trapped electrons at the precession frequency. The threshold is a critical value of $\frac{\mathrm{R}}{L_{T_e}}$ that depends on $\frac{\mathrm{R}}{L_{n_e}}$ and the fraction of trapped electrons f_t. Despite of different characteristics of these instabilities, even with similar fluctuation wavelengths, both modes can coexist in radially adjacent region in large $\frac{\mathrm{R}}{L_T}$ and $\frac{\mathrm{R}}{L_{n_e}}$. [23] Moreover, collisions can affect these modes directly or indirectly reducing the zonal flow.

These turbulence modes are interchange modes. Much higher above all thresholds, both modes combine and the growth rate is of the form (This paragraph closely follows the reference [23])

$$\gamma_0^2 = f_t \omega_{de} \omega_{pe}^* + \omega_{di} \omega_{pi}^* \tag{5.2}$$

where $\omega_{ps}^{*} = k_{\theta}V_{ps}^{*}$ and $\omega_{ds} = 2k_{\theta}\lambda_{s}V_{ds}$ (V_{ds} is the vertical drift velocity, $V_{ds} = -\frac{2T_s}{e_sBR}$, k_{θ} is a poloidal wavenumber, and $V_{ps}^{*} = B \times \frac{\nabla p_s}{n_se_sB^2}$ is the diamagnetic velocity of the species 's'). For trapped electrons, $\lambda_e = \frac{1}{4} + \frac{2s}{3}$ characterizes the dependence of the precession frequency on magnetic shear s, where $s = \frac{d\log(q)}{d\log(r)}$. For ion $\lambda_i = < \cos\theta + s\theta\sin\theta >$, where the bracket means an average over the mode poloidal structure. The particle flux of the species ('s') in a tokamak is written by

$$\Gamma_s = -D_s\nabla n_s + V_sn_s \tag{5.3}$$

where D_s is the diffusion coefficient, V_s and n_s are the pinch velocity and the density respectively. In plasmas without the neutral beam injection (NBI), the source of ionization is mainly peripheral, so that the particle flux in the core disappears. In conclusion, the ratio $\frac{V_s}{D_s}$ is a measure of particle density peaking of species ($\frac{\nabla n_s}{n_s}$). The diffusion coefficient is found to be higher than the neoclassical value for usual cases. The situation is not clear for V_s, since the neoclassical contribution driven by the inductive field, the Ware pinch [24], is rarely negligible in most Tokamak experiments. In the theoretical point of view, two additional terms contribute to the turbulent pinch. One is related with thermos diffusion [25, 26], and anticipates a pinch velocity proportional to the temperature gradient ($\frac{\nabla T_s}{T_s}$). The second contribution is proportional to the gradient and curvature of the magnetic field and is usually called the 'turbulence equi-partition' (TEP) term. [27, 28, 29] This is somewhat misleading since the magnetic curvature is not a thermo-dynamical force, but rather a geometric effect. Namely, the actual thermo-dynamical forces are the gradients of temperature and density multiplied by a geometric factor. This mechanism received some support from two-dimensional simulations of interchange turbulence [30] and TEM/ITG mode turbulence. [31] The link between particle transport and TEM was well investigated in connection with particle density transport barriers in Alcator C-Mod [32]. The physical cause of anomalous pinch comes from compressibility. In the limit of collisionless, the actual evolution equation of the density is

$$(\partial_t + v_E \cdot \nabla)n_e = V_{de} \cdot (n_e\nabla\emptyset - \nabla p_e) \tag{5.4}$$

where v_E and $\emptyset$ are the $E \times B$ drift velocity and electric potential. The compressibility terms in the right hand side of this equation lead to non-diagonal contributions in the quasi-linear flux:

$$\Gamma_s = -f_t D_{qI}\left\{\frac{\mathrm{d}n_e}{\mathrm{d}r} + C_q\frac{2}{R}n_e - C_T\frac{\mathrm{d}T_e}{T_e\mathrm{d}r}n_e\right\} \tag{5.5}$$

D_{qI} is the quasi-linear expression ($D_{qI} = \sum_{k\omega}|k_\theta \emptyset_{k\omega}/B|^2\,\tau_{c,k}$) where $\tau_{c,k}$ and $\emptyset_{k\omega}$ are a correlation time and Fourier components of perturbed electric potential. The first term is a conventional diffusion. The second term in equation 5.5 indicates to the curvature of pinch. For the case of cold electrons (vanishing term of pressure), equation 5.4 shows that the density is totally determined by the electric potential fluctuations and curvature of drift. In case of trapped electrons, the advection term on the right hand side of equation 5.4 should be replaced by the precession frequency, with $C_q = \lambda_e = \frac{1}{4} + \frac{2s}{3}$. Thus, the curvature of pinch velocity is proportional to the magnetic shear. This is consistent with the turbulence equi-partition theory. [27, 28, 29] When TEM is dominant, $C_q = \lambda_i = <\cos\theta + s\theta\sin\theta>$, i.e. is linked to the ion vertical drift velocity. The dependence on magnetic shear relys on the degree of localization of modes on the low field side. For ballooning modes that a turbulence localization close to $\theta = 0$, a dependence on magnetic shear maintains since $\lambda_i \approx\ 1 + \left(\mathrm{s} - \frac{1}{2}\right) < \theta^2 >$. The third term of equation 5.5 is the contribution of thermos-diffusion. So, the expression of C_T is quite complicated. It is positive in a region dominated by ITG mode and decreases when moving to a region dominated by TEM. Hence this transition occurs with increasing ratio of electron to ion heating power. Based on these results, turbulence simulations show that C_T changes sign when this ratio is high enough. [23] Collisional detrapping plays an important role in this problem. It was shown in that the ratio $\mathrm{V/D}$ decreases with collisionality. [33] This process is effective when the detrapping collision frequency, ν_{ei}/ε, becomes larger than $(k_\theta\rho_i)v_{Ti}/R$, which measures the electron precession frequency times a typical toroidal wavenumber. An effective value in collision frequency was defined in [33] as $\nu_{\mathrm{eff}} = (\frac{5}{2})^{1/2}\nu_{ei}\mathrm{R}/(\frac{T_e}{m_i})^{1/2}$. It is stressed here that the parameter ν_{eff} differs significantly from the conventional parameter $v^* = v_{ei}qR/\varepsilon_a^{3/2}v_{Te}$ for neoclassical transport.

With the collective scattering system, we observed density fluctuation in which each wavenumber channel rotates differently in the ion or electron diamagnetic direction in an H-mode plasma. Shot #23029 was made for an experiment for ELM control and mitigation by impurity drop (Boron Nitride) at magnetic field 1.9 T and plasma current I_p = 700 kA. The measurement position corresponds to the pedestal top region (~210 - ~220 cm) considering the scattering volume. In CH.4 (~26 cm^{-1}) and CH.3 (~20 cm^{-1}), fluctuations look to be rotating in the electron diamagnetic direction (stronger amplitude in the negative frequency), but rotating in ion diamagnetic direction (stronger amplitude in the positive frequency) in CH.2 (~18 cm^{-1}) as shown in Fig. 5.6 and 5.7. Impurity drop occurred at ~7 s, and then fluctuation corresponding to ~100 - ~300 kHz is reduced as the ELM is mitigated. In Fig. 5.8, electron density gradient decreases after the impurity drop but there is no significant change in the electron temperature. This may indicate that the fluctuation of the electron diamagnetic direction measured in CH.4 and CH.3 before the impurity is due to the TEM instabilities induced by the electron density gradient. Although the ion temperature profile near the measurement location did not change significantly, the fluctuation of the ion diamagnetic direction measured in CH.2 is presumed to be due to ITG mode by lower $\mathrm{R}/L_{T_i}\big|_{crit}$. Since the edge density and temperature higher at the transition, the coexistence of two adjacent modes are a sufficiently possible interpretation.

Another possible interpretation is that the plasma poloidal rotation velocities in the lab-frame of the TEM turbulences of different wavenumbers are not the same by the difference in the $\boldsymbol{E} \times \boldsymbol{B}$ drift velocity. The $\boldsymbol{E} \times \boldsymbol{B}$ drift wave is induced by a spatially non-uniform radial electric field and creates the sheared flows. The plasma rotation velocity of the poloidal direction in the lab-frame is composed of $\boldsymbol{E} \times \boldsymbol{B}$ drift velocity and phase velocity of micro-turbulence ($\mathbf{v}_{lab}^{pol} = \mathbf{v}_{E\times B} + \mathbf{v}_{phase}$). $\boldsymbol{v}_{E\times B}$ from the radial force balance equation is given by

$$\mathbf{v}_{E\times B} = \frac{\nabla p_i}{eZ_{\mathrm{eff}} n_i B} + V_{\emptyset i}\frac{B_\theta}{B}\hat{\emptyset} + V_{\theta i}\frac{B_\emptyset}{B}\hat{\theta} \tag{5.2}$$

Where the pressure p_i, density n_i are the parameter of the impurity or main ions with charge eZ_{eff}, toroidal velocity $V_{\emptyset i}$, poloidal velocity $V_{\theta i}$, B_θ and $B_\emptyset$ are the poloidal and toroidal magnetic field respectively. This means that if the $\boldsymbol{E} \times \boldsymbol{B}$ drift velocity is much greater than the phase velocity of micro-turbulence in electron diamagnetic direction, TEM can be observed in the ion diamagnetic direction. This $\boldsymbol{E} \times \boldsymbol{B}$ flow shear exists mainly in the H-mode pedestal region with high pressure gradient. The CH.2, which has a larger scattering volume than CH.3 and 4, is measured in a region with probably a large $\boldsymbol{E} \times \boldsymbol{B}$ velocity, and fluctuation by TEM turbulence may rotate in the ion diamagnetic direction. In the future, it will be verified which interpretation is more appropriate through simulation results.

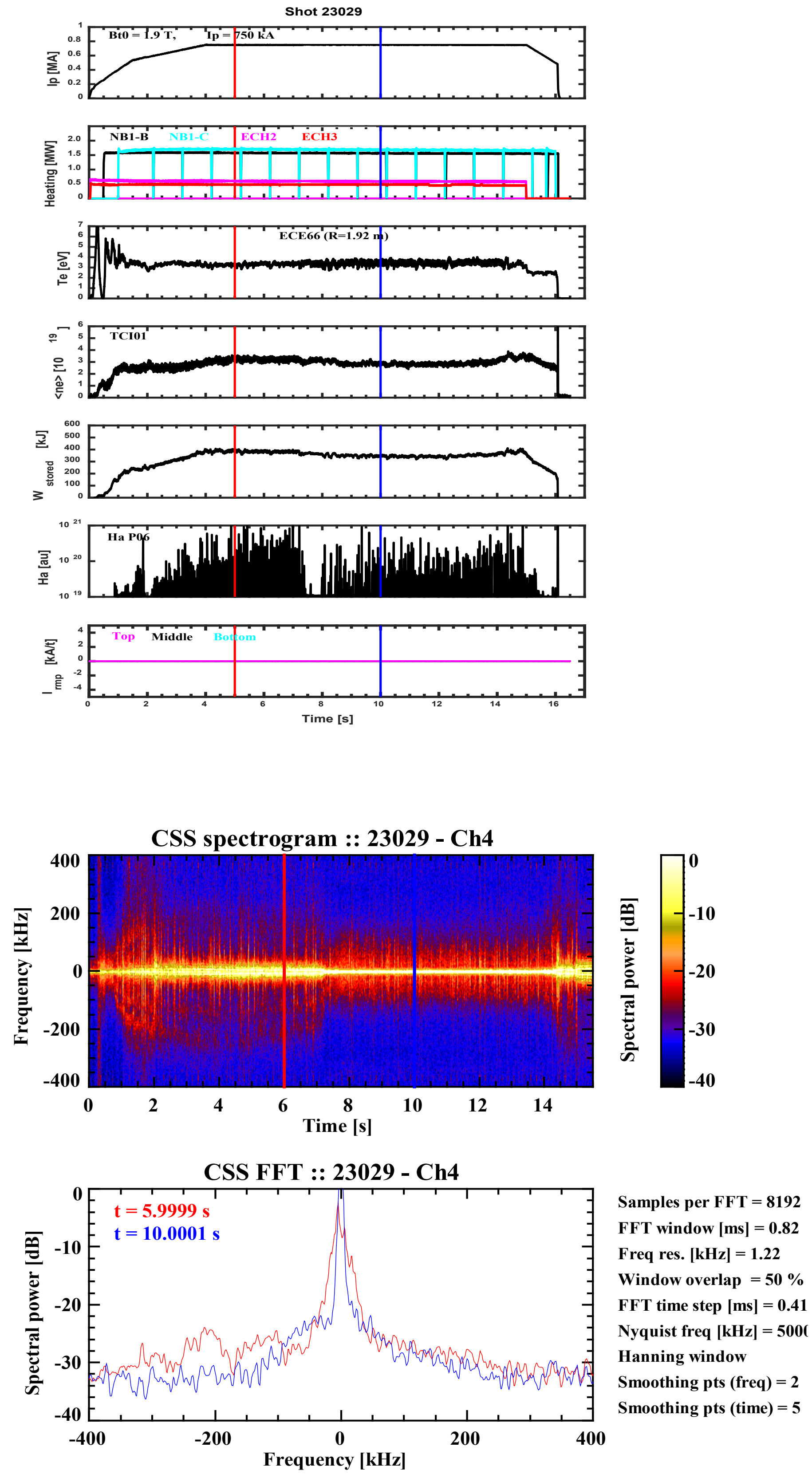

Fig. 5.6 Plasma parameter and the CSS spectrogram on CH.4 and of Shot 23029 in H-mode plasma

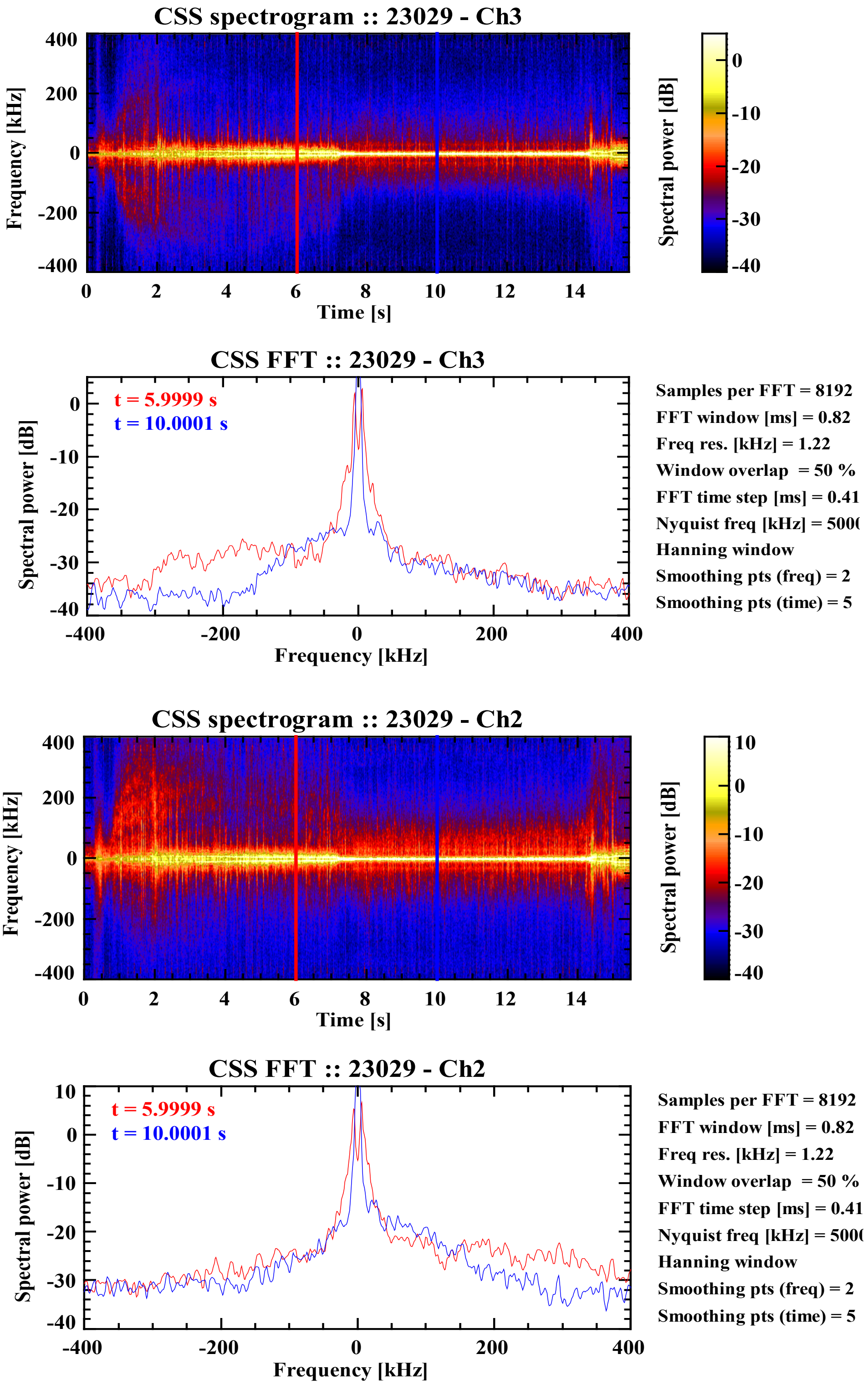

Fig. 5.7 The CSS spectrogram on CH.3 and CH.2 of Shot 23029 in H-mode plasma

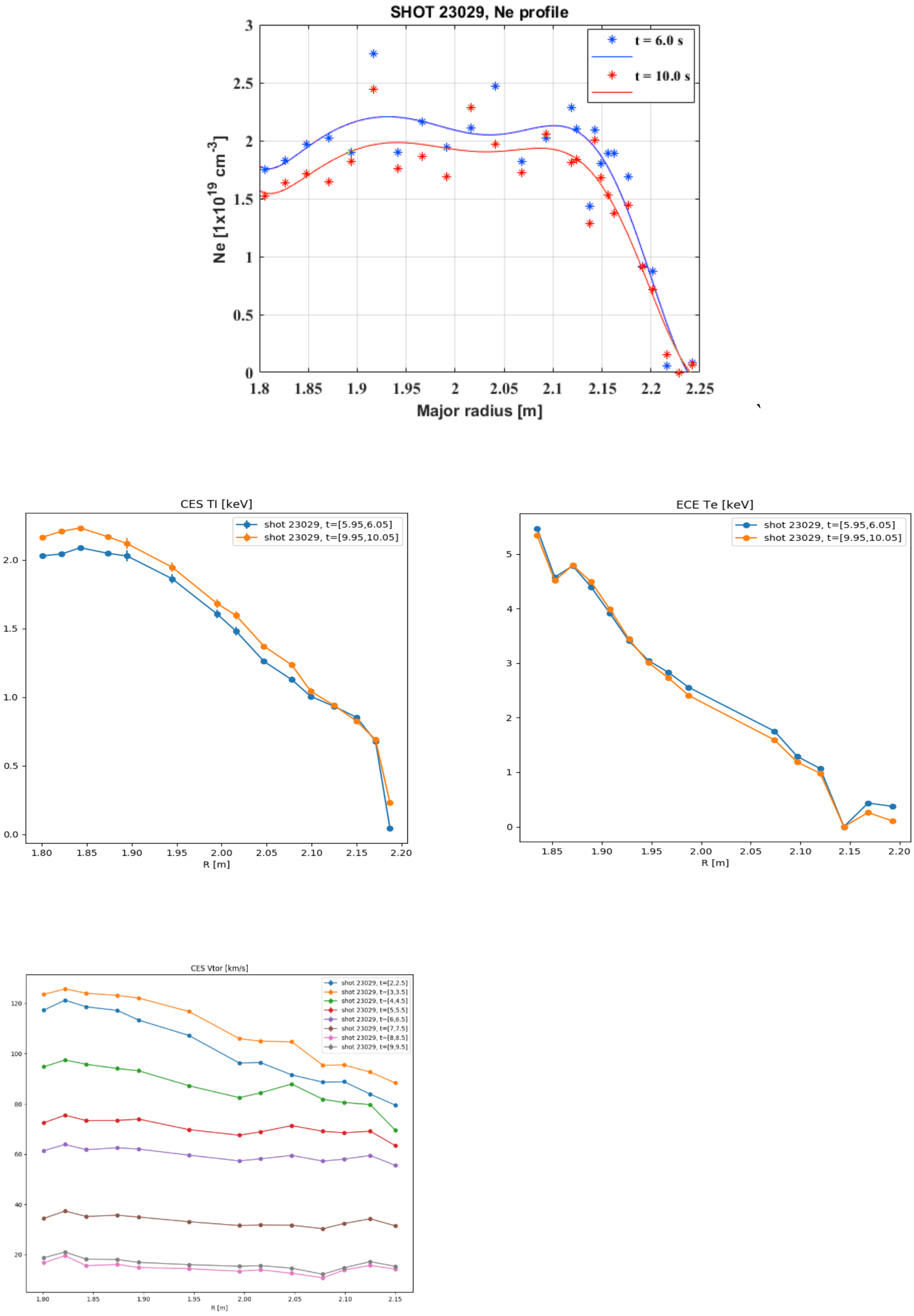

Fig. 5.8 The electron density profile, the ion temperature profile, the electron temperature profile and plasma toroidal velocity for shot 23029

Chapter 6

Summary and Conclusions

The purpose of this thesis work was to measure electron gyro-scale turbulence such as ETG mode in KSTAR plasma. To achieve this goal, the collective scattering system (CSS) was designed, and a variety of laboratory test and subsidiary studies such as strip-grid beam splitter were conducted to share optical systems with MIR system. The CSS had been developed over four years and first installed in 2018 KSTAR campaign, and then normal operation began in 2019 KSTAR campaign.

The CSS with 300 GHz O-mode probe beam can measure the electron density fluctuation at four discrete poloidal wavenumbers (~14, ~18, ~20 and ~26 cm^{-1}). The measurement position can be remotely changeable from the core to the outer edge shot-by-shot (r/a ~ 0.1-0.8). a nominal sampling rate is 10 MS/s (up to 20 MS/s) for full discharge pulse length. The spatial resolution is ~4-8 cm in the radial direction and ~1-2 cm in the poloidal direction. The wavenumber resolution is $\Delta k_{\perp}$ ~ 0.7 cm^{-1} which is based on the probe beam waist of ~ 3 cm.

In the 2019 KSTAR campaign, the data of various plasma discharges such as L-mode plasma, H-mode plasma, and ITB plasma were obtained using the CSS. After the L-H transition, a significant decrease in high-k turbulence was observed, and the RMP configuration seems to affect the high-k turbulence. In addition, the coherent turbulences that other fluctuation diagnostics have not been able to measure in the ITB plasma have been measured in the CSS, and further research is needed to determine the role of coherent turbulence in ITB plasma.

Experiments were also performed on changes in high-k turbulence due to changes in electron temperature gradient. The total spectral power of fluctuations compared with the scale of T_e at the radius of measurements. The observed fluctuations appear to be related to the electron temperature gradient. However, changes in average density and stored energy are also similar to those. It needs to be verified by comparison with a critical temperature gradient through simulation code.

The MHD instabilities such as ELM burst, Alfven eigenmode and ion gyro-scale fluctuation can be measured in the CSS spectrogram, because the fluctuations in the vicinity of the measurement position are carried in the scattered beam like the interferometry. This interferometric signals are characterized by being symmetric on the CSS spectrogram. Therefore, when analyzing CSS data, it is necessary to perform comparative analysis with data from other diagnostics to prevent misinterpretation.

In conclusion, the CSS will make a great contribution to small scale turbulence studies such as its physical properties and suppression mechanism. Furthermore, we expect to make the contribution to the field of turbulence simulation of trapped electron mode (TEM) and ETG mode, which was difficult to prove experimentally. In the future, more intensive analyses of CSS data will be carried out for studies of physics associated with small scale turbulence such as characteristics of ETG or trapped electron mode (TEM) in KSTAR H-mode or hybrid mode edge and their contribution to the plasma performance *This work was supported by the Ministry of Science and ICT of Korea under the KSTAR project and the NRF of Korea under contract Nos. NRF-2014M1A7A1A03029865 and NRF-2015M1A7A02002627.

Appendix

A.

1. Fourier transform and inverse Fourier transform:

$$f(\vec{k},\omega) = \int_{-\infty}^{+\infty} dt \int_{-\infty}^{+\infty} d^3r \;\; f(\vec{r},t)e^{-i(\vec{k}\cdot\vec{r}-\omega t)} \tag{A.1}$$

$$f(\vec{r},t) = \int_{-\infty}^{+\infty} \frac{d\omega}{2\pi} \int_{-\infty}^{+\infty} \frac{d^3k}{(2\pi)^3} \;\; f(\vec{k},\omega)e^{i(\vec{k}\cdot\vec{r}-\omega t)} \tag{A.2}$$

2. Parseval's Theorem:

$$\int_{-\infty}^{+\infty} dt \, |f(t)|^2 = \int_{-\infty}^{+\infty} \frac{d\omega}{2\pi} \;\; |f(\omega)|^2 \tag{A.3}$$

3. Delta function:

$$\int_{-\infty}^{+\infty} dt \;\; e^{i\omega t} = 2\pi\delta(\omega) \tag{A.4}$$

$$\int_{-\infty}^{+\infty} d^3r \;\; e^{i\vec{k}\cdot\vec{r}} = (2\pi)^3\delta(\vec{k}) \tag{A.5}$$

4. Integral formula I:

$$\int_{-\infty}^{+\infty} dx \;\; e^{-\frac{x^2}{a^2}} = a\sqrt{\pi} \tag{A.6}$$

5. Integral formula II:

$$\begin{aligned} \int_{-\infty}^{+\infty} dx \, e^{-\frac{x^2}{a^2}-ibx} &= \int_{-\infty}^{+\infty} dx \;\; e^{-\frac{1}{a^2}(x^2+ia^2x-\frac{a^4b^2}{4}+\frac{a^4b^2}{4})} \\ &= \int_{-\infty}^{+\infty} dx \;\; e^{-\frac{1}{a^2}(x+i\frac{a^2b}{2})^2} e^{-\frac{a^2b^2}{4}} \\ &= a\pi e^{-\frac{a^2b^2}{4}} \end{aligned} \tag{A.7}$$

6. Integral formula III:

$$\int_{-\frac{L_z}{2}}^{+\frac{L_z}{2}} dx \;\; e^{iax} = \left[\frac{e^{iax}}{ia}\right]_{-L_z/2}^{+L_z/2} = \frac{e^{\frac{iaL_z}{2}} - e^{\frac{-iaL_z}{2}}}{ia}$$

$$= \frac{2i\sin(\frac{aL_z}{2})}{ia} = \ L_z\frac{\sin(\frac{aL_z}{2})}{\frac{aL_z}{2}}$$

$$= L_z\ \operatorname{sinc}\left(\frac{aL_z}{2}\right) \tag{A.8}$$

B.

1. Product rule with del operator:

$$\nabla\big(\vec{A}\cdot\vec{B}\big) = \big(\vec{A}\cdot\nabla\big)\vec{B} + \big(\vec{B}\cdot\nabla\big)\vec{A} + \vec{A}\times\big(\nabla\times\vec{B}\big) + \vec{B}\times\big(\nabla\times\vec{A}\big) \tag{B.1.1}$$

$$\vec{A}\times(\vec{B}\times\vec{C})\ \ =\ \ \vec{B}(\vec{A}\cdot\overrightarrow{C}) - \vec{C}(\vec{A}\cdot\overrightarrow{B}) \tag{B.1.2}$$

2. First term of Eq. (2.23 (a)):

$$\big(\vec{R}\cdot\nabla\big)\vec{v} = \ \left(R_x\frac{\partial}{\partial x} + R_y\frac{\partial}{\partial y} + R_z\frac{\partial}{\partial z}\right)\vec{v}(t')$$

$$= \ R_x\frac{d\vec{v}}{dt}\frac{\partial t'}{\partial x} + R_y\frac{d\vec{v}}{dt}\frac{\partial t'}{\partial y} + R_z\frac{d\vec{v}}{dt}\frac{\partial t'}{\partial z}$$

$$= \dot{\vec{v}}\big(\vec{R}\cdot\nabla t'\big) \tag{B.2}$$

3. Second term of Eq. (2.23 (a)):

$$(\vec{v}\cdot\nabla)\vec{R} = (\vec{v}\cdot\nabla)\vec{r} - (\vec{v}\cdot\nabla)\overrightarrow{r'} \tag{B.3.1}$$

$$= \vec{v} - \vec{v}(\vec{v}\cdot\nabla t') \tag{B.3.2}$$

4. Similar to Eq. (B.2), Eq. (B.3.1) becomes:

$$(\vec{v}\cdot\nabla)\vec{r} = \left(v_x\frac{\partial}{\partial x} + v_y\frac{\partial}{\partial y} + v_z\frac{\partial}{\partial z}\right)(x\hat{x} + y\hat{y} + z\hat{z}) = \vec{v} \tag{B.4}$$

$$(\vec{v}\cdot\nabla)\overrightarrow{r'} = \vec{v}(\vec{v}\cdot\nabla t') \tag{B.5}$$

5. Third term of Eq. (2.23 (a)):

$$\nabla\times\vec{v} = \ \left(\frac{\partial v_z}{\partial y} - \frac{\partial v_y}{\partial z}\right)\hat{x} + \left(\frac{\partial v_x}{\partial z} - \frac{\partial v_z}{\partial x}\right)\hat{y} + \left(\frac{\partial v_y}{\partial x} - \frac{\partial v_x}{\partial y}\right)\hat{z}$$

$$= \ \left(\frac{dv_z}{dt'}\frac{\partial t'}{\partial y} - \frac{dv_y}{dt'}\frac{\partial t'}{\partial z}\right)\hat{x} + \left(\frac{dv_x}{dt'}\frac{\partial t'}{\partial z} - \frac{dv_z}{dt'}\frac{\partial t'}{\partial x}\right)\hat{y} + \left(\frac{dv_y}{dt'}\frac{\partial t'}{\partial x} - \frac{dv_x}{dt'}\frac{\partial t'}{\partial y}\right)\hat{z}$$

$$= -\vec{a}\times\nabla t' \tag{B.6}$$

6. In the same way as Eq. (B.6), Fourth term of Eq. (2.23 (a)) becomes:

$$\begin{aligned}\nabla\times\vec{R} &= \nabla\times\vec{r}-\nabla\times\overrightarrow{r'}\\ &= -\vec{v}\times\nabla t' \end{aligned} \tag{B.7}$$

where $\nabla\times\vec{r}=0$

7. Calculation required for Eq. (2.30):

From Fig. 2.3,

$$c(t-t')=R \quad => \quad c^2(t-t')^2=R=\vec{R}\cdot\vec{R} \tag{B.8}$$

Differentiate with respect to t:

$$2c^2(t-t')\left(1-\frac{\partial t'}{\partial t}\right)=2\vec{R}\cdot\frac{\partial\vec{R}}{\partial t} \quad => \quad cR\left(1-\frac{\partial t'}{\partial t}\right)=\vec{R}\cdot\frac{\partial\vec{R}}{\partial t} \tag{B.9}$$

$$\frac{\partial\vec{R}}{\partial t}=-\frac{\partial\overrightarrow{r'}}{\partial t}=-\frac{\partial\overrightarrow{r'}}{\partial t'}\frac{\partial t'}{\partial t}=-\vec{v}\frac{\partial t'}{\partial t} \quad => \quad cR\left(1-\frac{\partial t'}{\partial t}\right)=-\vec{R}\cdot\vec{v}\frac{\partial t'}{\partial t}$$

$$=> \quad cR=\frac{\partial t'}{\partial t}\left(\vec{R}\cdot\left(c\hat{R}-\vec{v}\right)\right) \tag{B.10}$$

$$\frac{\partial t'}{\partial t}=\frac{cR}{\left(cR-\vec{R}\cdot\vec{v}\right)} \tag{B.11}$$

References

[1] M. Greenwald *et al*, “A new look at density limits in tokamaks”. *Nuclear fusion*, **28**, 2199, 1988.

[2] Martin Greenwald *et al*, “Density limits in toroidal plasmas”, *Plasma Physics and Controlled Fusion*, **44**, R27, 2002.

[3] G.S. Lee *et al*, “Design and construction of the kstar tokamak”, *Nuclear Fusion*, **41**(10):1515-1523, 2001.

[4] M. Shimadae, “Chapter 1: Overview and summary”, *Nuclear Fusion*, **47**(6):S1-S17, 2007.

[5] W. Dorland, F.Jenko *et al*, “Electron Temperature Gradient Turbulence”, *Physical Review Letters*, **85**, 2000.

[6] W. Lee *et al*, “Design of a collective scattering system for small scale turbulence study in Korea Superconducting Tokamak Advanced Research”, *Review of Scientific Instruments*, **87**, 043501, 2016.

[7] D.R. Smith *et al*, “A collective scattering system for measuring electron gyroscale fluctuations on the National Spherical Torus Experiment”, *Review of Scientific Instruments*, **79**, 123501, 2008.

[8] E. Mazzucato *et al*, “Short-Scale Turbulent Fluctuations Driven by the electron-Temperature Gradient in the National Spherical Torus Experiment”, *Physical Review Letters*, **101**, 075001, 2008.

[9] H. Park, “Tokamak Plasma Wave Studies via Multi-Channel Far Infrared Laser Scattering”, *PhD Thesis*, UCLA, Los Angeles, CA, 1984.

[10] W. Lee, “Collective Thomson Scattering System for Transport Study on NSTX”, *PhD Thesis*, POSTECH, Pohang, 2008.

[11] J.D. Jackson, “Classical Electrodynamics Third Edition”, *John Wiley & Sons*, 1999.

[12] W. Lee *et al*, “Poloidal rotation velocity measurement with an MIR system on KSTAR”, *Journal of Instrumentation*, **8**, C10018, 2013.

[13] W. Lee et al, “Microwave imaging reflectometry for density fluctuation measurement on KSTAR”, *Nuclear Fusion*, **54**, 023012, 2014.

[14] Y.U. Nam *et al*, “Analysis of edge density fluctuation measured by trial KSTAR beam emission spectroscopy system”, *Review of Scientific Instruments*, **83**, 10D530, 2012.

[15] D.H. Chang *et al*, “Design of neutral beam injection system for KSTAR tokamak”, *Fusion Engineering and Design*, **86**, 2-3, 2011.

[16] G.S. Yun *et al*, “Development of KSTAR ECE imaging system for measurement of temperature fluctuations and edge density fluctuations”, *Review of Scientific Instruments*, **81**, 10D930, 2010.

[17] G.S. Yun *et al*, “Quasi 3D ECE imaging system for study of MHD instabilities in KSTAR”, *Review of Scientific Instruments*, **85**, 11D820, 2014.

[18] D.J. Lee *et al*, “A large-aperture strip-grid beam splitter for partially combined two millimeter-wave diagnostics on Korea Superconducting Tokamak Advanced Research”, *Review of Scientific Instruments*, **90**, 014703, 2019.

[19] P.F. Goldsmith, “Quasioptical System: Gaussian Beam Quasioptical Propagation and applications”, *Wiley-IEEE Press*, p.235, 1998.

[20] W.J. Smith, “Modern Optical engineering: The Design of Optical System”, *McGraw-Hill*, p.187, 1990.

[21] B. Coppi *et al*, “Instabilities due to temperature gradients in complex magnetic field configurations”, *Physics of Fluids*, **10**, 1966.

[22] P. Mantica *et al*, “Experimental study of the ion critical-gradient length and stiffness level and the impact of rotation in the jet tokamak”, *Physical Review Letters*, **102**, 2009.

[23] X. Garbet *et al*, “Physics of transport in tokamaks”, *Plasma Physics and Controlled Fusion*, **46**, 2004.

[24] A.A. Ware , “Pinch-Effect Oscillations in an Unstable Tokamak Plasma”, *Physical Review Letters*, **25**, 916, 1970.

[25] B. Coppi et al, “Ion-Mixing Mode and Model for Density Rise in Confined Plasmas”, *Physical Review Letters*, **41**, 551, 1978.

[26] W.M. Tang *et al*, “Microinstabilities in weak density gradient tokamak systems”, *Physics of Fluids*, **29**, 3715, 1986.

[27] V.V. Yankov, *JETP Lett*, **60**, 171, 1994

[28] M.B. Isichenko *et al*, “Anomalous pinch effect and energy exchange in tokamaks”, *Physics of Plasmas*, **3**, 1916, 1996.

[29] D.R. Baker *et al*, “Density profile consistency and its relation to the transport of trapped versus passing electrons in tokamaks” *Physics of Plasmas*, **5**, 2936, 1998.

[30] V. Naulin *et al*, “Equipartition and Transport in Two-Dimensional Electrostatic Turbulence”,

Physical Review Letters, **81**, 4148, 1998.

[31] H. Norman et al, “Simulation of toroidal drift mode turbulence driven by temperature gradients and electron trapping”, *Nuclear Fusion*, **30**, 983, 1990.

[32] D.R. Ernst *et al*, “Role of trapped electron mode turbulence in internal transport barrier control in the Alcator C-Mod Tokamak”, *Physics of Plasmas*, **11**, 2637, 2004.

[33] C. Angioni et al, “Theory-based modeling of particle transport in ASDEX Upgrade H-mode plasmas, density peaking, anomalous pinch and collisionality”, *Physics of Plasmas*, **10**, 3225, 2003.

Acknowledgement

다사다난했던 2020년이 지나고, 2021년 새해가 되었습니다. 늦게나마 감사의 글을 쓰고 있는 지금, 지난 시간 동안 있었던 많은 일들이 생각이 납니다. 박사학위라는 새로운 도전을 시작하기 위해 울산으로 간지가 엊그제 같은데 벌써 7년이라는 시간이 흘러 졸업을 하게 된다니 꿈을 꾸는 것 같은 느낌입니다. 짧다면 짧지만 저에게는 무척이나 긴 시간이었고, 그 동안 울산, 포항, 대전에서 만나 인연을 맺고 저를 도와주셨던 많은 분들께 감사의 말씀을 드립니다. 특히 학위 과정 막바지에 많이 힘들어 하던 저를 응원 해주시던 많은 분들께도 감사의 말씀을 드립니다.

먼저 디펜스 심사와 이 논문을 완성 할 수 있도록 도와주신 박현거 교수님, 인용균 교수님, 최은미 교수님, 남용운 박사님, 이우창 박사님께 진심으로 감사드립니다. 7년동안 저를 지도해주시고, 제가 하는 일이 많은 지원을 아끼지 않으셨던 박현거 교수님께 다시 한번 감사드립니다. 핵융합 학계에서 대가의 제자가 된다는 것이 쉽지가 않은 일인데, 그런 기회를 주시고 마지막까지 챙겨주셔서 많은 은혜를 입은 것 같습니다. 그리고, 제2의 지도 교수님이라고 해도 부족하지 않으신 이우창 박사님께도 감사의 말씀을 드립니다. 제가 성장 할 수 있도록 많은 가르침을 주셨고, 연구자의 참된 모습이 무엇인지 보고 배울 수 있었던 것 같습니다. 국가핵융합연구소에서 참여연구자로서 연구를 할 수 있도록 기회와 많은 지원을 해주셨던 남용운 박사님께도 감사의 말씀을 드립니다.

학위 과정 막바지에 방황하던 저를 잡아주시고, 좋은 말씀해주셨던 이규동 박사님, 고원하 박사님께도 감사의 말씀을 드립니다. 그리고 이재현 박사님, 최민준 박사님, 김민우 박사님, 남윤범 박사님께도 감사의 말씀을 드립니다. 비록 학교는 다르지만, 저에겐 선배와 같았고, CSS 장치 개발 및 운영할 수 있게 많은 도움을 받았습니다. 편한 친구 같았던 그리고 사수였던 임준억 박사님, 김민호 박사님께도 감사의 말씀을 드립니다. 대전에서 적응할 수 있도록 저를 많이 챙겨주신 김성국 박사님, 한종원 기술원님께도 감사의 말씀을 드립니다. 울산에서 잘 챙겨 주시던 이인근 박사님, 류민우 박사님께도 감사의 말씀을 드립니다. 그리고 Lab은 다르지만 동기인 규빈이, 후배와 같았던 진영, 인한이도 남은 학업 잘 마무리하여 좋은 결과가 있기를 바랍니다. 같은 분야에 계신 모든 분들과 즐겁게 연구하면서 소중한 인연 계속해서 이어가기를

바랍니다.

힘들 때 위로해주고, 응원해주던 상인동 친구들인 천국, 경재, 동한, 승환이 에게도 감사의 말을 전합니다. 박사학위 마무리 중인 기범이도 좋은 결과가 있기를 바라고, 함께해서 좋았다라는 말을 전하고 싶습니다. 원상이, 주형이 에게도 감사의 말을 전합니다. 대학 시절 같이 도서관에 모여 공부하고, 함께 놀았던 습관으로 인해 제가 여기까지 올 수 있었다고 생각합니다. 그리고 인생의 멘토이자, 베프인 남이 에게도 감사의 말을 전하고, 힘든 순간마다 항상 나의 버팀목이 되어줘서 고맙게 생각합니다.

마지막으로 저를 아낌없이 지원해주시고 키워주신 어머니와 하늘에 계신 아버지께 감사의 말과 사랑한다는 말을 드리고 싶습니다. 특히 학위과정중에 가까이 계셨지만 자주 못 찾아 뵈었던 것이 가장 후회가 됩니다. 더 후회하지 않게 효도 하면서 살도록 하겠습니다. 그리고 오랫동안 인연을 맺었던 장경자님, 김미혜씨께도 감사의 말씀을 드립니다. 계속해서 이 소중한 인연들 오래가기를 간절히 바랍니다.

이동재 올림

Curriculum Vitae

Name : Dong Jae Lee

Date of Birth : January 24, 1986

E-mail : djlee0913@gmail.com

Education

2014. 3. - 2020. 8. Ph.D. in Department of Physics, UNIST

2005. 3. - 2014. 2. B.S in Department of Physics, Kyungbuk National University

2002. 3. - 2005. 2. Daegu High School

Experience

2018. 9. 1. - 2019. 6. 31. Student Researcher : Development, Installation and operation of the Microwave Imaging Reflectometry, Collective Scattering system, Nuclear Fusion Research Institute

2016. 9. 1. - 2018. 9. 01. Participating Researcher : Development of scattering system for turbulence study on KSTAR, Nuclear Fusion Research Institute

2013. 7. - 2013. 8. Intern : Density measurements in KSTAR from emission spectroscopy , Nuclear Fusion Research Institute

Research Interests

1. Development and installation of advanced microwave diagnostics in KSTAR (Electron Cyclotron Emission Imaging, Microwave Imaging Reflectometry, Collective Scattering System)
2. Maintenance and operation of Microwave Imaging Reflectometry, Collective Scattering system in KSTAR
3. Optics design of millimeter wave and sub THz system
4. Laboratory experiments with W-band millimeter wave, sub THz wave and RF components

Publication

1. W. Lee, D.J. Lee, H.K. Park, Y.U. Nam, T.G. Lee, M.J. Choi, H.J Ahn, H.K. Park, Y.S. Na, M.S. Park, “Development of a collective scattering system and its application to the measurement of multiscale fluctuations in KSTAR plasmas”, Plasma Phys. Control. Fusion **63,** 035003 (2021)

2. W. Lee, J. Lee, D.J. Lee, H.K. Park, "Study of the origin of quasi-coherent modes in low-density KSTAR ECH plasmas" Nuclear Fusion, **61**, 016008 (2020)
3. M. Joung, M. Woo, J.W. Han, S.J. Wang, S.G. Kim, S.H, Hahn, D.J. Lee, J.G. Kwak, R. Ellis, "Design of ECH launcher for KSTAR advanced Tokamak operation", Fusion Engineering and Design, **151**, 111395 (2020)
4. D.J. Lee, W. Lee, H.K. Park and T.G. Kim, "A large-aperture strip-grid beam splitter for partially combined two millimeter-wave diagnostics on Korea Superconducting Tokamak Advanced Research", Rev. Sci. Instrum. **90**, 014703 (2019)
5. W. Lee, J. Leem, D.J. Lee, M.J. Choi, H.K. Park, J.A. Lee, G.S. Yun, T.G. Kim, H. Park, K.W. Kim, "Quasi-coherent fluctuation measurement with the upgraded microwave imaging reflectometer in KSTAR, Plasma Phys. Control. Fusion **60** (2018)
6. Y.B. Nam, D.J. Lee, J. Lee, C. Kim, G.S. Yun, W. Lee and H.K. Park, "New compact and efficient local oscillator optics system for the KSTAR electron cyclotron emission imaging system", Rev. Sci. Instrum. **87** (2016)
7. W. Lee, H.K. Park, D.J. Lee, Y.U. Nam, J. Leem and T.K. Kim, "Design of a collective scattering system for small scale turbulence study in Korea Superconducting Tokamak Advanced Research", Rev. Sci. Instrum. **87** (2016)

Academic Activities

1. D.J. Lee, W. Lee, T.G. Lee, M.J. Choi, Y.U. Nam and H.K. Park, "Collective scattering system developed for high-k turbulence study in KSTAR", 14th International Reflectometry Workshop,

Lausanne, Swiss, May 22 – 24, 2019

2. D.J. Lee, W. Lee, T.G. Lee, M.J. Choi, Y.U. Nam and H.K. Park, "Commissioning of the collective scattering system developed for high-k turbulence study", 5th UNIST-kyoto Univ. Workshop, Pusan, Korea, April. 22 – 23, 2019
3. D.J. Lee, W. Lee, T.G. Lee, M.J. Choi, Y.U. Nam and H.K. Park, "Commissioning of the collective scattering system developed for electron gyroscale turbulence study", 2019 KSTAR conference, Seoul, Korea, Feb. 20 – 22, 2019
4. D.J. Lee, W. Lee, H.K. Park, J. Leem and Y.U. Nam, "Collective scattering system for high-k turbulence measurement and the modified MIR in KSTAR", 9th Japan-Korea Seminar on Advanced Diagnostics for Steady-state Fusion Plasmas, Toki-Nagoya, Japan, Aug. 7 – 10, 2018
5. D.J. Lee, W. Lee, H.K. Park, J. Leem and Y.U. Nam, "Collective Thomson scattering System and the modified MIR system in KSTAR", 2018 KSTAR conference, Muju, Korea, Feb. 21 – 23, 2018
6. D.J. Lee, W. Lee, H.K. Park, J. Leem and Y.U. Nam, "Collective Thomson Scattering System combined with the MIR system in KSTAR", 2017 KPS Fall Meeting, Kyungju, Korea, Oct. 25 – 27, 2017
7. D.J. Lee, W. Lee, H.K. Park, J. Leem, Y.U. Nam, T.K. Kim and H. Park, "Design characteristics of a microwave collective scattering system for KSTAR", 8th Korea-Japan Workshop on Advanced Diagnostics for Steady-State Fusion Plasmas, Pusan, Korea, Aug. 24 – 27, 2016
8. D.J. Lee, W. Lee, H.K. Park, J. Leem, Y.U. Nam, T.K. Kim and H. Park, "Design characteristics of a microwave collective scattering system for KSTAR", High-Temperature Plasma Diagnostics, Wisconsin-Madison, US, June 5 – 9, 2016
9. D.J. Lee, W. Lee, H.K. Park, J. Leem, Y.U. Nam, T.K. Kim and H. Park, "Design of a collective scattering system for small scale turbulence study on KSTAR", KPS 2016 spring meeting, Dageon, Korea, April 20 – 22, 2016

10. D.J. Lee, W. Lee, H.K. Park, J. Leem, Y.U. Nam, T.K. Kim and H. Park, “Design characteristics of the KSTAR collective scattering system for small scale turbulence study”, 2016 KSTAR conference, Dageon, Korea, Jan. 24- 26, 2016